

Semiconducting nanowire-based Josephson junctions for qubits

Inauguraldissertation

zur
Erlangung der Würde eines Doktors der Philosophie
vorgelegt der
Philosophisch-Naturwissenschaftlichen Fakultät
der Universität Basel

von

Luk Yi Cheung

2024

Genehmigt von der Philosophisch-Naturwissenschaftlichen Fakultät
auf Antrag von

Erstbetreuer: Prof. Dr. Christian Schönenberger

Zweitbetreuer: Prof. Dr. Dominik Zumbühl

Externer Experte: Prof. Dr. Attila Geresdi

Externer Experte: Dr. Marcelo Goffman

Basel, den 28.03.2023

Prof. Dr. Marcel Mayor
Dekan

Contents

1. Introduction	1
2. Andreev bound states in SNS Josephson junctions	5
2.1. Andreev reflection	5
2.2. Andreev bound states	7
2.3. Effects of back-scattering and finite length	7
2.4. Spin-orbit coupling	10
2.5. Andreev level and Andreev spin qubits	13
2.6. Full-shell epitaxial InAs/Al nanowires	14
3. Integration of superconducting resonators with Andreev qubits	17
3.1. Hamiltonian description of superconducting resonators	17
3.2. Quarter-wavelength transmission line resonator	19
3.3. RF SQUID	20
3.4. Inductive coupling	21
3.5. Dispersive limit	24
4. DC transport measurement of full-shell epitaxial InAs/Al nanowire Josephson junctions	27
4.1. Device	27
4.2. Measurement techniques	28
4.3. Josephson current	28
4.4. Multiple Andreev reflections	31
4.5. Transparency estimation	34
4.6. Conclusion	34
5. Designing a superconducting cavity coupler for Andreev qubits	37
5.1. Half-wavelength transmission line resonator	37
5.2. Capacitively coupled quarter-wavelength transmission line resonator pair	39
5.2.1. Resonator excitation	41
5.2.2. Inter-resonator coupling capacitance	42
5.2.3. Shared inductance	43
5.3. Final design	44
5.4. Conclusion	46

6. Microwave spectroscopy of Andreev bound states in epitaxial InAs/Al nanowire Josephson junctions	49
6.1. Device	49
6.2. Qubit-resonator interaction	52
6.3. Qubit linewidth	54
6.4. Coherent manipulation of pair transitions	56
6.5. Spin-orbit splitting of ABSs	57
6.6. Conclusion	59
7. Photon-mediated long-range coupling of two Andreev pair qubits	61
7.1. Abstract	62
7.2. Main	62
7.3. Dual-mode superconducting cavity coupler	67
7.4. Conclusion	68
7.5. Extended data	69
8. Gatemon qubit using Ge/Si core/shell nanowire Josephson junctions	77
8.1. Device	80
8.2. Gatemon spectroscopy	83
8.3. Quantum coherence	84
8.4. Conclusion	87
9. Experimental techniques	91
9.1. Device fabrication	91
9.2. Sample holder	93
9.3. Cryostat wiring	94
9.4. Room temperature microwave setup	97
9.5. Qubit measurement protocol	100
10. Conclusion and outlook	107
Bibliography	111
A. Cavity readout	121
B. Derivation of the capacitively coupled quarter-wavelength transmission line resonator	123
C. Additional DC transport measurement of full-shell epitaxial InAs/Al nanowire Josephson junctions	125
D. Additional microwave spectroscopy measurement of full-shell epitaxial InAs/Al nanowire Josephson junctions	129

Publications	131
Acknowledgements	133

1 Introduction

The basic building block of a quantum computer is a quantum bit (qubit), a quantum two level system, that stores information in the superposition of the two quantum states [1]. Ideally, a qubit should have a long coherence time, fast manipulation, and a small footprint [2]. For over two decades, the quest for stable large-scale qubit systems that can execute useful computational tasks has fueled intense research in condensed matter physics. As a result of a journey of proof-of-principle experiments, demonstrating single-qubit operations [3, 4], long range qubit-qubit interactions [5, 6] and a two-qubit quantum processor [7, 8], the *spin qubits* in semiconductors and *superconducting qubits* have claimed the leading positions in solid-state-based qubit platforms, which have been solidified more than ever through significant improvements in quantum gate fidelities [9–17]. For all the highlights these two platforms possess, spin and superconducting qubits have their own characteristic limitations. Single electron spin qubits in a quantum dot in isotopically enriched ^{28}Si devices have shown a dephasing time on the order of tens of microseconds far below the energy relaxation time in a high magnetic field environment ($\sim 1\text{ T}$), where the limiting factor was found to be charge noise [18]. When reducing the magnetic field to $\sim 100\text{ mT}$, the dephasing time of the spin qubit drops to a few microseconds and becomes limited by spin flips of residual ^{29}Si nuclei [19]. Superconducting qubits with reduced sensitivity to charge noise were found to perform better in terms of dephasing time, usually ranging from tens of microseconds to just over a hundred microseconds [20]. However, the relaxation time of a superconducting qubit barely exceeds half of a millisecond, which will ultimately limit the qubit dephasing [21]. In addition, the high coherence in superconducting qubits comes at a cost of increased footprint, rendering a difficult roadmap for up-scaling. After all these arguments, an experimental question becomes relevant, that is, does an intermediate nanoelectronic device exist, that can combine the best from both worlds? In this regard, a novel type of qubit, known as Andreev qubits, has emerged in recent years. It is encoded in the electron-like states emerging in a transparent few-modes Josephson weak link.

A Josephson weak link is an electronic device that is composed of two superconducting electrodes, connected via a non-superconducting segment. In a transparent few-modes Josephson weak link, superconducting quasiparticles

can undergo phase-coherent Andreev reflections at the interfaces to the superconducting electrodes, resulting in discrete energy levels bounded in a sub-micrometer-scale volume, as small as the weak link itself [22, 23]. Recently, experimental works have demonstrated the dynamics and coherent manipulation of these quasiparticle states in superconducting atomic point contacts [24] and epitaxial InAs/Al nanowire Josephson junctions [25, 26]. In the latter material platform, the strong intrinsic spin-orbit coupling has been utilized to unlock the spin degree of freedom, enabling control and readout of Andreev spin qubits [27]. The hallmark features of these fermionic states of being electrically controlled, small size, and carrying supercurrent make the semi-conducting nanowire-based Josephson junctions an interesting candidate for scalable Andreev qubits [28–33].

To fully exploit the potential of Andreev qubits, there are still several milestones to accomplish. First, a controllable exchange interaction of qubits is elementary to a quantum computer. It should feature a long range coupling scheme and a tunable interaction strength, forming a building block for two-qubit operations [6, 34]. So far, there has been only a single report on the coupling of an Andreev spin qubit to a superconducting transmon qubit [35]. However, the presented Andreev spin qubit resides in the same Josephson weak link, which is used to form the transmon qubit, thus depriving this approach of scalability. Furthermore, their exchange interaction is based on the physical proximity of the qubits and not an actual tunable parameter. In this thesis, we propose a long range coupling scheme for Andreev qubits using a superconducting cavity coupler, whose qubit-cavity interaction strength can be tuned by aligning the qubit frequency with respect to the cavity frequency. We will present the development of our superconducting cavity coupler in-depth and demonstrate long range coupling of two Andreev level qubits.

On the single qubit level, the coherence properties of Andreev qubits have not reached the state-of-the-art of solid-state-based qubits yet, with the latest studies pointing out a spin-specific limitation in dephasing time [27]. That naturally rises the question, is there a different semiconductor material, that features transparent semiconductor-superconductor interfaces, high crystal quality and perhaps spin-orbit coupling, but less nuclear spin magnetic field fluctuation? In the second part of the thesis, we will employ the Ge/Si core/shell nanowires, a group IV semiconductor with spin-orbit coupling, and establish Josephson weak links using this material, building the base for Andreev qubits in group IV semiconductors.

Outline of this thesis

Ch. 2 presents the theoretical concepts of Andreev bound states in semiconducting nanowire-based Josephson junctions, followed by the introduction

to the implementation of Andreev qubits using full-shell epitaxial InAs/Al nanowires. The control and readout of Andreev qubits presented in this thesis rely on the coupling to a superconducting microwave resonator. Ch. 3 provides an overview of the qubit-resonator coupling and concludes the theory part of this thesis. Ch. 4 presents the DC electrical characterization of full-shell epitaxial InAs/Al nanowire Josephson junctions. The electrical performance of these nanowire devices is evaluated in terms of junction transparencies. The extracted high transparency parameters encourage us to further proceed to fabricate the microwave chip. Ch. 5 thoroughly discusses the design considerations for the superconducting cavity coupler for Andreev qubits. From the experimental requirements, we derive design rules for each relevant electronic component, which are checked using numerical simulation tools. We then combine the knowledge about our full-shell epitaxial InAs/Al nanowire Josephson junctions and superconducting cavity coupler. In Ch. 6, we demonstrate the operation of the cavity coupler as a microwave spectroscopy tool and qubit state detector for individual NWJJ devices. In Ch. 7, we simultaneously couple both Andreev pair qubits to the cavity and demonstrate distant, strong coupling of two Andreev pair qubits. With the demonstration of the capability of our superconducting cavity coupler to entangle two Andreev pair qubits, we close the investigation of qubits formed with epitaxial InAs/Al nanowires. In Ch. 8, we motivate the use of Ge/Si core/shell nanowire Josephson junctions and demonstrate coherent manipulation of a superconducting gatemon qubit, that manifests Josephson supercurrent in these nanowire devices. In Ch. 9, we summarize the important experimental techniques, which are the backbone of the presented thesis, helping the readers to understand and reproduce the experiments. This thesis is concluded in Ch. 10 with a brief outlook of possible future experiments.

2 Andreev bound states in SNS Josephson junctions

Andreev bound states (ABSs) are the key mechanism for electrical transport in semiconducting nanowire-based Josephson junctions. In this chapter, we present the concepts of ABSs in a superconductor-metal-superconductor Josephson junction (SNS JJ). It is a condensed version of the Ch. 2-3 from the dissertation from Cyril Metzger in Ref. [36], in which we outline the essential microscopic processes investigated in this thesis. Sec. 2.1-2.4 introduce an intuitive picture of the occurrence of ABSs, followed by the implications of back-scattering, finite junction length and spin-orbit coupling (SOI). Hereafter, the implementation of Andreev qubits is discussed in Sec. 2.5, with focus on the material platform in Sec. 2.6.

2.1. Andreev reflection

We consider a system with a segment of normal metal that is in electrical contact with another segment of superconductor (Fig. 2.1a). The superconductor is described by a complex order parameter $\Delta = |\Delta|e^{i\delta}$, where $|\Delta|$ is the superconducting gap and δ the superconducting phase. In the normal metal, free electrons have the energy dispersion $E = \hbar^2 k^2 / 2m^*$, with k being the wave-vector and m^* the effective mass of the electron. For now, there is no mechanism to differentiate spin-up electrons from spin-down electrons such that the electron band is two-fold degenerate. In the ground state, all the fermionic states up to the electrochemical potential μ are filled by electrons, where μ is related to the Fermi wave-vector k_F by $\mu = \hbar^2 k_F^2 / 2m^*$.

Now, we consider a right-moving spin-up electron excitation e_1 in the normal metal with a wave-vector $k_1 = k_F + \delta k$ and energy $E_1 = \hbar^2 k_1^2 / 2m^*$, see Fig. 2.1b. A right-moving Cooper pair in the superconductor is generated with the e_1 incident on the metal-superconductor interface. The Cooper pair possesses a momentum of $2\hbar\delta k$, an energy of 2μ and charges with opposite spin orientations. To complete this process, e_1 has to pair up with a spin-down electron e_2 with $k_2 = -k_F + \delta k$ and $E_2 = \mu - \hbar^2 k_2^2 / 2m^*$ in the metal. The missing electron e_2 is equivalent to a left-moving spin-up hole excitation with k_2 and E_2 [37]. This process is known as Andreev reflection, discovered by A.F. Andreev in 1964, and describes the charge transfer of $2e$ across the metal-

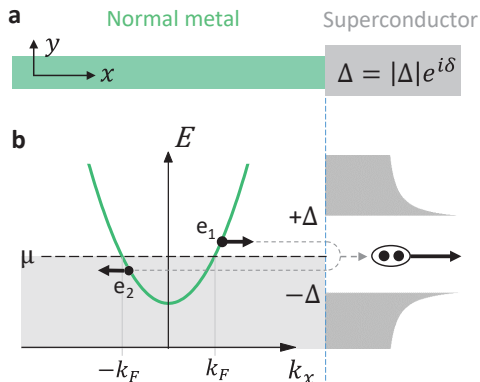


Figure 2.1. Andreev reflection. **a**, A metal-superconductor interface. The superconductor is characterized by the superconducting gap Δ and phase δ . **b**, At the interface, a right-moving electron e_1 in the gap pairs up with a left-moving electron e_2 , creating a right-moving Cooper pair in the superconductor and leaving a left-moving hole in the normal metal. Figure adapted from Ref. [36].

superconductor interface by retro-reflecting an electron with a low excitation energy ($E_1 - \mu < \Delta$) as a hole [22].

After explaining what happens before and after an Andreev reflection, let's regard what happens during an Andreev reflection. The superconducting order parameter Δ does not have a sharp boundary, it rather possesses a smooth transition into the normal metal over the coherence length $\xi = \hbar v_F / |\Delta|$, i.e., $\Delta(x)$. Upon approaching the superconductor, the right-moving electron becomes a quasiparticle with a fixed energy $E_{\text{qp}} = \sqrt{\epsilon(x)^2 + \Delta^2(x)} = \sqrt{(\hbar^2 \delta k(x)^2 / 2m^*)^2 + \Delta^2(x)}$ and a charge $-e \cdot \frac{\epsilon(x)}{E_{\text{qp}}}$. This formula shows that the wave-vector $\delta k(x)$ gradually reduces as $\Delta(x)$ increases towards the superconductor. Hence, the electron-to-hole conversion does not happen spontaneously at a certain distance to the interface and is rather a gradual process over a characteristic length scale ξ_{AR} , that depends on the energy of the impinging quasiparticle E_{qp} (Details in Sec. 2.1.2, [36]). It can be shown that the phase difference $\phi(E_{\text{qp}})$ between the right-going electron-like quasiparticle and the left-going hole-like quasiparticle depends on the particle energy and reads

$$\phi(E_{\text{qp}}) = -\arccos\left(\frac{E_{\text{qp}}}{|\Delta|}\right) - \delta. \quad (2.1)$$

For an impinging quasiparticle at μ ($E_{\text{qp}} = 0$), the Andreev reflection is accompanied by a phase shift of $\pi/2$. In the next section, we will discuss about the formation of ABSs.

2.2. Andreev bound states

Now, we consider a device with a segment of normal metal that is contacted with two segments of superconductor on both sides, featuring a superconducting phase of $-\delta/2$ and $\delta/2$ (Fig. 2.2a). We further assume that the normal metal is much shorter than the coherence length, $L \ll \xi$, and mean free path, $L \ll \lambda_{\text{MFP}}$. The former assumption neglects the phase acquired along the trip in the metal while the latter ensures that Andreev reflection is the only quasiparticle scattering mechanism. Fig. 2.2b illustrates the so-called ABS that arises from phase-coherent Andreev reflections of a quasiparticle at two interfaces. One also loosely speaks of a quasiparticle being trapped in the JJ [38]. The total acquired phase of this round-trip is [39]

$$\begin{aligned}\phi_{\text{tot}}^- &= \phi_L + \phi_R \\ &= \left(-\arccos\left(\frac{E_{\text{qp}}}{|\Delta|}\right) + (-\delta/2) \right) + \left(-\arccos\left(\frac{E_{\text{qp}}}{|\Delta|}\right) - \delta/2 \right) \\ &= -2\arccos\left(\frac{E_{\text{qp}}}{|\Delta|}\right) - \delta.\end{aligned}\quad (2.2)$$

Note that the additional phase from the superconductor is added with opposite signs for an electron-to-hole conversion and a hole-to-electron conversion. Similarly, we obtain a total phase of $\phi_{\text{tot}}^+ = -2\arccos(\frac{E_{\text{qp}}}{|\Delta|}) + \delta$ when we consider a right-move hole as the starting point. Because we are interested in energy levels that are associated with trapped quasiparticles in the junction, we look for solutions $E_{\text{qp}} = E_A(\delta)$, where the quasiparticle becomes itself again after two Andreev reflections. Hence, the total acquired phase should be a multiple of 2π . In the simplest case, $\phi_{\text{tot}}^\pm \stackrel{!}{=} 0$:

$$\Rightarrow E_A^\pm(\delta) = \pm|\Delta|\cos\left(\frac{\delta}{2}\right).\quad (2.3)$$

E_A^+ corresponds to the round-trip with the electron-like quasiparticle going to the left superconducting electrode and E_A^- to the round-trip with the electron-like quasiparticle going to the right superconducting electrode (Fig. 2.2c).

2.3. Effects of back-scattering and finite length

The Eq. (2.3) is associated with the energy level of two perfect ABSs without normal scattering events. In a realistic junction, Andreev reflection is not the

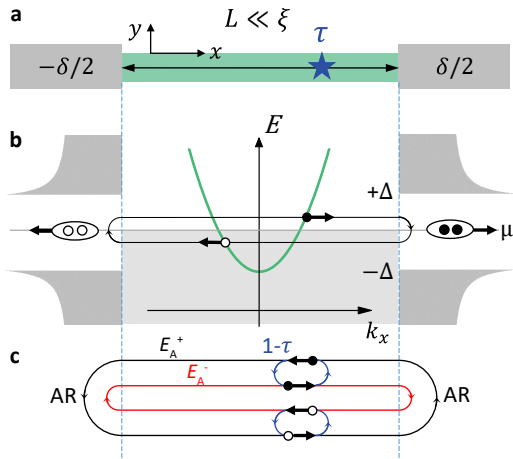


Figure 2.2. Andreev bound state. **a**, A short SNS JJ ($L \ll \xi$) with superconducting phases $-\delta/2$, $\delta/2$ at the electrodes. A star symbolizes scattering center in the normal metal, leading to a junction transparency τ . **b**, ABS with a right-moving electron-like quasiparticle. A right-moving Cooper pair (full circles) is generated in the right superconducting electrode while a left-moving hole pair (open circles) is generated in the left electrode. **c**, Two quasiparticle round-trips in the short SNS junction with the associated energy levels E_A^\pm . Figure adapted from Ref. [36].

only scattering process. An electron can as well be reflected as an electron in the normal metal due to impurities or at the interfaces. This normal reflection couples the quasiparticle round-trips $E_{\Lambda}^+(\delta)$ and $E_{\Lambda}^-(\delta)$, as illustrated in Fig. 2.2c. The probability is associated with $1 - \tau$, with τ being the transparency of the junction. With that, the Eq. (2.3) can be extended to [40]

$$E_{\Lambda}^{\pm}(\delta) = \pm|\Delta|\sqrt{1 - \tau\sin^2\left(\frac{\delta}{2}\right)} \quad (2.4)$$

to include normal reflections.

In the introduction of ABSs in Sec. 2.2, we assume that a quasiparticle does not acquire phase when traveling along the normal metal. This assumption is not valid when the quasiparticle dwells in the normal metal for a considerable time. The phase acquired by the quasiparticle over a length of L is $\frac{L}{\xi} \frac{E_{\text{qp}}}{|\Delta|}$. In case of a long junction ($L \gtrsim \xi$) or a highly energetic quasiparticle ($E_{\text{qp}} \gtrsim \Delta$), the phase acquisition can not be neglected. One can further embed the normal reflection into the problem, as treated in the Ref. [40]. The phase δ acquired at the metal-superconductor interface is then replaced by an effective phase α , taking a scatter potential at the position $x = a$ and the transparency τ of the junction into account:

$$\alpha = \arccos \left\{ \tau \cos(\phi) + (1 - \tau) \cos \left[\left(\frac{L - 2a}{\xi} \right) \left(\frac{E_{\text{qp}}}{\Delta} \right) \right] \right\}. \quad (2.5)$$

Finally, we obtain the formula for the total acquired phase ϕ_{tot}^{\pm} for a round-trip:

$$\phi_{\text{tot}}^{\pm} = -2 \arccos \left(\frac{E_{\text{qp}}}{|\Delta|} \right) \pm \alpha + 2 \frac{L}{\xi} \left(\frac{E_{\text{qp}}}{|\Delta|} \right). \quad (2.6)$$

To illustrate the ABSs under the effects of transparency and finite junction length, we now plot some Andreev energy levels as a function of the phase difference δ . Fig. 2.3 shows the numerically calculated positive ABSs ($E > 0$) using Eq. (2.6) for three different junction lengths ($L = 0\xi$, $L = 1.1\xi$, $L = 2.6\xi$). For each positive ABS at $E = E_{\Lambda}$, there is a negative ABS at $E = -E_{\Lambda}$ due to electron-hole symmetry. The dashed energy levels are associated to a junction with unity transparency, $\tau = 1$, whereas the solid energy levels correspond to $\tau = 0.7$. Normal reflection lifts the degeneracy at $\delta = \pi$ and couple states that arise from right-moving electron-like quasiparticles with that from right-moving hole-like quasiparticles. In case of a "zero"-length junction, we restore the results Eq. (2.4). At $\delta = \pi$, there is a gap of $2\Delta\sqrt{1 - \tau}$ between the positive ABS and negative ABS. As the junction length is increased above ξ , more ABS manifolds fall into the gap. For $L = 1.1\xi$, there are four manifolds (two positive, two negative), and for $L = 2.6\xi$, there are six manifolds (three positive, three negative). The energy of ABS of higher manifolds can

be computed using the condition $\phi_{\text{tot}}^{\pm} \stackrel{!}{=} 2\pi n$, with $n \geq 1$. The corresponding quasiparticles have such a high excitation energy, that a multiple of 2π is acquired along the path in the normal metal. Additional gaps at $\delta = 0$ open when the scatter potential is not placed in the middle of the normal metal segment (Here: $a = 0.3L$).

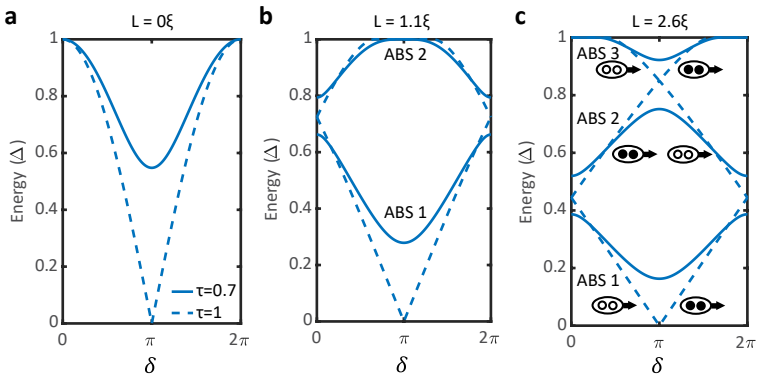


Figure 2.3. Realistic ABSs. Numerically calculated positive ABS energy levels in the gap Δ with (a) $L = 0\xi$, (b) $L = 1.1\xi$ and (c) $L = 2.6\xi$. Solid lines account for a scattering potential at $a = 0.3L$ and a junction transparency of $\tau = 0.7$. Dashed lines account a $\tau = 1$. The calculation is inspired by Ref. [36].

2.4. Spin-orbit coupling

When a charge particle moves in an electric field, it experiences an effective magnetic field that couples to its spin degree of freedom. This effect is known as spin-orbit coupling (SOI) and the corresponding Hamiltonian is written as

$$H_{\text{SO}} = \vec{\alpha} \cdot (\vec{\sigma} \times \vec{k}), \quad (2.7)$$

where $\vec{\alpha}$ is the SO coupling strength, $\vec{\sigma}$ is the vector of Pauli matrices in the spin space and \vec{k} is the electron wavevector. In solid state devices, one distinguishes between two types of SOIs. When the unit cell of the crystal itself lacks an inversion center, the crystal structure is known as bulk inversion asymmetric and can develop an intrinsic electric field. The corresponding SOI is known as *Dresselhaus type* [41]. On the other hand, the *Rashba type* SOI is associated with structural inversion asymmetry that arises from extrinsic electric potential such as externally applied gate voltages or crystal surfaces [42].

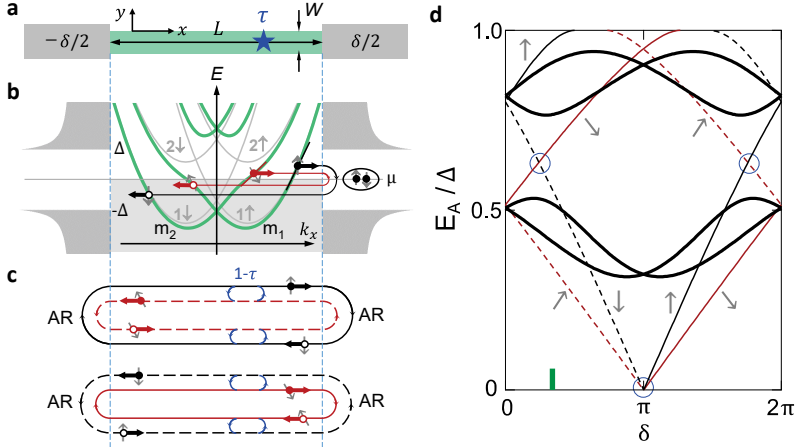


Figure 2.4. SOI splitting of ABSs. **a**, Similar schematic as Fig. 2.2a with a finite junction width W introducing transverse bands. **b**, A system with four transverse bands. SOI mixes transverse bands with opposite spins, yielding a spin texture dependent Fermi velocity, indicated with a different slope at $\sim \mu$. **c**, Quasiparticle round-trips that give rise to four ABSs. **d**, Energy diagram as a function of δ . For each δ value, there are four manifolds (two positive, two negative), each with two spin texture dependent ABSs. The lineshape of the thin lines corresponds to the lineshape of the round-trips in **c**. Back-scattering leads to avoided crossing of the ABSs at open circles, yielding the realistic states (thick black lines). Figure adapted from Ref. [36].

We consider a normal metal wire along the \vec{e}_x -direction and assume that the electric field due to inversion asymmetry is in the \vec{e}_z -direction. The Hamiltonian of the system can be written as

$$H = H_0 + H_{\text{SO}} = \frac{\hbar^2 \vec{k}^2}{2m^*} + \mathcal{U}(y, z) + \alpha \vec{e}_z \cdot (\vec{\sigma} \times \vec{k}), \quad (2.8)$$

with m^* being the effective mass of the electron in the solid and $\mathcal{U}(y, z)$ the confinement potential in the transverse direction. The confinement in the \vec{e}_y - and \vec{e}_z -direction leads to a discretization of k_y and k_z . By further assuming a harmonic potential $\mathcal{U}(y, z) = m\omega_0^2(y^2 + z^2)$, the terms in the Eq. (2.8), which are associated with the kinetic and potential energy, can be reformulated as a 2D quantum harmonic oscillator: $\hbar^2(k_y^2 + k_z^2)/2m^* + \mathcal{U}(y, z) = \hbar\omega_0(n + 1/2)$, with $n \in \mathbb{N}_0$ being the transverse band number. Eq. (2.8) then reads

$$H = \frac{\hbar^2(k_x - k_\alpha \sigma_y)^2}{2m^*} + \alpha k_y \sigma_x + \hbar\omega_0(n + \frac{1}{2}) - \frac{m^* \alpha^2}{2\hbar^2}, \quad \text{with } k_\alpha = \frac{m^* \alpha}{\hbar^2}. \quad (2.9)$$

The SOI and transverse confinement in combination lead to the follow effects:

- At first, the spin degeneracy of the electron band $E(k_x)$ is lifted yielding two parabolic bands, shifted with respect to each other by $\Delta k_x = k_\alpha$ (grey in Fig. 2.4b). A spin orientation along the \vec{e}_y -axis can be assigned to each of the band splitting (\uparrow, \downarrow).
- The spin-splitting occurs for all transverse bands. Hence, each band is characterized by the index $n\sigma_y$ with n being the transverse band number and σ_y the spin orientation along the \vec{e}_y -axis.
- The term $\alpha k_y \sigma_x$ mixes different transverse bands with opposite spins, leading to the green energy bands in Fig. 2.4b.

As a result of band mixing, the band $1 \downarrow$ hybridizes with the band $2 \uparrow$ and the band $1 \uparrow$ with the band $2 \downarrow$. At the avoided crossings, the electron spin is in superposition of \uparrow and \downarrow . Usually, the term "spin texture" is used for referring to the different spin superpositions.

We consider now the system with the lowest four transverse bands (Fig. 2.4b). When the chemical potential μ is aligned to a level, where avoided crossings occur due to band mixing, quasiparticles can have four round-trips with different Fermi velocities induced by different spin textures. Hereafter, normal scattering events can be introduced to the system again, as was done earlier in this chapter, to couple round-trips of right-moving electrons and left-moving electrons (Fig. 2.4c). Hence, SOI enriches the Andreev spectrum tremendously.

Fig. 2.4d shows a representative Andreev spectrum as a function of the superconducting phase difference δ . In total, there are four manifolds (two positive, two negative), each with two spin texture dependent ABSs. To understand it, we first regard the spectrum with perfect transparency ($\tau = 1$) at a

fixed δ , indicated by a green mark. The lower lying positive manifold (dashed thin lines) is formed by the two energetically more favorable left-moving electron round-trips, which are also dashed lines in Fig. 2.4c. Their energy levels are shifted with respect to each other because of the spin texture dependent Fermi velocities. The higher lying manifold (solid thin lines) has a slope with opposite signs and thus is associated with the two right-moving electron round-trips generating a supercurrent in opposite direction to the prior manifold. In this manifold, an additional phase of 2π is acquired by the quasiparticles after a round-trip. Similarly, the ABSs are shifted with respect to each other due to different Fermi velocities. Normal scattering events along the round-trips lead to avoided crossings indicated with open circles, yielding the realistic ABSs in thick solid lines.

2.5. Andreev level and Andreev spin qubits

The discrete energy spectrum of ABSs has been employed to realize qubits. It is fundamental to quantum computation that the qubit can be prepared in any linear combination of the ground state $|0\rangle$ and excited state $|1\rangle$. In the representation of a Bloch sphere, $|0\rangle$ can be at the north pole and $|1\rangle$ at the south pole (Fig. 2.5a). Any superposition state can be visualized as a vector on the Bloch sphere $|\Psi\rangle = \cos(\theta/2)|0\rangle + e^{i\phi} \sin(\theta/2)|1\rangle$.

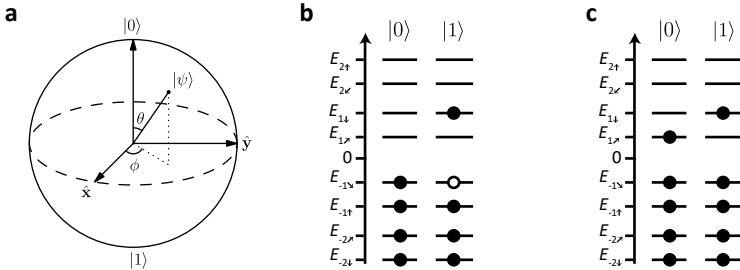


Figure 2.5. Andreev level and Andreev spin qubits. **a**, Bloch sphere representation of a qubit with the ground state $|0\rangle$ being at the north pole and $|1\rangle$ at the south pole. Many-body occupation of the Andreev spectrum for an Andreev level qubit (**b**) and an Andreev spin qubit (**c**). Full dots above $E = 0$ represent an electron-like quasiparticle excitation and hollow dots below $E = 0$ represents a hole-like quasiparticle excitation.

Two kinds of qubits have been realized using the Andreev spectrum. Fig. 2.5b-c show the definition of the qubit ground and excited states in the represen-

tation of the Andreev spectrum for the two kinds of Andreev qubit. In the *Andreev level qubit*, the excited state is formed by an electron-like quasiparticle excitation above $E = 0$ and a hole-like quasiparticle excitation below $E = 0$ while the qubit ground state has all the negative ABSs occupied. The Andreev pair qubit frequency then reads $f_e = (E_{1\downarrow} - E_{-1\downarrow})/h = (E_{1\downarrow} + E_{1\uparrow})/h$. In the *Andreev spin qubit*, the qubit ground state has an electron-like quasiparticle excitation from the beginning. The qubit excited state is formed by having the quasiparticle excitation in an ABS associated with a different spin texture. Here, the qubit frequency is given by $f_o = (E_{1\downarrow} - E_{1\uparrow})/h$.

Based on the number of quasiparticle excitations, one assigns the term *even parity* to the Andreev level qubit and *odd parity* to the Andreev spin qubit. A parity switching happens when the junction traps or detraps a quasiparticle, leading to a leakage out of the computational subspace.

2.6. Full-shell epitaxial InAs/Al nanowires

Full-shell epitaxial InAs/Al nanowires are the material platform used for forming Andreev qubits in this thesis (cross-section in Fig. 2.6a). These nanowires were grown in the wurzite crystal structure using molecular-beam epitaxy technique (MBE) by Prof. P. Krogstrup in the Niels Bohr Institute [43]. After the growth of the InAs nanowires, Al was grown by angled deposition within the MBE chamber, covering each facet of the nanowires with an Al shell with a domain-matched and impurity free superconductor-semiconductor interface (Fig. 2.6b). The epitaxial superconductor-semiconductor interface is often associated with the suppression of the so-called "sub-gap" states, which appear below the superconducting gap Δ and can be a source of unwanted interaction with the intentional formation of bound states [44]. Further characteristics of the InAs/Al nanowires are a quasi-1D confinement and a large SOI. A number of findings quickly followed after the release of this material platform, demonstrating qubit applications [25, 45] and exotic properties in the superconductivity such as the emergence of Majorana bound states [46, 47] and skewed current-phase relations [48]. All these observations have highlighted the reliability and robustness of these nanowires, motivating us to realize our experiments on this material platform.

To fabricate a Josephson junction using the full-shell InAs/Al nanowires, a short segment of the Al-shell has to be stripped away. The top panel of Fig. 2.6c shows a scanning electron micrograph of a typical nanowire Josephson junction (NWJJ) device after the wet etching process, which possesses a semiconductor segment of ~ 150 nm with a narrower diameter. In the lower schematic, the superconductor-semiconductor interface, that is cylindrical around the nanowire's circumference, is indicated in blue.

This concludes our introduction to ABS in semiconducting nanowire-based

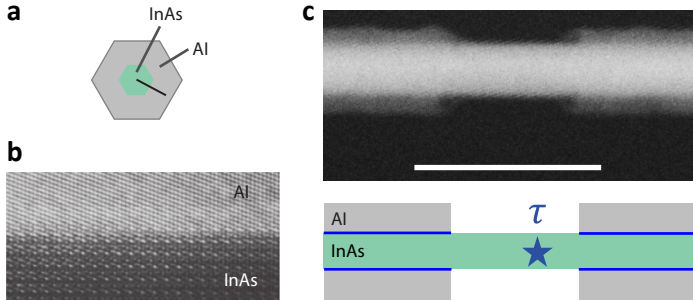


Figure 2.6. Full-shell epitaxial InAs/Al nanowires **a**, Schematic transversal cross-section of the epitaxial InAs/Al nanowire. Al is in grey and InAs is in green. **b**, Transmission electron micrograph showing the epitaxial InAs/Al interface. **c**, (Top) Scanning electron micrograph of a NWJJ. The Al shell is stripped in the middle. The scale bar is 200 nm. (Bottom) A schematic longitudinal cross-section of the NWJJ. Superconductor-semiconductor interfaces are indicated in blue.

JJs with SOI as a novel platform for solid state quantum computation. In the next chapter, we will see how Andreev qubits can be manipulated and read out.

3 Integration of superconducting resonators with Andreev qubits

Circuit quantum electrodynamics (cQED) is the study of well-designed, non-linear superconducting circuits, usually known as "artificial atoms", with confinement of electromagnetic fields in the microwave frequency domain [49–52]. Originally, leading the field of research for quantum information processing using robust, coherent superconducting qubits, cQED has also advanced the development of linear superconducting microwave resonators as an exploratory toolkit to discover new phenomena in novel solid-state devices [53, 54]. In fact, the planar superconducting microwave resonator on silicon substrates lies in the core of the study of the few-mode Josephson elements [24, 38, 55–57].

In this chapter, we will introduce the qubit-resonator coupled system which contains a superconducting resonator and a few-mode Josephson junction. First, Sec. 3.1 and 3.2 present the linear quantized LC -circuit and then the more specific quarter-wavelength transmission line type resonator. After that, the radio-frequency superconducting quantum interference device (RF-SQUID) is described in the Sec. 3.3. Hereafter, the inductively coupled SQUID-resonator system is presented in Sec. 3.4, merely capturing the essential aspects. A more detailed derivation of the coupling scheme can be found in the Sec. 4.2 in the dissertation from Cyril Metzger [36]. The final section discusses the implication of qubit-resonator coupling in the dispersive limit, a limit that allows fast, non-demolition measurement of the qubit state.

3.1. Hamiltonian description of superconducting resonators

We consider a non-dissipative parallel circuit composed of an inductance L_r and a capacitance C_r , as illustrated in the Fig. 3.1a. The capacitive energy stored in the circuit is given by the accumulated charge Q on the capacitor plates and reads $E_C = Q^2/2C_r$. Similarly, the inductive energy is related to the phase drop Φ across the inductance as $E_L = \Phi^2/2L_r$. Because Q and Φ are canonically conjugated variables, the system can be treated quantum mechanically by replacing the classical variables (Q, Φ) with corresponding

operators $(\hat{Q}, \hat{\Phi})$ [58]. The Hamiltonian of the quantum LC -circuit reads [49]

$$\hat{H} = \frac{\hat{Q}^2}{2C_r} + \frac{\hat{\Phi}^2}{2L_r} \quad (3.1)$$

with the canonical commutator relation $[\hat{\Phi}, \hat{Q}] = i\hbar$. Because the Hamiltonian Eq. (3.1) is equivalent to a quantum harmonic oscillator, we can introduce the creation operator \hat{a}^\dagger for a quantum harmonic oscillator and express it in terms of $\hat{\Phi}$ and \hat{Q} with

$$\hat{a}^\dagger = \frac{1}{\sqrt{2\hbar}} \left(\sqrt{\frac{C_r}{L_r}} \hat{\Phi} + i\sqrt{\frac{L_r}{C_r}} \hat{Q} \right). \quad (3.2)$$

The Hamiltonian for the quantum LC -circuit then reads

$$\hat{H} = hf_r \left(\hat{a}^\dagger \hat{a} + \frac{1}{2} \right), \quad (3.3)$$

where $f_r = (2\pi\sqrt{L_r C_r})^{-1}$ is the resonance frequency, usually in the few GHz range, and h the Planck's constant. The eigenenergies are plotted as a function of the flux Φ across the inductance in Fig. 3.1b, with the parabolic inductive energy $E_L(\Phi)$. The levels are discrete and equidistant. When excited with microwave at f_r , the quantum LC -circuit starts to resonate and populate the excited states. The number of excitations in the quantum LC -resonator is also loosely referred to as the photon number.

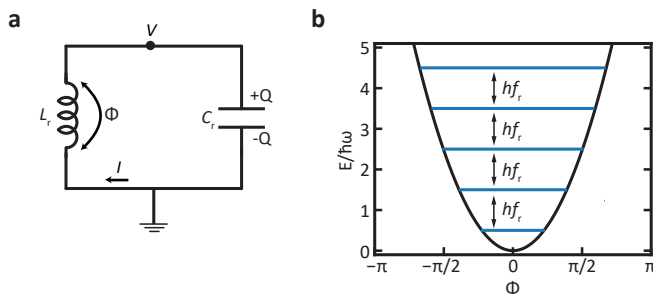


Figure 3.1. Non-dissipative LC -circuit. **a**, LC -circuit with charge Q on the capacitance and flux drop Φ across the inductance. **b**, Energy level of the quantized LC -circuit as a function of the flux Φ across the inductance. Figures adapted from [59].

A realistic resonator is characterized by both the resonance frequency f_r and photon energy decay rate κ . There are different energy relaxation paths which lead to a non-zero κ . Usually, one distinguishes between the intrinsic

κ_i and coupling κ_c decay rates. While κ_i quantifies the photon energy decay into unwanted loss channels, κ_c quantifies the wanted decay into the readout circuit. The total photon energy decay rate can be obtained by adding the individual contributions $\kappa = \kappa_i + \kappa_c$ [60]. Equivalently, one can define the resonator's quality factor $Q = 2\pi f_r / \kappa$ and distinguish between the intrinsic $Q_i = 2\pi f_r / \kappa_i$ and coupling $Q_c = 2\pi f_r / \kappa_c$ quality factors.

The quantized *LC*-resonator can be realized in many different designs and material platforms. One of the common constructions uses a superconducting planar transmission line geometry of finite length with deterministic boundary conditions on highly resistive substrates. The boundary conditions imposed by the geometry lead to a confinement of electromagnetic fields. The fields are discretized into a set of modes with distinct frequencies, where each mode can be thought of as an harmonic oscillator by itself.

3.2. Quarter-wavelength transmission line resonator

Among different on-chip planar transmission line resonator types, the quarter-wavelength coplanar transmission line resonator was the first used geometry for Andreev level qubits [24]. It is a transmission line of length L with a characteristic impedance Z_0 . One end of the transmission line is opened and the other end is shorted to the ground (Fig. 3.2). In the figure, the coplanar transmission line resonator is symbolized by the coaxial cable, featuring a center conductor that is surrounded by a cylindrical ground. With these boundary conditions, a current can not flow across the open end whereas a voltage can not build up at the short end. This gives rise to the discretization of the electromagnetic fields with a wavelength λ_n determined by the length of the transmission line and mode number $n \in \mathbb{N}_0$, $\lambda_n = 2L / (n + 1/2)$. The term quarter-wavelength emphasizes the fact that the fundamental mode ($n = 0$) is quarter-wavelength long, $L = \lambda_0 / 4$. It manifests a voltage anti-node at the open end and a current anti-node at the short end, as illustrated in Fig. 3.2. The current and voltage oscillates at the frequency $f_n = \nu / \lambda_n$, where ν is the speed of light in the transmission line.

The so-formed transmission line resonator can be excited using microwave sources. The excitation is typically coupled either capacitively to the open end or inductively to the short end of the transmission line, as displayed in the grey dashed boxes in Fig. 3.2. The average number of circulating photons on the resonator reads [61]

$$\langle \hat{n} \rangle = \langle \hat{a}^\dagger \hat{a} \rangle = \frac{2}{\hbar f_r^2} \frac{Z_{\text{env}}}{Z_R} \frac{Q^2}{Q_c} P_{\text{exc}}, \quad (3.4)$$

where P_{exc} is the applied microwave power at the resonator, Z_{env} the environmental impedance seen by the resonator, Z_R the resonator impedance, Q is the resonator's total quality factor and Q_c the coupling quality factor.

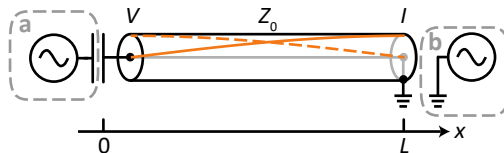


Figure 3.2. Quarter-wavelength transmission line resonator. The voltage and current are distributed along the wire according to the boundary conditions. The resonator can be excited capacitively through the open end (a) or inductively through the short end (b).

Because of the state-to-current conversion which comes naturally with ABSs, Andreev qubits are usually located at the resonator’s current anti-node while the resonator is excited at the voltage anti-node.

3.3. RF SQUID

To study the wide range of the Andreev spectrum, tunability of the superconducting phase difference δ across the NWJJ is needed. The superconducting phase difference of a JJ can be set with the junction embedded in a so-called *radio frequency superconducting quantum interference device* (RF SQUID). It is a continuous superconducting ring that is interrupted by the junction at one point, as displayed in Fig. 3.3a. In this arrangement, an out-of-plane magnetic field B penetrates the enclosed area A and generates a threading flux $\Phi = B \cdot A$. Because the superconducting order parameter in the ring has to be identical after a round-trip, the total phase drop ϕ_{tot} around the ring should add up to a multiple of 2π . Realistically, we need to further consider a loop inductance L_{loop} that accounts for the inductance of the superconducting ring and a loop current $I(\delta)$. Fig. 3.3b displays the equivalent circuit for the RF SQUID. The periodic flux leads to a boundary condition that reads [62, 63]

$$\phi_{\text{tot}} = \delta + \frac{2\pi}{\phi_0} L_{\text{loop}} I(\delta) - \frac{2\pi}{\phi_0} \Phi \stackrel{!}{=} 2\pi n. \quad (3.5)$$

A large loop inductance leads to hysteresis in $\delta(\Phi)$ due to the so-called screening effect in the SQUID, see Sec. 2.3.2 in [64]. A usual practise to overcome this problem is to design a sufficiently small L_{loop} such that most of the external flux bias drops across the junction [65]. In that limit, there is a linear dependence between the external flux bias and the superconducting phase difference that reads

$$\delta \approx \frac{2\pi}{\phi_0} (B \cdot A). \quad (3.6)$$

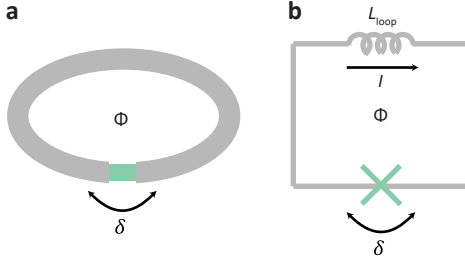


Figure 3.3. RF SQUID with a Josephson junction. **a**, Schematic of an RF SQUID. The superconducting loop (grey) is interrupted by the JJ (green). The superconducting phase difference δ across the weak link depends on the threading magnetic flux Φ . **b**, Equivalent circuit of the RF SQUID. The inductance of the superconducting loop is modelled as a lumped element inductance L_{loop} .

The RF SQUID is usually mutually or inductively coupled to a tank circuit for measurement, hence the adjunct *radio frequency* [66].

3.4. Inductive coupling

After treating the resonator and NWJJ as two separate systems, the coupled system is now described. For that, we consider an inductively coupled SQUID-resonator system, see the schematic and equivalent circuit in Fig. 3.4. The SQUID composed of the NWJJ and a superconducting loop is connected to a small portion of the resonator inductance l_s with $l_s/L_r \ll 1$. We recall that the resonator is fully described by the Hamiltonian eq. (3.3):

$$\hat{H}_r = hf_r(\hat{a}^\dagger \hat{a} + \frac{1}{2}). \quad (3.7)$$

On the other hand, a superconducting phase difference dependent Hamiltonian for the ABSs in the NWJJ can be constructed, $\hat{H}_{\text{JJ}}(\delta)$. Its eigenenergies are subject of Ch. 2. We assume that the resonator is in the ground state. The zero-point fluctuation of the resonator then generates a phase fluctuation across the weak link that reads [36]

$$\delta_{\text{zfp}} = \frac{l}{L} \sqrt{\frac{\pi Z_r}{R_Q}}, \quad (3.8)$$

where $Z_r = \sqrt{L_r/C_r}$ is the resonator impedance and $R_Q = h/4e^2$ the quantum resistance. Because of the small fluctuation amplitude, the Hamiltonian of the

coupled system can be approximated by an expansion at a flux bias value δ_0 to the second order as

$$\hat{H}_{\text{tot}}(\delta_0) \approx \hat{H}_r + \hat{H}_{\text{JJ}}(\delta_0) + \delta_{\text{zp}} \hat{H}'_{\text{JJ}}(\delta_0)(a + a^\dagger) + \frac{\delta_{\text{zp}}^2}{2} \hat{H}''_{\text{JJ}}(\delta_0)(a + a^\dagger)^2, \quad (3.9)$$

where $\hat{H}'_{\text{JJ}}(\delta_0) = d\hat{H}_{\text{JJ}}(\delta_0)/d\delta$ is the first derivative and $\hat{H}''_{\text{JJ}}(\delta_0) = d^2\hat{H}_{\text{JJ}}(\delta_0)/d\delta^2$ the second derivative of the NWJJ Hamiltonian with respect to the phase difference δ . It becomes clear that the ABS-resonator coupling is manifested in a change of the energy of the total system induced by the zero-point flux fluctuation of the resonator.

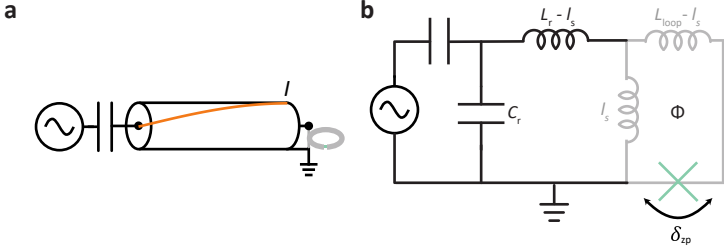


Figure 3.4. Inductively coupled SQUID-resonator system. **a**, A schematic of a quarter-wavelength transmission line resonator coupled to an RF SQUID. The current amplitude profile is plotted in orange. **b**, Equivalent circuit of the hybrid system with resonator capacitance C_r and inductance L_r . A small portion of the resonator inductance l_s defines the coupling to the SQUID. The resonator's ground state generates a zero-point flux fluctuation δ_{zp} across the NWJJ leading to the SQUID-resonator coupling.

One can further derive the shift of the resonance frequency $\delta f_{r,i}$ due to an ABS [36]. Assuming $|i\rangle$ is an ABS with the eigenenergy $E_i|i\rangle = \hat{H}_{\text{JJ}}|i\rangle$, then $|-i\rangle$ is also an ABS with eigenenergy $-E_i$ due to electron-hole symmetry. The resonance shift reads [67]

$$\begin{aligned} \frac{h\delta f_{r,i}}{\delta_{\text{zp}}^2} &= \underbrace{E_i''}_{2.\text{order}} + \sum_{i \neq j} |\langle i|\hat{H}'_{\text{JJ}}|j\rangle|^2 \left(\underbrace{\frac{2}{E_j - E_i}}_{2.\text{order}} - \underbrace{\frac{1}{E_j - E_i + hf_r} - \frac{1}{E_j - E_i - hf_r}}_{1.\text{order}} \right) \\ &= E_i'' + \sum_{i \neq j} \frac{\hbar^2 g_{ij}^2}{\delta_{\text{zp}}^2} \mathcal{V}_{ij}. \end{aligned} \quad (3.10)$$

The two f_r -dependent terms result from the first order expansion while the other two terms result from the second order expansion. The frequency shift

has two contributions. The first contribution is the term before the sum bracket and arises from the curvature of the ABS $|i\rangle$. The remaining three terms in the sum bracket, forming the second contribution, account for all other ABSs that couple to the ABS $|i\rangle$ via a coupling current matrix element $|\langle i|\hat{H}'_{JJ}|j\rangle|$. The coupling strength between an Andreev transition $j \rightarrow i$ and the resonator is introduced in the second line of the equation as $g_{ij} = \delta_{zp}|\langle i|\hat{H}'_{JJ}|j\rangle|/\hbar$.

After establishing the shift of resonance frequency induced by one ABS, it is straightforward to compute the resonance frequency shift for any many-body occupation of an Andreev spectrum. In general, the state index i is replaced by $i\sigma$, where $i < 0$ ($i > 0$) accounts for ABSs below (above) $E = 0$ and σ for the spin degree of freedom. An interesting case is the resonance shift due to the many-body ground state $|g\rangle$, which is also the ground state of the Andreev level qubit, occupying all negative ABSs and vacating all positive ABSs. The resonance frequency shift for the many-body ground state reads (p. in [36])

$$\frac{\hbar\delta f_{r,|g\rangle}}{\delta_{zp}^2} = \frac{1}{2} \left(\sum_{i<0,\sigma} E''_{i\sigma} + \sum_{\substack{i<0,\sigma \\ j>0,\sigma'}} \frac{\hbar^2 g_{i\sigma,j\sigma'}^2}{\delta_{zp}^2} \mathcal{V}_{i\sigma,j\sigma'} \right). \quad (3.11)$$

The first sum accounts for the curvature of all the occupied states whereas the second sum results from the coupling of each occupied state at $E < 0$ to all unoccupied states at $E > 0$. Finally, the resonance frequency shift for an arbitrary many-body occupation $|\Psi\rangle$ can be expressed as

$$\delta f_{r,|\Psi\rangle} = \delta f_{r,|g\rangle} + \sum_{i>0,\sigma} [n_{i\sigma} \delta f_{r,i\sigma} - (1 - n_{-i\sigma}) \delta f_{r,-i\sigma}], \quad (3.12)$$

where $n_{i\sigma} \in \{0, 1\}$ indicates the occupation of the ABS $i\sigma$.

In general, the coupling between the ABS and resonator is distinguished between *adiabatic*-, *dispersive*- and *resonating*-type, depending on the ratio of the qubit-resonator energy detuning and coupling strength $(|E_j - E_i| - \hbar f_r)/\hbar g_{ij}$. In the *adiabatic* limit, the qubit and resonator frequencies are far detuned such that the resonance frequency mainly shifts due to the second order term of the expansion. When the Andreev transition energy is much greater than the resonance frequency $|E_j - E_i| \gg \hbar f_r$, e.g., for the pair transition at $\delta = 0$, the current matrix element vanishes, further simplifying the formula to $\frac{\hbar\delta f_{r,i}}{\delta_{zp}^2} \approx E''_{i\sigma}$. In the *resonating* limit $|E_j - E_i| = \hbar f_r$, the Andreev transition is under continuous energy exchange with the cavity photon. It results in the occurrence of a symmetric and an anti-symmetric entangled matter-light state with an energy difference of $2\hbar g_{ij}$.

3.5. Dispersive limit

When the Andreev transition frequency is a few g_{ij} detuned from the resonator frequency, an interesting case arises that is known as the *dispersive* limit. Superconducting qubits are usually dispersively coupled to a superconducting resonator for non-demolition qubit state readout[68].

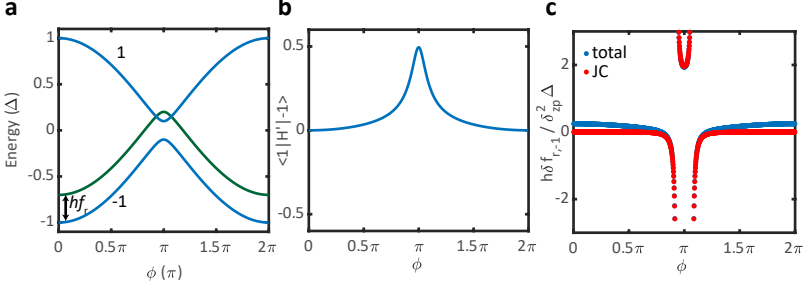


Figure 3.5. Energy diagrams of the ABS-resonator hybrid system. **a**, The energy spectrum of one ABS with the resonator energy level that is offset by hf_r from the ground state. **b**, Coupling current matrix element between the ABS $| - 1 \rangle$ and $| 1 \rangle$. **c**, Resonance frequency shift computed using the coupling Hamiltonian with both the first and second order terms ("total") and with only the first order terms ("JC"). In the dispersive limit, the first order terms are sufficient to capture the frequency shift.

To illustrate this regime, we consider two ABSs in the zero-length limit with a transparency of 0.99. The coupling current matrix element can be analytically computed using $\langle 1|H'_{JJ}(\delta)| - 1 \rangle = \frac{\Delta\sqrt{1-\tau}}{2} \left(\frac{\Delta}{E_{\Lambda}^{\dagger}(\delta)} - \frac{E_{\Lambda}^{\dagger}(\delta)}{\Delta} \right)$ [67]. The shift of the resonance as a function of δ can then be computed using the Eq. (3.10), by inserting $\langle 1|H'_{JJ}(\delta)| - 1 \rangle$, $E_{-1}(\delta)$, $E_1(\delta)$ and hf_r . Figure 3.5a shows the energy of the ABSs as a function of the superconducting phase difference δ . The number 1 (-1) denotes the ABS above (below) $E = 0$. Additionally, the resonator transition is plotted in green. The coupling current is shown in Figure 3.5b. It increases as both ABSs approach each other. The analytically computed resonance frequency shift for the ABS ground state is plotted in Figure 3.5c, as well as a function of δ . A divergence of the resonator frequency is expected as the Andreev transition frequency approaches the photonic transition frequency. The red curve, labelled as "total", uses the full expression Eq. (3.10) and the blue curve, labelled as "JC", only uses the first order terms in the expansion. The region where the red curve is in good agreement with the blue curve is identified as the *dispersive* limit. In fact, the red curve is the

result of the well-known Jaynes-Cummings model. It describes the interaction between a superconducting resonator and a generic qubit ($|g\rangle, |e\rangle$) in the form of [69, 70]

$$\hat{H}_{\text{JC}} = \hbar f_{\text{r}}(\hat{a}^\dagger \hat{a} + \frac{1}{2}) + \frac{\hbar f_{\text{qb}}}{2} \hat{\sigma}_z + \hbar g(\hat{a} \hat{\sigma}_+ + \hat{a}^\dagger \hat{\sigma}_-), \quad (3.13)$$

where f_{qb} is the qubit frequency, $\hat{\sigma}_z = |e\rangle\langle e| - |g\rangle\langle g|$ is the inversion operator and $\hat{\sigma}_\pm$ the raising (lowering) operator of the qubit. The latter two terms describe the energy exchange between the resonator and qubit with a coupling strength g . This is very convenient as it implies that control and readout techniques previously developed for superconducting qubits can be transferred to the Andreev qubits [49].

4 DC transport measurement of full-shell epitaxial InAs/Al nanowire Josephson junctions¹

Epitaxial InAs/Al nanowires are the first semiconducting nanowire material in which the application as Andreev qubits was demonstrated. These nanowires feature highly transparent semiconductor-superconductor interfaces, gate tunable charge carrier density and strong spin-orbit coupling. A reliable routine to fabricate highly transparent Josephson junctions (JJs) using these nanowires is therefore key technology. Among all the fabrication steps, the etching of nanowire's Al shell turned out to be least reproducible, manifesting in variable junction lengths and sharpness of the Al edges. The existing Al etch recipe in the nanoelectronics lab was adapted and modified, where the use of Microposit MF-321 developer as Al etchant was replaced by Transene type D [64]. The replacement of etchant was motivated by cleaner junctions and sharper Al edges. The Al etch recipe can be found in Sec. 9.1.

In Ref. [71], Goffmann *et al.* have developed a quantitative understanding of the channel numbers and transparencies in an epitaxial InAs/Al nanowire Josephson junction (NWJJ) by analysing its *IV*-characteristics. This motivated us to employ DC transport measurement techniques to test the performance of these NWJJs, before integrating them to microwave circuits. The full-shell epitaxial InAs/Al NWJJ device is described in Sec. 4.1, followed by the description of the cryogenic measurement techniques in Sec. 4.2. The study of the Josephson supercurrent is presented in Sec. 4.3. The measured multiple Andreev reflection features are discussed in Sec. 4.4, resulting in an estimation of channel transparencies in Sec. 4.5. The last section concludes our findings.

4.1. Device

Full-shell epitaxial InAs/Al NWJJs are fabricated on an undoped Si wafer with 160 nm thermally grown SiO₂ oxide. An Al segment of ~ 150 nm is stripped by wet etching technique. Subsequently, NbTiN is sputtered on the

¹This experiment was conducted with Alexei Orekhov, a semester project student from the Chalmers University of Technology. L.Y. Cheung and A. Orekhov shared the device fabrication, measurement and data analysis.

NWJJ after removal of the surface AlO_x by means of Ar-milling. Two side gates (Ti/Au) are evaporated flanking the semiconductor region. A scanning electron micrograph of the NWJJ is shown in Fig. 4.1-Fig. 4.2, together with the measurement setups. The device was measured in a dilution refrigerator at 20 mK.

4.2. Measurement techniques

The NWJJ is contacted with four superconducting probes on the chip in a quasi-four-probe measurement scheme. We consider two types of transport measurement. In the voltage bias measurement, a DC voltage bias and a small AC voltage modulation are combined with a 1:4 transformer and subsequently divided by a 1:1000 voltage divider before reaching the device (Fig. 4.1). For finite device resistance, the voltage bias and modulation generate a current that can be amplified with a room temperature IV -converter. The output of the IV -converter is then routed to the lock-in or a multimeter for data acquisition. The side gates are connected to the DC voltage source with a 1 M Ω resistor. All lines are heavily filtered with room temperature π -filters and LC low-pass filters at ~ 100 mK with a cutoff frequency of 80 MHz. Usually, this measurement scheme is used when the device has the highest resistance among all the resistances along the line.

On the other hand, the device can as well be measured in the current bias configuration at high carrier doping in the semiconductor. By inserting a large room temperature resistor R between the voltage source and NW, a current is generated by the ratio of voltage and resistance $I = V/R$. Two other probes across the NW can be connected to a differential voltage amplifier followed by a lock-in or multimeter for measuring the voltage across the NW (Fig. 4.2).

4.3. Josephson current

We now show the gate dependent supercurrent of our nanowire. Fig. 4.3 shows the differential resistance R , measured with a lock-in, as a function of the side gates V_G in the current bias configuration. The differential resistance is ~ 10 k Ω in the normal state (at high bias), it abruptly drops to lower values at lower bias. The current value, at which the abrupt drop happens, depends on the gate voltage. The drop in resistance indicates the onset of a Josephson current I_c [78]. For a highly transparent SNS JJ, quasiparticles below the superconducting gap ($E_{qp} < \Delta$) undergo phase coherent Andreev-reflections at the interfaces, transferring Cooper pairs from one electrode to the other. Hence, a dissipationless current can flow through the junction. Fig. 4.3c shows cross-sections at three different gate voltage values. In the normal state ($|I| > I_c$), the resistance decreases at higher gate voltages due

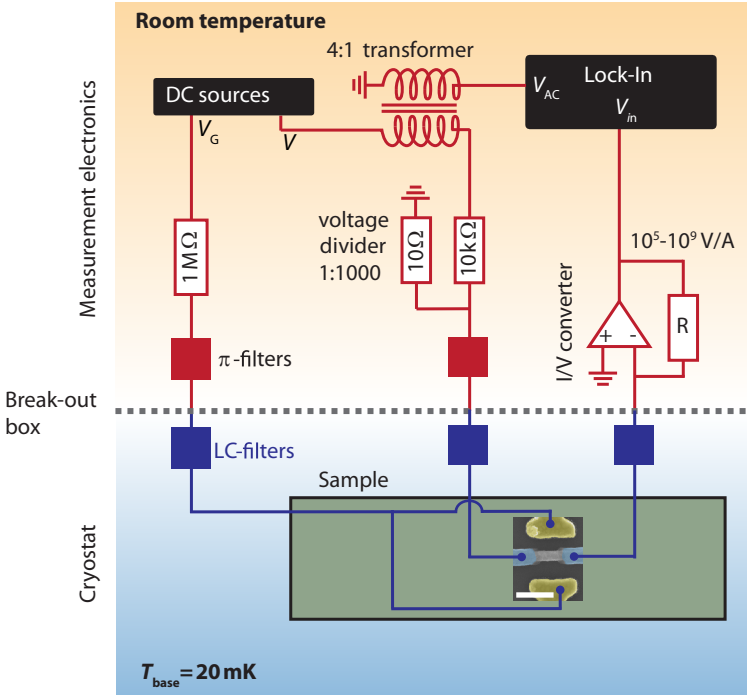


Figure 4.1. Setup for voltage bias measurement. The AC and DC voltage are combined with a 4:1 transformer before reaching the device through a 1:1000 voltage divider. On the other side of the nanowire, an I/V-converter is used to amplify the signal. The side gates are connected to a DC voltage source via a $1M\Omega$ resistor. All lines are filtered with room temperature π -filters and rf-filters at ~ 100 mK ($f_{cutoff} \approx 80$ MHz). A scanning electron micrograph of the NWJJ device is shown. The scale bar is 200 nm. Figure adapted from [72–77].

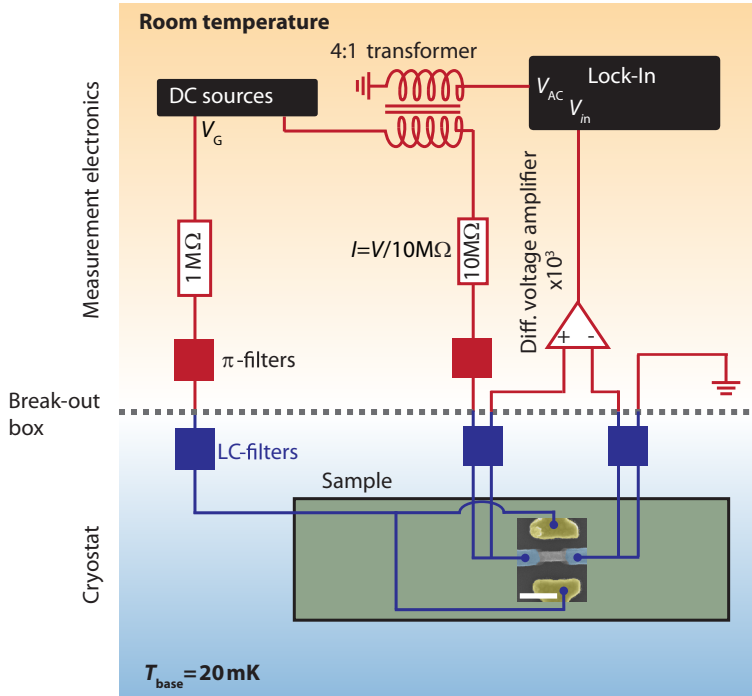


Figure 4.2. Setup for current bias measurement. Similar as the Fig. 4.1. For the current bias measurement, the voltage divider is replaced with a $10\text{M}\Omega$ resistor and the IV -converter replaced with a differential voltage amplifier. Figure adapted from [72–77].

to increased number of charge carriers in the semiconductor. The resistance in the Josephson branch ($|I| < I_c$) is finite. This can be caused by voltage fluctuation generated by finite temperature [79]. Moreover, I_c increases at higher V_G and reaches 20 nA at $V_G = 10$ V.

Fig. 4.3d shows the extracted $I_c R_n$ -product as a function of V_G . I_c is estimated as the first positive current bias value that features $R = 1\text{k}\Omega$ and R_n is estimated as the differential resistance at $I = 0.2\ \mu\text{A}$. One observes that the $I_c R_n$ -product has an overall upwards trend and reaches $\sim 40\ \mu\text{V}$ at $V_G = 5$ V. For a short clean metallic weak link at $T \ll T_c$, an $I_c R_n = \pi\Delta/e$ is expected [80]. Considering the bulk Al gap $\Delta_{\text{Al}} \approx 210\ \mu\text{eV}$ [81], the measured $I_c R_n$ -product is only a fraction of the expectation value, indicating that the NWJJ is not in the short clean limit. The reduction of $I_c R_n$ -product can be explained by finite length effects, as the I_c falls exponentially with the junction length l as $e^{-l/\xi}$, with ξ being the coherence length of the proximity effect in the semiconductor.

4.4. Multiple Andreev reflections

We will now investigate resonance features in the normal branch. Resistance peaks are observed above the Josephson current, appearing at different I as a function of V_G . Overall, they follow the increase of the Josephson current and appear at higher bias current when V_G is increased. To understand these resistance peaks, the differential conductance is computed as the inverse of the differential resistance $G = R^{-1}$. The voltage drop V across the junction is obtained by numerically integrating the differential resistance, $V = \sum_i R_i \cdot \Delta I_i$ and $V(I_0) = 0$, with $\Delta I_i = I_{i+1} - I_i$ being the bias current difference between two adjacent data points. Fig. 4.4a shows the computed differential conductance G as a function of I and V_G . The same dataset with a converted voltage axis V is plotted in Fig. 4.4b. The modulating conductance peaks in the current axis appear to be at fixed voltage values. Fig. 4.4c shows a linecut at $V_G = 4.5$ V. The conductance peaks are interpreted as signature of multiple Andreev reflections (MARs) [82, 83].

In voltage bias measurement, when an electron-like quasiparticle travels from one superconducting electrode to the other, it gains an energy of eV . At a transparent superconducting-semiconducting interface, the electron-like quasiparticle can be Andreev reflection as a hole-like quasiparticle, travelling back, again with a gain of eV . For highly transparent junctions, this process repeats until a quasiparticle obtains enough energy to escape to the unoccupied quasiparticle branch in the superconducting electrode, giving rise to an additional conduction channel. A relation between the voltage value V_n , at which an increase of conductance occurs due to MAR, and the number of completed Andreev reflections n can be simply derived from this picture

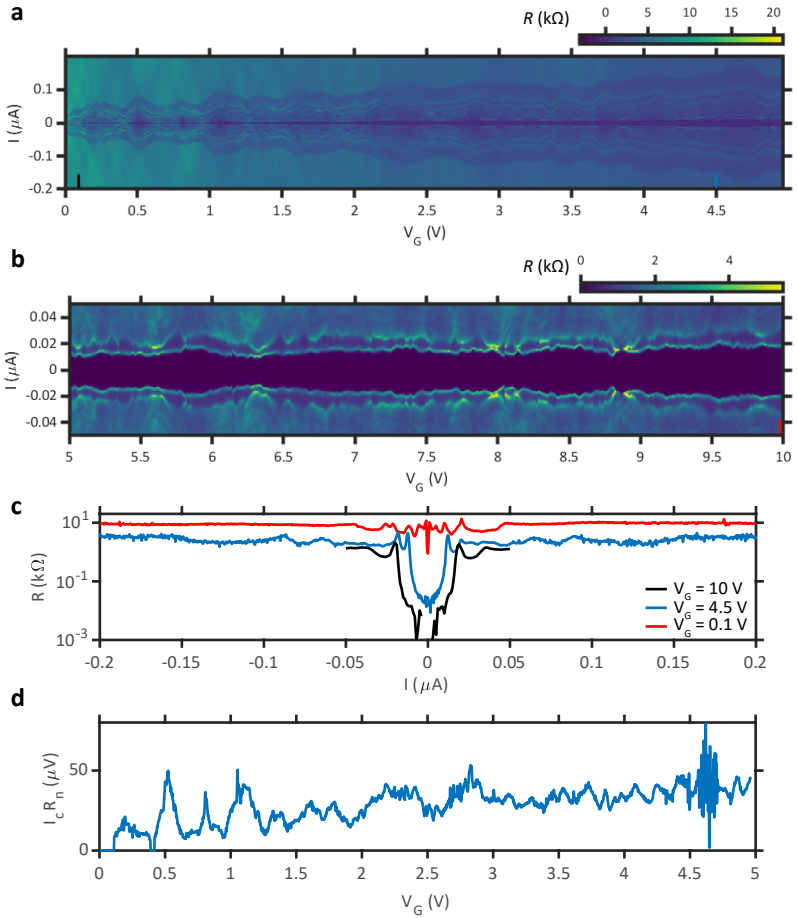


Figure 4.3. Josephson current in an InAs/Al NWJJ. a-b, Differential resistance R as a function of gate voltage V_G and bias current I . **c,** Vertical linecuts at gate voltage values marked in the map. **d,** The $I_c R_n$ -product as a function of V_G .

as $V_n = 2\Delta/en$ [82]. Using the formula from above, a superconducting gap $\Delta' = 134 \mu\text{eV}$ is estimated from the voltage difference between the two outermost conductance peaks in Fig. 4.4c, which is significantly lower than the bulk value. The voltage values, at which conductance peaks for the first five orders of MARs are expected, are indicated with grey lines. We can find conductance peaks that correspond up to the 5th-order MAR. In general, it is difficult to distinguish the order for high order MAR as the voltage difference between two adjacent peaks decreases for increasing order numbers. The observation of MARs indicate transparent interfaces which is beneficial for forming ABSs.

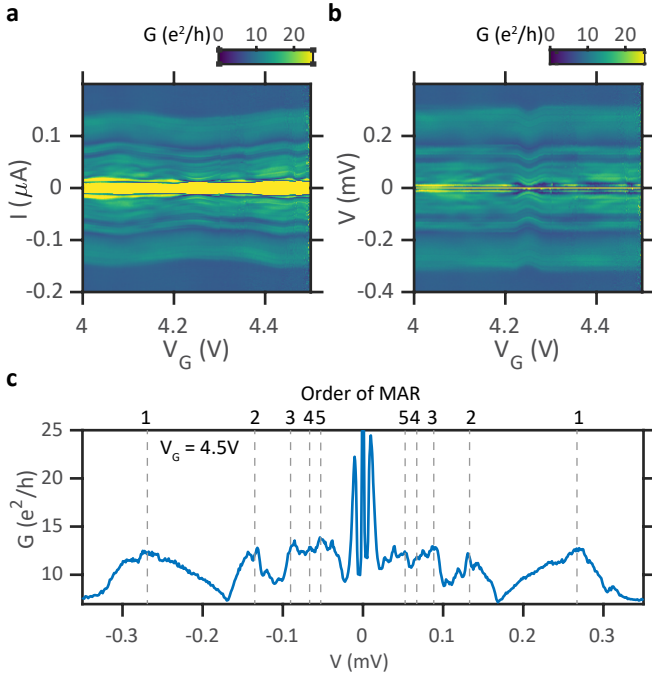


Figure 4.4. Multiple Andreev reflection. **a**, Computed differential conductance G as a function of bias current I and gate voltage V_G . **b**, Same data set as **a**. However, the current bias values are converted into voltage drop across the NWJJ using the method described in the main text. **c**, Vertical linecut from **b** at $V_G = 4.5 \text{ V}$. Voltage values with expected conductance enhancement are indicated with dashed grey lines and the order of MARs.

4.5. Transparency estimation

The study of the MAR features gives a qualitative understanding of the junction transparency. Now, we attempt to quantitatively understand the number of channels in the nanowire and their transparencies. The IV -curve of a few-mode transparent JJ can be decomposed into distributions of MARs [84–86]. In practice, we use a computer script to generate IV -curves using transparencies $\{\tau_1, \tau_2, \dots, \tau_n\}$ and the superconducting gap Δ as input parameters to mimic our experiment [87]. Fig. 4.5 shows the IV -curve at two representative gate voltage values. The lines are simulated using τ_i from Tab. 4.1 and $\Delta = \Delta' = 134 \mu\text{eV}$. The objective of the simulated IV -curves is to mimic the data up to $V = 0.3 \text{ mV} > 2\Delta/e$ as good as possible, so that the IV -characteristics are well described both in the superconducting and normal regimes.

We observe that three modes are enough to explain the data at low gate voltage, $V_G = 0.1 \text{ V}$, while the data at high gate voltage, $V_G = 4.5 \text{ V}$, require at least five channels. The increased number of ABSs can be explain by the higher carrier doping at larger gate voltage values. Overall, the transparencies are also higher at high carrier doping, perhaps due to more electric screening of impurities and lower potential fluctuations along the semiconducting part.

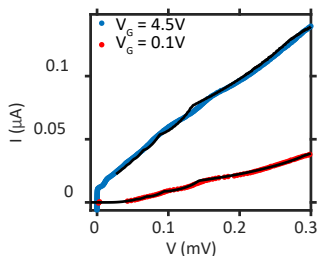


Figure 4.5. Transparency estimation. The IV -curves at two representative gate voltage values are plotted. The lines indicate simulated IV -curves using the transparency values in Tab. 4.1 that achieve the best correspondence with the experiment.

4.6. Conclusion

In summary, we have presented an electrical study of a full-shell epitaxial InAs/Al NWJJ in different carrier density regimes in the semiconductor, all

V_G (V)	τ_1	τ_2	τ_3	τ_4	τ_5
0.1	72.4	44.8	3.7	0	0
4.5	98.7	85.8	74.6	57.5	40.3

Table 4.1. Transparencies $\tau_1 \dots \tau_5$ in percentage used to reproduce the IV -curves in Fig. 4.5.

accessible via field-effect control. The device featured a tunable Josephson supercurrent in the investigated gate range. At high carrier doping, we estimated reasonably high transparencies for the numerous ABSs residing in the junction, verifying our etching recipe to form Andreev levels in the GHz range. In addition, the nanowire device was measured close to depletion, with quantum dot features forming in the junction area. The dataset is plotted and described in the App. C. In the next chapter, we will discuss the functionalities of our superconducting microwave circuitry.

5 Designing a superconducting cavity coupler for Andreev qubits

Superconducting resonators have been employed to inductively couple to Andreev bound states (ABSs), allowing coherent manipulation of Andreev pair transitions and even Andreev spins in the presence of spin-orbit interaction [24, 25, 27]. Now, our aim is to design a superconducting cavity coupler to entangle two spatially separated Andreev qubits using the inductive coupling scheme. Such a superconducting microwave cavity coupler should ideally possess of

- low photon energy decay rate to the environment and
- two current anti-nodes at distance.

In the Sec. 5.1, the coplanar transmission line coupler design from Majer *et al.* [6] is introduced together with our adaptation. The first generation coupler design was strongly susceptible to the environmental factors and could only show low internal quality factor. We later progressed to a capacitively coupled transmission line resonator pair geometry that reduces this susceptibility. The specifics are elaborated in Sec. 5.2. This chapter closes with the final design of the superconducting cavity coupler for Andreev qubits in the last section.

5.1. Half-wavelength transmission line resonator

The Fig. 5.1a illustrates the cavity coupler for two conventional superconducting qubits. It is a half-wavelength coplanar transmission line resonator which is opened at both ends such that two voltage anti-nodes develop. By placing the two superconducting qubits in the vicinity of the voltage anti-nodes, the charge degree of freedom of the qubits is coupled to the cavity voltage fluctuation and the qubits can exchange quantum information.

We adapted the half-wavelength coplanar transmission line resonator design and constructed the first generation cavity coupler for Andreev qubits in a similar fashion. Because the Andreev qubits couple inductively to the cavity, as discussed in the Sec. 3, the ends of the transmission line are shorted to the ground forming current anti-nodes. Fig. 5.1b displays the first generation coupler. The black arrows indicate the current amplitude maximum and thus

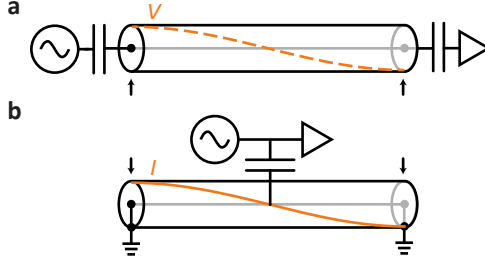


Figure 5.1. Half-wavelength transmission line resonator. **a**, Illustration of the cavity coupler for two spatially separated superconducting qubits. The resonator is measured in transmission. The voltage amplitude profile is plotted along the transmission line. **b**, First generation cavity coupler design for distant Andreev qubits. Here, the current amplitude profile is plotted along the transmission line. Arrows indicate the ideal location for the corresponding qubits in the two resonator types.

the ideal location of Andreev qubits for strong coupling to the cavity. The center of the cavity coupler is capacitively coupled to a feedline or directly to a readout circuit for reflection measurement.

It is common to test the resonator design prior the integration of nanowire devices. We hence fabricated a test chip using the layout as shown in Fig. 5.2a. The structures were patterned on NbTiN on an undoped Si wafer. The main part of the layout consists of a feedline, the cavity coupler and a quarter-wavelength test resonator in hanger configuration. The test chip was measured in a dilution refrigerator at base temperature. The qubit control lines (gate and flux lines) are grounded on a room temperature breakout box through several low-pass filter stages. Fig. 5.2b-c show the transmission spectrum $|S_{21}(f)|$ through the feedline. A prominent dip is measured at 6.35 GHz, which corresponds to the test resonator. The internal quality factor is deduced from fitting the resonance curve in the complex plane [60]. We obtain $Q_{i,\lambda/4} \approx 2.5 \cdot 10^5$ indicating low microwave loss to the environment. Surprisingly, the resonance of the cavity coupler is a shallow dip. A fit to the spectrum yields an internal quality factor of merely $Q_{i,\lambda/2} \approx 0.9 \cdot 10^3$.

The low quality factor and the large mismatch between $Q_{i,\lambda/2}$ and $Q_{i,\lambda/4}$ hint towards a flawed coupler design. We hence tested more chips with changes which we believe can help increasing the quality factor. It includes

- using a Si/SiO₂ wafer instead of a Si wafer,
- adding more bondwires on the ground plane,

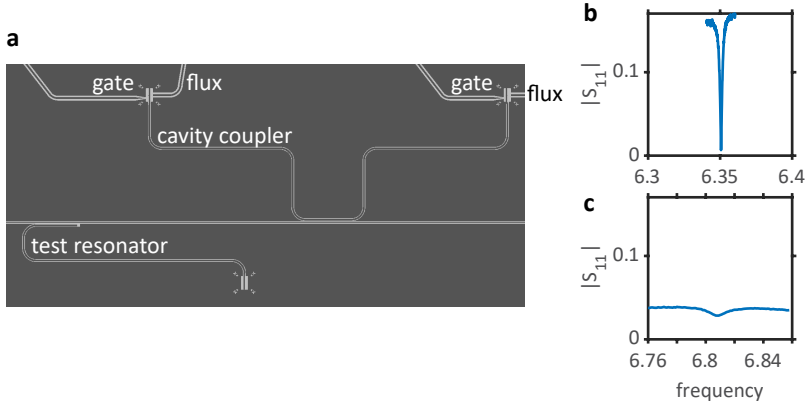


Figure 5.2. Cavity coupler test chip. **a**, The layout of the cavity coupler test chip. NbTiN is in grey. **b-c**, Transmission spectra through the feedline.

- removing the qubit control lines and
- more cautious cleaning of the chip.

At the end, we could experimentally exclude incautious handling of the chip, inhomogeneous superconductor or substrate, and microwave leakage through the qubit control lines as the reasons for the reduced internal quality factor. Furthermore, the reduced internal quality factor for the cavity coupler can not be reproduced using the Sonnet simulation software.

We suspect that shorting the center conductor on both ends to the ground opens a path for ground loop current to flow through the entire center conductor. It has been shown that a large supercurrent could weaken the pair correlation in a superconductor [88], which can be detrimental for the resonator's quality factor. Such a ground loop current could be prevented by breaking the center conductor. In the next section, we will see how the center conductor is broken and its implications.

5.2. Capacitively coupled quarter-wavelength transmission line resonator pair

In the second generation coupler design, the transmission line resonator is interrupted in the middle with the aim to prevent low frequency current on the center conductor. In the following, we discuss the resonance properties and design parameters in more detail. Fig. 5.3a shows the transmission line model of the so-called capacitively coupled transmission line resonator pair. It consists

of two transmission lines with exactly the same length $\sim L/2$ and a characteristic impedance Z_0 that are shorted to the ground on two ends and connected via a coupling capacitor C_m at $x = L/2$ in the middle. In the limit of a small capacitive coupling, this geometry yields two identical quarter-wavelength resonators with the same frequency. Because the coupling capacitance allows current to oscillate across the capacitor, this resonator design hybridizes two resonating modes with opposite symmetries. We can heuristically derive the current and respectively voltage amplitude profile of the resonating modes and their resonance frequencies. The readers are referred to App. B for details.

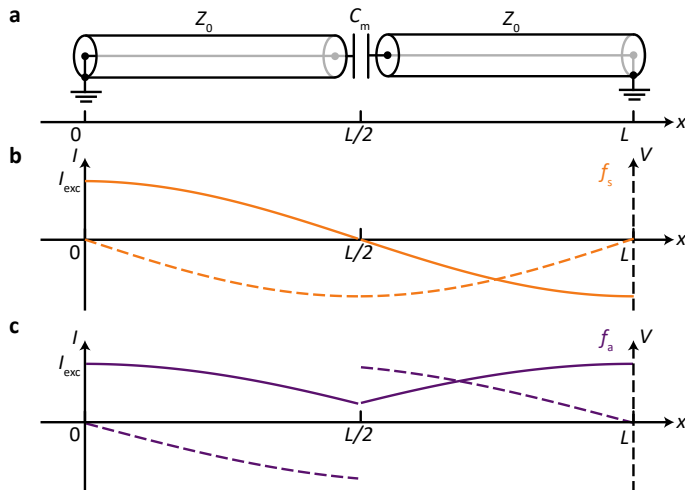


Figure 5.3. Capacitively coupled transmission line resonator pair. **a**, Transmission line model for the capacitively coupled resonator pair. A coupling capacitance is introduced to the center of the transmission line. **b-c**, Current and voltage amplitude profiles of the two resonating modes. Mode in **b** possesses an anti-symmetric current profile and a symmetric voltage profile at the coupling capacitance, whereas mode in **c** possesses a symmetric current profile and an anti-symmetric voltage profile.

Here, we solely plot the current and respectively voltage amplitude profile of the resonating modes (Fig. 5.3b-c). For the mode in **b**, the current is anti-symmetric at the coupling capacitor, while the voltage profile is symmetric. This mode is identical to the half-wavelength resonator without C_m , discussed in Sec. 5.1. For the mode in **c**, the current is symmetric at the coupling capacitance and its amplitude is non-zero across the capacitance. The voltage profile

is anti-symmetric and its amplitude across the capacitance is reduced in comparison to the first mode due to the finite current across the capacitor. The resonance frequency f_2 of the second resonating mode can be derived from that of the first mode f_1 under the assumption of a small variation $(f_1 - f_2)/f_1 \ll 1$. The formula reads

$$f_2 \approx f_1 \cdot \left(1 - \frac{4C_m Z_0}{\pi} f_1 \right). \quad (5.1)$$

For the rest of this chapter, the mode with symmetric voltage is referred to as the symmetric mode with resonance frequency f_s and that with anti-symmetric voltage is referred to as the anti-symmetric mode with resonance frequency f_a for brevity.

5.2.1. Resonator excitation

Microwaves can couple in different ways to a superconducting resonator. We decide to route microwave excitation through an open-ended coplanar transmission line to the middle of the capacitively coupled resonator pair, at the coupling capacitor, and measure the resonator response in reflection. The location of the voltage anti-nodes of the symmetric mode ensures a strong coupling to the resonator drive line. Moreover, the reflection measurement uses one port and thus captures all the reflected photons from the resonator that are not lost to the environment. This improves the signal-to-noise ratio in comparison to a transmission- or notch-type resonator measurement, where the resonator sees two ports. We name this design of the drive line the common port to emphasize the fact that it commonly excites both quarter-wavelength transmission lines resonators with the same phase. Technically, the common port can not excite the anti-symmetric mode which would require an excitation with a phase difference of π .

We use Sonnet to simulate the resonant behavior of the cavity coupler. The simulation file contains the design of the capacitively coupled coplanar transmission line resonator pairs with realistic material properties. Si is chosen as the substrate and a sheet inductance of 2.4 pH/ \square to mimic the kinetic inductance in the NbTiN film, which is calibrated from independent measurements using coplanar transmission line resonators of variable length. The reflection of the cavity coupler is simulated with two different excitation ports: a) a differential port with the signal being 180° out-of-phase on the two traces, b) a common port with a single trace. Fig. 5.4 shows the simulated reflection spectrum of the capacitively coupled resonator pairs. The figure contains a red curve that is simulated using a differential port and a blue curve that is simulated using a common port. The design of the ports is displayed in the insets close to the corresponding resonances. The port comes from left to right and ends before the center conductor of the resonator.

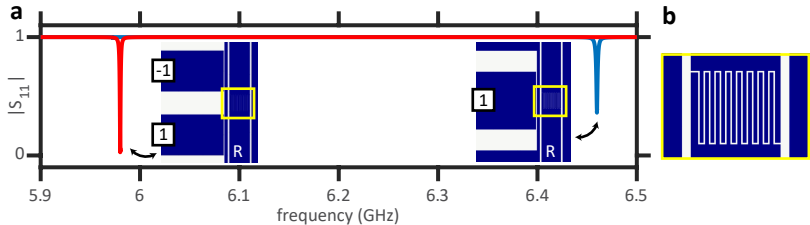


Figure 5.4. Simulation of the capacitively coupled resonator pair. **a**, The reflection amplitude $|S_{11}|$ is simulated against the excitation frequency. The red curve uses a differential port driving the anti-symmetric voltage mode, whereas the blue curve uses a common port driving the symmetric voltage mode of the same capacitively coupled resonator pair. The design of the drive lines are shown in the insets close to the corresponding resonances. The label R indicates the center conductor of the resonator. **b**, Illustration of the interdigitated coupling capacitor. The position of the capacitance is indicated with yellow boxes in the inset of **a**.

As expected from the transmission line model, the symmetry of the cavity drive reflects itself in the symmetry of the cavity. The anti-symmetric mode with a lower resonance frequency is excited when using the differential port while the symmetric mode with a higher resonance frequency is excited when using the common port. Thus, we are able to selectively establish a strong coupling to one of the two cavity modes, by adjusting the resonator drive line design.

The coupling rate from the drive line to the resonator's symmetric mode can be tuned by varying the distance between the resonator and drive line and the width of the drive line. Since we aim to engineer a coupled qubit-cavity system where the quantum decoherence is limited by the qubits, we design the photon energy decay rate to the drive line to be in the lower MHz-range, lower than the typical linewidth of Andreev pair transitions [24]. The coupling quality factor can be fitted from both the simulation and experiment. Usually, they differ by a factor of less than two.

5.2.2. Inter-resonator coupling capacitance

The next question arises: How should the inter-resonator coupling capacitance C_m be designed? In the previous section, it is shown that the resonance frequency f_a of the anti-symmetric voltage mode depends on the coupling capacitance. The frequency difference between the anti-symmetric and symmetric voltage mode increases for a larger coupling capacitance.

Since we are interested in measuring a clean qubit spectrum, we require the frequency difference of the two resonating modes to be five times greater than the qubit-resonator coupling strength, $\Delta f = f_s - f_a \gtrsim 5g$. Typical coupling strength of Andreev pair transitions with the resonator is found to be ~ 100 MHz [24, 36]. The lower bound for the coupling capacitance can be computed using Eq. (5.1). For $f_s = 6.5$ GHz, $Z_0 = 50 \Omega$, a design rule for the coupling capacitance is obtained that reads

$$C_m \gtrsim 186 \text{ fF}. \quad (5.2)$$

The frequency difference between the two resonating modes was simulated in Sonnet to confirm the analytically computed coupling capacitance. It was found through numerical simulation that the requirement of $\Delta f \gtrsim 5g$ is achieved with a smaller simulated capacitance. At the end, the interdigitated capacitance design in Fig. 5.4b is applied to the actual device. It consists of 8 finger pairs with a finger width of $2 \mu\text{m}$, an interdigital gap of $1 \mu\text{m}$ and a finger length of $40 \mu\text{m}$. It generates a simulated frequency difference of ~ 500 MHz between the modes, and a simulated capacitance of 43 fF at 6.5 GHz, which is about a factor of four different from the analytical value. To derive the expression Eq. (5.1), an assumption is made that is a small ratio of the frequency difference and the resonance frequency of the symmetric mode. In our case, the target $\Delta f/f_s \approx 0.08$ is quite substantial and could be the reason for the inaccurate prediction from the analytical expression.

5.2.3. Shared inductance

The coupling strength also imposes a design rule for the shared inductance between the resonator and the RF SQUID. For that, the resonator inductance and capacitance have to be found first. We require a 50Ω -resonator with a symmetric mode resonance frequency of 6.5 GHz. Using $Z_R = \sqrt{L_r/C_r}$ and $f_s = 1/2\pi\sqrt{L_r C_r}$, the resonator inductance and capacitance can be computed to be $L = 1.22$ nH, $C = 0.49$ pF.

We consider one ABS in the short-junction limit with a junction transparency τ and a superconducting gap Δ . For estimating the shared inductance, we consider the equation that relates the light-matter coupling strength to the zero-point flux fluctuation and the coupling current matrix element of the Andreev pair transition:

$$hg = \delta_{\text{zp}} |\langle 1 | H'_{\text{JJ}} | -1 \rangle|. \quad (5.3)$$

The coupling current matrix element $|\langle 1 | H'_{\text{JJ}} | -1 \rangle|$ in general depends on Δ , τ and the superconducting phase difference δ across the junction. Here, a conservative estimation is made by choosing $\Delta = 30$ GHz [25] such that $|\langle 1 | H'_{\text{JJ}} | -1 \rangle| \approx 0.3 \cdot 30$ GHz. Applying the condition $g = 100$ MHz hence

yields a zero-point flux fluctuation of $\delta_{zp} = 0.011$. Using Eq.(3.8), which relates the zero-point flux fluctuation to the shared inductance, we finally obtain a lower bound for the shared inductance l_s for a coupling strength greater than 100 MHz, that reads

$$l \gtrsim 86 \text{ pH}. \quad (5.4)$$

This is much smaller than the Josephson inductance of the NWJJ, which is typically on the order of nH. Thus, the phase drop across the shared inductance can be neglected.

5.3. Final design

The final layout of the superconducting cavity coupler for the experiment that links two Andreev qubits is shown in Fig. 5.5a. The entire capacitively coupled transmission line resonator pair extends over 6 mm, with a short to the ground at both ends. Small holes in the superconducting ground plane are left to trap flux vortices. Bondpads indicated with V_i are for the nanowire bottom gates. Because a qubit drive on the bottom gates is desired as well, the gate lines are designed to match 50Ω . I_i indicates the bondpads for DC current bias.

Fig. 5.5b presents the simulated current amplitude at resonance frequency in the nanowire area. Indeed, a current amplitude maximum occurs on the shared inductance. The SQUID loop is not closed for the simulation such that there is no current flow on the strip parallel to the shared inductance. Further considerations are discussed below.

Resonance frequency

We aim for a resonance frequency of $f_s = 6.5 \text{ GHz}$ to be in the intermediate regime to dispersively couple to both even and odd parity transitions. The Sonnet simulation reveals a symmetric mode resonance frequency of $f_s = 6.46 \text{ GHz}$.

Characteristic impedance of the transmission line

We see from Eq.(3.8) that the zero-point flux fluctuation across the NWJJ scales with the inverse of the square root of the resonator impedance $\delta_{zp} \propto 1/\sqrt{Z_r}$. We attempt to enhance the zero-point flux fluctuation by lowering the characteristic impedance of the transmission line. A center conductor with a width of $50 \mu\text{m}$ and a gap of $5 \mu\text{m}$ is used, yielding a simulated characteristic impedance of $Z_0 \approx 38 \Omega$. The characteristic impedance is related to the resonator impedance via

$$Z_R = \sqrt{\frac{L}{C}} = \frac{2}{\pi} Z_0 \approx 24 \Omega. \quad (5.5)$$

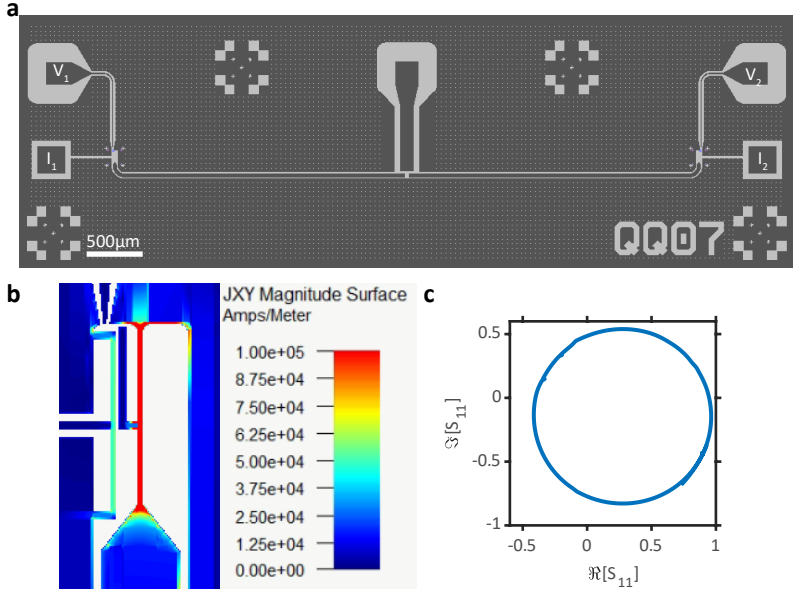


Figure 5.5. The cavity coupler for the experiment with two Andreev qubits. **a**, The cavity coupler layout. The lines indicated with V_i are for the nanowire bottom gates and the lines indicated with I_i are for passing a current next to the SQUID to phase bias. **b**, Simulated current amplitude in the qubit area at the resonance frequency. A maximum is found on the center conductor at the short end. **c**, Simulated reflection coefficient S_{11} of the capacitively coupled resonator pair.

Using the resonator impedance and the resonance frequency, we compute a simulated resonator inductance $L \approx 0.59$ nH and capacitance $C \approx 1.03$ pF.

Current bias line

Unlike existing experiments that apply a background magnetic field to flux bias single Andreev qubits, the two-qubit experiment requires independent flux biasing of two RF-SQUIDs. Our solution is to pass a current near each RF-SQUID. Through the study of simulation, we found that having single stripes with $50\ \Omega$ -resistive termination close to the cavity current anti-nodes induces substantial microwave leakage from the resonator. This problem is resolved by splitting the flux biasing stripes into two, as shown in the Fig. 5.5b. In this configuration, the resonator locally induces similar current in both flux biasing stripes such that no net current is induced on the stripe to the termination. This suppresses the transmission towards the current source by ~ 20 dB.

Shared inductance

We narrow down the center conductor at the short ends of the resonator to locally increase the inductance, as seen in Fig. 5.5b. With $\delta_{zp} \propto l_s$, the narrow stripe further increases the coupling to the Andreev transitions. Because of the symmetric design of the flux biasing stripes, only half of the narrowed center conductor is connected to the loop and contributes to the shared inductance. Assuming that the inductance is mainly given by the kinetic inductance, the share inductance is estimated to be $l \approx 0.12$ nH.

The zero-point flux fluctuation can be recalculated using simulated circuit parameters, $\delta_{zp} \approx 0.022$. This exceeds the value we impose earlier by a factor of two. Again, the factor of two comes from a larger l_s and a smaller Z_R than that which are derived from the design rules. Such a zero-point fluctuation would generate a coupling strength to the pair transitions of ~ 200 MHz, putting us in the strong coupling limit for the even parity Andreev states.

Coupling quality factor

A fit to the simulated reflection coefficient S_{11} in Fig. 5.5c yields a simulated $Q_c = 5300$.

5.4. Conclusion

We have developed two generations of half-wavelength superconducting cavity couplers and identified a problem of low internal quality factors when grounding a coplanar transmission line resonator on two sites. In the second generation, this problem is solved by introducing an interdigitated coupling capacitor

in the middle of the transmission line. We have discussed in-depth the design parameters by relating them to experimental conditions. The proposed cavity coupler design couples via cavity flux fluctuation to the qubits and hence is complementary to the cavity coupler in Ref. [6, 34], which are commonly used now for spin and superconducting qubits.

In the next chapter, we will integrate Andreev qubits into the cavity coupler and investigate the qubits using the coupler as qubit state detector.

6 Microwave spectroscopy of Andreev bound states in epitaxial InAs/Al nanowire Josephson junctions

In this chapter, we present the cavity coupler in operation with two Andreev pair qubits. For now, we do not intend to couple the Andreev qubits, such that only one qubit is measured at a time and the coupler is only used for qubit state readout. Sec. 6.1 shows the device consisting of the cavity coupler and two InAs/Al nanowire Josephson junctions (NWJJs). Sec. 6.2 discusses the qubit-field interaction, followed by the study of the pair transition linewidth in Sec. 6.3. After the investigation in the frequency domain, we demonstrate coherent manipulation of an Andreev pair qubit in both NWJJs in Sec. 6.4. Finally, we present the measurement of single quasiparticle transitions in a wider range of superconducting phase difference in Sec. 6.5.

6.1. Device

The device under investigation has two full-shell epitaxial InAs/Al NWJJs that are both inductively coupled to a superconducting cavity coupler. Fig. 6.1a shows a scanning electron micrograph of one of the two full-shell epitaxial InAs/Al NWJJs. Each qubit is controlled by a Ti/Pd bottom gate and a bias of the superconducting phase difference between the Al shells. The nanowire is suspended on NbTiN over the bottom gate. In the middle of the left (right) nanowire, an Al segment of 280 nm (190 nm) is stripped with wet-etching technique. Qubit control lines are shown in Fig. 6.1b. A DC current bias I_L next to the SQUID can tune the threading flux inside the loop and hence adjust the superconducting phase difference Φ_L across the NWJJ. The bottom gate is connected to a DC voltage source V_L and a microwave signal generator via an RC bias tee. Finally, Al contacts are evaporated on the Al-shell after the removal of surface AlO_x using Ar-milling, embedding the NWJJ in the NbTiN SQUID that is connected in parallel to the shared inductance (red) of the superconducting cavity coupler.

The superconducting microwave coupler is a NbTiN capacitively coupled coplanar transmission line resonator pair. A simplified schematic of the coupler and readout circuit is illustrated in Fig. 6.1d. The ends of the transmission line

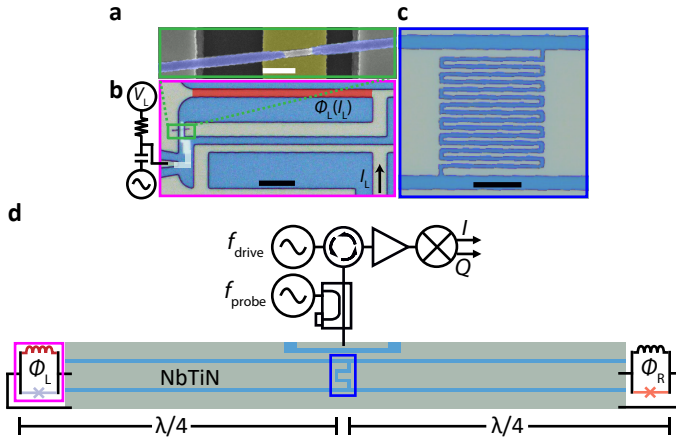


Figure 6.1. Microwave cavity coupler for distant Andreev pair qubits. **a**, False-colour scanning electron micrograph of the left full-shell InAs/Al NWJJ. The Al-shell (light blue) is etched to form a semiconducting NW-based JJ. The NWJJ is suspended on NbTiN (light grey) over a Ti/Pd bottom gate (yellow). The scale bar is 300 nm . **b**, Optical micrograph showing the left qubit. The NWJJ is contacted to a loop in the NbTiN layer forming an RF SQUID, which shares an inductance with the cavity (red in **b** and **c**). The Andreev qubit is controlled by a DC current bias I_L and a DC gate voltage V_L . Additional microwave signal on the gate allows excitation of the ABSs. The scale bar is $10\text{ }\mu\text{m}$. **c**, Optical micrograph of the resonator pair coupling capacitance. The scale bar is $20\text{ }\mu\text{m}$. **d**, Schematic of the device showing two distant gate- and flux-tunable NWJJs coupled to the short ends of a capacitively coupled $\lambda/4$ -coplanar transmission line resonator pair with the microwave readout setup (simplified).

are shorted to the ground forming two spatially separated current anti-nodes. Each half of the transmission line forms a quarter-wavelength mode and is capacitively coupled with each other via an interdigitated coupling capacitor in the center. Fig. 6.1c shows an optical micrograph of the coupling capacitor. Resonator probe and qubit excitation tones are routed through an open-ended transmission line to the coupling capacitor.

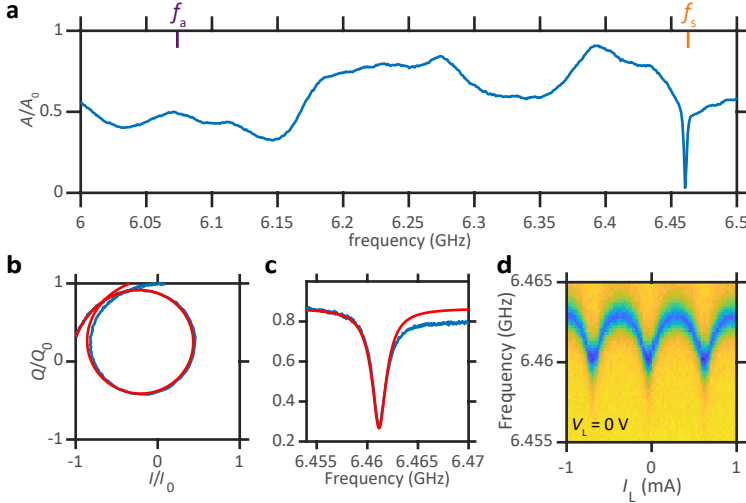


Figure 6.2. Symmetric mode resonance response. **a**, Normalized reflection coefficient A/A_0 as a function of probe frequency f_{probe} . A dip appears at the symmetric mode resonance frequency ~ 6.461 GHz. Measurement of the resonance in a smaller frequency span in normalized IQ -values (**b**) and normalized reflection coefficient (**c**). Red lines are fits to extract resonator parameters. **d**, Reflection coefficient measurement as a function of f_{probe} and the flux bias I_L .

A characterization of the cavity coupler is performed prior to the investigation of the NWJJs. For this, the NWJJs are pinched off at $V_{L,R} = -4$ V. As discussed in the Ch. 5, the cavity coupler possesses a strongly coupled symmetric mode with resonance frequency f_s and a weakly coupled anti-symmetric mode with f_a . Fig. 6.2a shows the normalized reflection amplitude A/A_0 as a function of frequency f_{probe} of a weak microwave probe tone. The observed resonance at ~ 6.461 GHz corresponds to the resonance of the symmetric mode. In fact, no resonance feature is observed at the frequency of the anti-symmetric mode, which is found by simulation to be at around

6 GHz, highlighting the weak coupling to the anti-symmetric mode from the cavity drive line. By fitting the resonance in the IQ -plane using the technique from Ref. [60], we extract the resonator parameters $f_s = 6.4612$ GHz, $\kappa_{\text{int}}/2\pi = 0.7$ MHz and $\kappa_s/2\pi = 1.2$ MHz, with κ_s being the coupling rate (Fig. 6.2b-c). Since $\kappa_s > \kappa_{\text{int}}$, the resonator is overcoupled to the readout circuit. The fitting process captures most of the line shape of the resonance, but does not work well for the right half of the spectrum. We suspect that it is caused by standing wave patterns on the sample holder or chip which gives a modulating reflection coefficient as background.

After the basic characterization of the cavity coupler, we determine the flux periodicity of the RF SQUIDS by monitoring the resonance shift as a function of current bias I_L , with the nanowire operating as a Josephson junction at $V_L = 0$ V. Fig. 6.2d shows the normalized reflection amplitude around f_s as a function of I_L . The periodic shift of the resonance frequency occurs due to a periodic change of the Josephson inductance. The periodicity of the left SQUID is determined from this measurement as $I_{2\pi}^{(L)} = 0.72$ mA. Similar measurement was performed on the right NWJJ to obtain the periodicity of the right SQUID $I_{2\pi}^{(R)} = 0.71$ mA. The discrepancy can result from a slightly different area of the SQUID loops due to the manual placement of NWs.

Furthermore, the π -points of each NWJJ can be identified from this measurement as the current bias point with the largest downwards resonance shift [24].

6.2. Qubit-resonator interaction

First, we search for Andreev pair transitions in each NWJJ individually, with the idling NWJJ being pinched off. The cavity coupler is probed with a weak microwave tone around symmetric mode f_s as a function of gate voltages at the π -points. The circulating photon number in the resonator is estimated to be ~ 1.54 , when applying an excitation power of 10^{-17} W at the device. Fig. 6.3a shows a single tone spectrum as a function of the gate voltage V_L at $\phi_L = \pi$. We observe that the cavity resonance disperses when sweeping V_L . Fig. 6.3b shows a single tone spectrum as a function of the flux bias ϕ_L at $V_L = 0.756$ V, marked in the gate dependent map. Similar resonance frequency shift is also observed when sweeping V_R and ϕ_R , see Fig. 6.3c-d. The observation of avoided-crossings indicates a strong coupling of the cavity coupler to Andreev pair transitions in both NWJJs. The transition frequency of a pair of ABSs depends on the junction transparency, which is tuned by the electric field-effect.

Fig. 6.3b and d are different because of the difference in junction transparency. The pair transition always remains above f_s in the former measurement and it is tuned below f_s when approaching $\phi_R = \pi$ in the latter

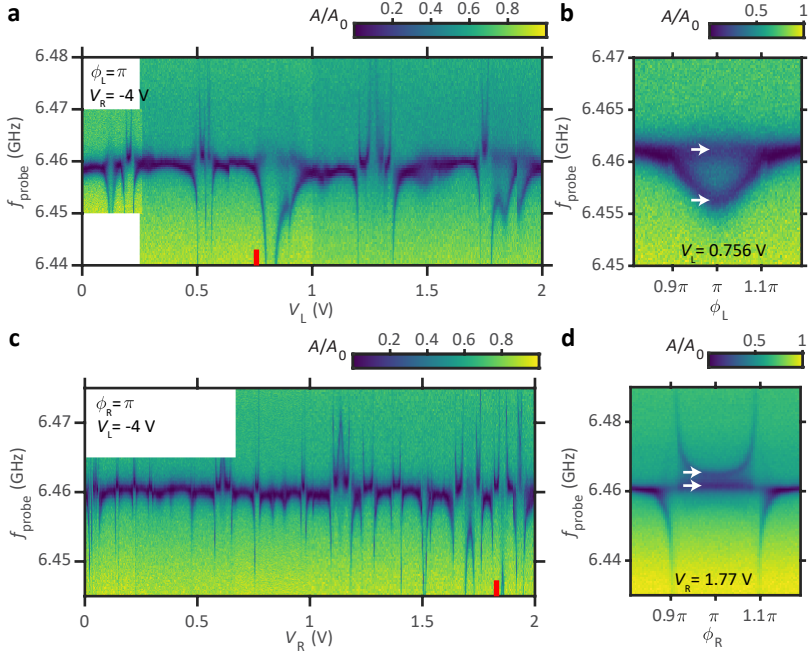


Figure 6.3. Hybridization of the Andreev pair transitions and symmetric cavity mode. Normalized reflection coefficient A/A_0 as a function of gates (**a**, **c**) and flux bias (**b**, **d**). Avoided-crossings are observed due to the inductive coupling of an Andreev pair transition and the symmetric cavity mode. White arrows indicate double dips featuring quasiparticle poisoning in the junctions.

measurement. Lower pair transition frequency at $\phi = \pi$ can be achieved with a higher junction transparency or in a finite-length junction. Furthermore, a double dip pattern is observed sometimes, e.g. in Fig. 6.3.b and d, indicating parity switching events in both NWJJs [24]. In both plots, the second resonance seems to be constant at f_s , suggesting that no single particle transition is coupled to the cavity in the measured flux range.

6.3. Qubit linewidth

After the demonstration of strong coupling of Andreev pair transitions to the symmetric cavity mode, the qubit spectral lines are measured by means of pulsed two-tone spectroscopy. We focus on one Andreev pair transition in the right qubit. Fig. 6.4a-b shows the single tone spectrum as a function of V_R and ϕ_R . Again, a pull of the resonance frequency is observed due to a dispersively coupled Andreev pair transition. In the pulsed two-tone spectroscopy measurement, a saturating qubit drive pulse with variable frequency f_{drive} is sent to the device at the same time as a weak resonator probe pulses with frequency $f_{\text{probe}} \approx f_s$. Afterwards, both pulses are turned off for $8 \mu\text{s}$ such that the qubit can relax to the ground state. A second probe pulse is then sent to probe the resonator when the qubit is in the ground state. Fig. 6.4c-d show the normalized change I/I_0 of the quadrature values between the two reflected resonator probe pulses as a function of V_R and ϕ_R . The measured resonances are the transition frequency f_{qb} of the Andreev pair qubit.

We extract the qubit-cavity detuning $\Delta_f = f_{\text{qb}} - f_s$ from the two-tone spectrum and the dispersive shift χ from the single-tone spectrum at the operation point where the qubit is insensitive to gate and flux noise to the leading order. Using $\chi/2\pi = -(g/2\pi)^2/\Delta_f$, the coupling strength between the Andreev pair qubit and symmetric cavity mode is found to be $g/2\pi = 119 \text{ MHz}$ at this operation point. The qubit-cavity coupling strength is not a constant value, but depends on the coupling matrix element of the transition and the presence of additional Andreev transitions in the microwave range [67]. Both physical quantities have strong gate and flux dependence.

Interestingly, the qubit linewidth becomes wider when tuned away from the π -point in the flux space. Such a behaviour is not observed in the gate space. This observation suggests a flux-noise limited coherence time for the Andreev pair qubit at $\phi_R \neq \pi$. To quantify the effect of the control parameters V_R and ϕ_R on decoherence, the measured qubit spectrum is fitted with a Lorentzian function and the slope of the qubit frequency dispersion is computed numerically as $\frac{f_{\text{qb}}(x_{i+1}) - f_{\text{qb}}(x_i)}{x_{i+1} - x_i}$, with $x \in \{V_R, \phi_R\}$ being the control parameters. Fig. 6.4e shows two exemplary spectra and fits at $\phi_R = \pi$ (blue) and $\phi_R = 1.09\pi$ (black).

The extracted full width at half maximum FWHM and slope are plotted as a

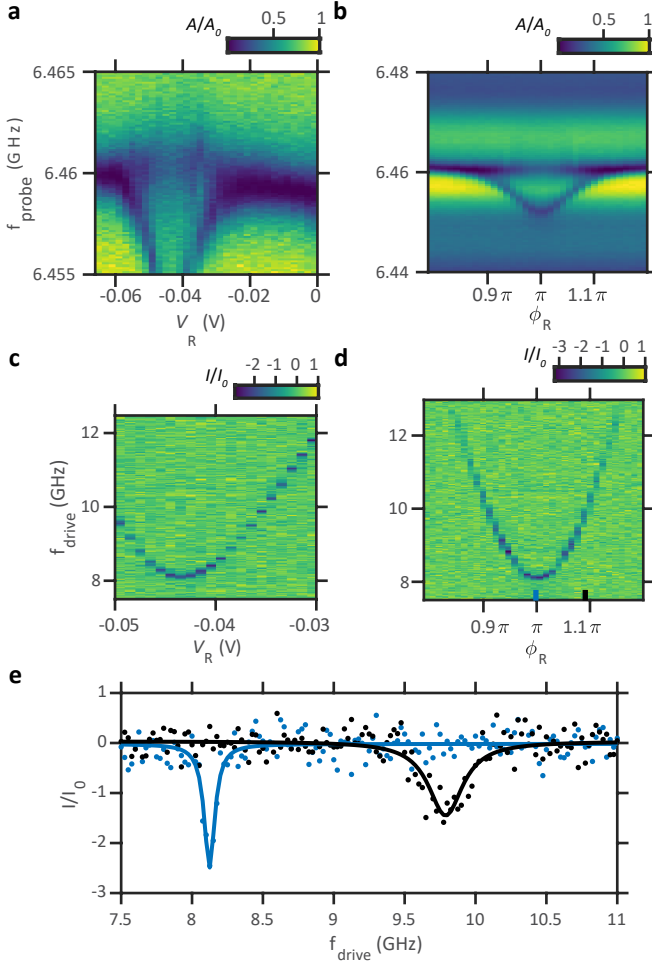


Figure 6.4. Gate and flux tunable Andreev pair transition. **a-b**, Single tone spectrum around f_s as a function of gate V_R and flux ϕ_R . **c-d**, Normalized change of the quadrature value of the resonator probe pulse (I/I_0) as a function of V_R and ϕ_R . **e**, vertical linecuts from **d**. The solid lines are Lorentzian fits to the data.

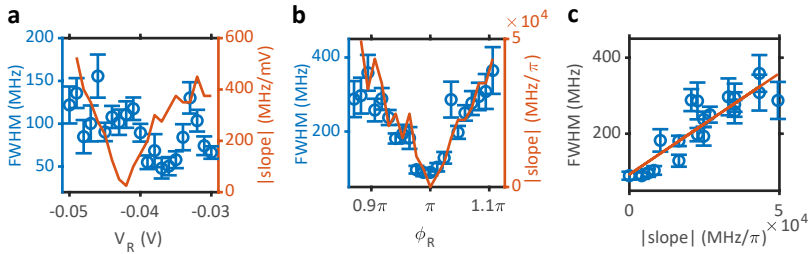


Figure 6.5. Gate and flux noise. The extracted qubit linewidth FWHM and numerically computed slope of the dispersion relations plotted as a function of V_R (a) and ϕ_R (b). c, FWHM as a function of the slope in the flux space. The solid line is a linear fit.

function of the control parameters in Fig. 6.5a-b. It becomes apparent that the qubit linewidth and slope in the gate space are uncorrelated, while that in the flux space indeed increases with the slope. In Fig. 6.5c, the extracted FWHM is plotted against the slope in the flux dispersion to emphasize their correlation. Using a phenomenological linear model: $\Delta f_{\text{qb}} = \partial f_{\text{qb}}/\partial \phi_R \cdot \sigma_\phi + \Delta f_{\text{qb},\pi}$, we can estimate the flux fluctuation σ_ϕ and the qubit linewidth at the flux sweet-spot $\Delta f_{\text{qb},\pi}$. The fit to the data in Figure 6.5c yields a $\sigma_\phi = 0.0053\pi$ and $\Delta f_{\text{qb},\pi} = 93$ MHz. The value of $\Delta f_{\text{qb},\pi}$ value at the flux sweet spot suggests a maximum coherence time of $T_2 = 1.3/\pi \Delta f_{\text{qb},\pi} \approx 4$ ns [89].

In the next section, we will operate the NWJJs as Andreev pair qubits and demonstrate coherent manipulation of the pair transitions.

6.4. Coherent manipulation of pair transitions

First, we investigate the left Andreev pair qubit. Fig. 6.6a presents two-tone spectroscopy with the qubit spectrum as a function of V_L at $\phi_L = \pi$. At the gate sweet-spot $V_L = 1.8$ V, we apply a coherent qubit drive pulse of variable pulse width t_{rabi} to address the qubit transition. The response of the cavity is measured twice, immediately after the manipulation period and after the qubit decays to the ground state, each time with a $1\mu\text{s}$ -long probe pulse. The qubit state vector rotates between the excited and ground state under the influence of the coherent drive pulse, yielding oscillations, also known as Rabi oscillations, in the cavity response. The normalized change of the quadrature value Q/Q_0 between the two cavity readout pulses is plotted as a function of t_{rabi} and drive power in Fig. 6.6b. As the drive power increases, the oscillation becomes faster showing up to 10 full periods within 50 ns. A finite decoherence time leads to a reduction in the contrast over time. We

note that the measured Q/Q_0 does not oscillate symmetrically about a mean value, but tends to saturate at a value that is higher than the mean value at large t_{rabi} , which we do not fully understand. This behaviour is more apparent in the Fig. 6.6c, showing a linecut from Fig. 6.6b at -5dBm. We use a fit function: $A \exp(-t_{\text{rabi}}/T_{2,\text{rabi}}) \sin(2\pi f_{\text{rabi}} t_{\text{rabi}} + \phi) + B t_{\text{rabi}} + C$ to fit the Rabi oscillation, where the term $B t_{\text{rabi}}$ accounts for this tendency. The decay of Rabi oscillation is estimated to be $T_{2,\text{rabi}}^{(\text{L})} = 19$ ns. Furthermore, a T_1 measurement is performed by preparing the qubit in the excited state and letting it decay over the time t_{wait} before readout. An exponential fit to the data shows an energy relaxation time of $T_1^{(\text{L})} = 1.07 \mu\text{s}$.

Similar studies can be conducted at other gate voltages and on the right qubit. Here, Fig 6.6e-g show the study of an Andreev pair transition in the right qubit at the gate sweet-spot $V_{\text{R}} = 1.457$ V and $\phi_{\text{R}} = \pi$. We obtain a qubit frequency of $f_{\text{qb,R}} = 5.6$ GHz, $T_{2,\text{rabi}}^{(\text{R})} = 58$ ns and $T_1^{(\text{R})} = 0.28 \mu\text{s}$.

Because the right qubit frequency is closer to the symmetric mode resonance frequency f_{s} , the shorter energy relaxation time ($T_1^{(\text{R})} < T_1^{(\text{L})}$) could be caused by spontaneous emission into the environment via the resonator, described by the Purcell-effect [90, 91]. The Purcell-limited energy relaxation time $T_1^{\text{Purcell}} = \frac{2\pi}{(g/\Delta_f)^2 \kappa}$ becomes longer with larger qubit-resonator detuning Δ_f . For the right qubit, the Purcell-limited energy relaxation time is estimated to be $T_1^{\text{Purcell}} \approx 16 \mu\text{s}$ which can not explain the measured short $T_1^{(\text{R})}$. Because $T_1^{(\text{R})}$ corresponds to a frequency uncertainty that is larger than the measured qubit linewidth from the previous section, we learn that the linewidth in the two-tone spectroscopy is limited by qubit dephasing.

The reasons for the short energy relaxation and decoherence time remain unclear. But the facts that both nanowires are fabricated and measured nominally in the same way on the same chip and a difference of almost a factor of three is seen in the T_2^{rabi} suggests that there is a large variation in the NW device parameters.

6.5. Spin-orbit splitting of ABSs

In addition to the characterization of the pair transitions, single quasiparticle transitions (SQPTs) were also measured using the cavity coupler. The transition frequency of the SQPTs are often lower around $\phi = 0$ than $\phi = \pi$ [56]. Hence, two-tone spectroscopy was performed beyond the narrow range around $\phi = \pi$. A typical half-range two-tone spectrum is shown in Fig. 6.7. The spectrum is taken at $V_{\text{R}} = 0.884$ V. At this gate voltage value, there is no evident pair transition below 20 GHz. However, multiple resonances are observed around $\phi_{\text{R}} = 0$. In particular, the four resonances indicated with arrows seem to merge at $\phi_{\text{R}} = 0$ and to split for $\phi_{\text{R}} \neq 0$ or $\phi_{\text{R}} \neq \pi$. These resonances are associated with four SQPTs between four Andreev spin states

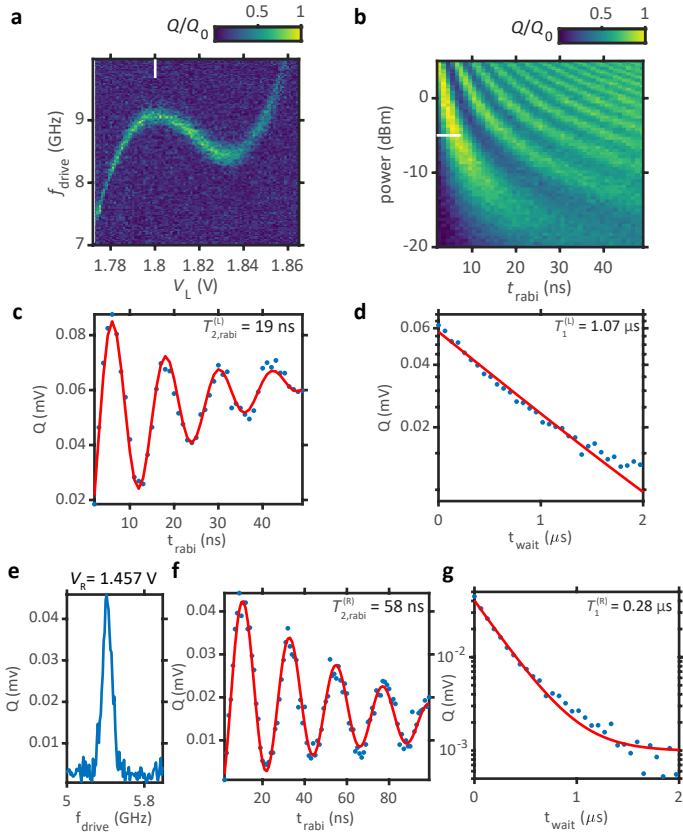


Figure 6.6. Time domain measurement of Andreev pair transitions. **a**, Two-tone spectroscopy, demonstrating the qubit spectrum as a function of V_L at $\phi_L = \pi$. **b**, Normalized change of the quadrature value Q/Q_0 between the two cavity readout pulses as a function of drive pulse width t_{rabi} and drive power. **c**, Rabi oscillation as a function of t_{rabi} at -5 dBm. The solid line is a fit function according to the text. **d**, $T_1^{(L)}$ measurement. The line is an exponential fit to the data. Similar measurements for the right qubit are plotted in **e** (Qubit spectrum), **c** (Rabi oscillation at -5 dBm), and **g** ($T_1^{(R)}$ measurement).

that are split due to strong spin-orbit coupling in the InAs nanowire. The dispersion of these transitions depends on mesoscopic parameters such as the junction length, junction transparencies, charging energy in the normal region and the SOI strength, as analysed in [55, 56]. With the wide gate and flux tunability of the InAs/Al NWJJ, a zoo of different SQPT configurations can be accessed. Since the SQPTs are not subject of this thesis, we move additional measurement that demonstrates the local gate dependence of some of the SQPTs in one device in App. D.

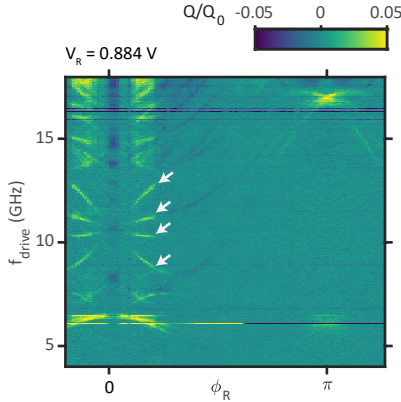


Figure 6.7. Spin-orbit splitting of single quasiparticle transitions. Normalized change of the quadrature value of the resonator probe pulse Q/Q_0 as a function of ϕ_R and f_{drive} , measured at $V_R = 0.884 \text{ V}$. Resonances indicated with white arrows correspond to single quasiparticle transitions.

6.6. Conclusion

We have fabricated a device with two full-shell epitaxial InAs/Al NWJJs, which were inductively coupled to a superconducting cavity coupler. We have demonstrated that both NWJJs were strongly coupled to the symmetric mode of the cavity coupler, supported by the measurement of avoided-crossings between Andreev pair transitions and the cavity mode. We were able to operate the same cavity mode as a spectroscopy tool to obtain both pair transitions and SQPTs in the Andreev spectrum, from both NW devices. In another experiment, we have demonstrated that the cavity coupler could be used as a qubit state detector, when the NWJJs operated as Andreev pair qubits. the dynamic characteristics of both Andreev pair qubits were measured.

In the next chapter, we want to demonstrate qubit-qubit coupling via the harmonic modes of the superconducting microwave coupler.

7 Photon-mediated long-range coupling of two Andreev pair qubits

In the previous chapter, we have shown that the Andreev pair qubits can interact with the symmetric mode of the cavity coupler. This chapter is dedicated to the demonstration of long-range coupling of two Andreev pair qubits via the microwave cavity coupler. Parts of this chapter were submitted for publishing.

Photon-mediated long-range coupling of two Andreev pair qubits

L. Y. Cheung,¹ R. Haller,¹ A. Kononov,¹ C. Ciaccia,¹ J. H. Ungerer,^{1,2}
T. Kanne,³ J. Nygård,³ P. Winkel,^{4,5,6} T. Reisinger,⁴ I. M. Pop,⁴
A. Baumgartner^{1,2} and C. Schönenberger^{1,2}

¹Department of Physics, University of Basel, Klingelbergstrasse 82, CH-4056, Switzerland

²Swiss Nanoscience Institute, University of Basel, Klingelbergstrasse 82, CH-4056, Switzerland

³Center for Quantum Devices, Niels Bohr Institute, University of Copenhagen, DNK-2100, Denmark

⁴IQMT, Karlsruhe Institute of Technology, DE-76344, Germany

⁵Departments of Applied Physics and Physics, Yale University, Connecticut 06511, USA

⁶Yale Quantum Institute, Yale University, Connecticut 06520, USA

7.1. Abstract

In a superconducting weak link, the supercurrent is carried by Andreev bound states (ABSs) formed by the phase-coherent reflection of electrons and their time-reversed partners. A single, highly transmissive ABS can serve as an ideal, compact two-level system, due to a potentially large energy difference to the next ABS [28]. While the coherent manipulation of such Andreev pair qubits (APQs) has been demonstrated [24, 25], a long-range coupling between two APQs, necessary for advanced qubit architectures [92, 93], has not been achieved, yet. Here, we demonstrate a coherent remote coupling between two APQs, mediated by a microwave photon in a novel superconducting microwave cavity coupler. The latter hosts two modes with different coupling rates to an external port. This allows us to perform fast readout of each qubit using the strongly coupled mode, while the weakly coupled mode is utilized to mediate the coupling between the qubits. When both qubits are tuned into resonance with the latter mode, we find excitation spectra with avoided-crossings, in very good agreement with the Tavis-Cummings model [94]. Based on this model, we identify highly entangled two-qubit states for which the entanglement is mediated over a distance of six millimeters. This work establishes APQs as compact and scalable solid-state qubits.

7.2. Main

The fundamental quantum states in superconducting weak links are Andreev bound states (ABSs) that form as superpositions of propagating electrons and holes near a superconductor [22, 95, 96]. In Fig. 7.1a), we illustrate the formation of a single, highly transmissive ABS in a short normal metal or semiconductor region (N) between two superconducting reservoirs (S) with a superconducting gap Δ . The condition for constructive interference of the electron and

hole partial waves contains phase shifts due to Andreev reflections at the NS interfaces and the propagation in N [40, 97, 98]. For a single channel in the short junction limit, the constructive interference results in two time-reversed, spin-degenerate Andreev levels, with eigenenergies tuned by the phase difference δ between the two superconducting order parameters. Including a transmission probability τ in the N part between the two superconductors, one obtains the energy spectrum $E_{\pm}(\delta) = \pm\Delta\sqrt{1 - \tau\sin^2(\delta/2)}$ around the Fermi energy, as shown in Fig. 7.1b) [28, 39, 99, 100]. We choose these two states at constant $\delta = \pi$ to define the Andreev pair qubit (APQ) with a tunable excitation gap of $\Delta E = 2\Delta\sqrt{1 - \tau}$. The APQ subspace is spanned by the even parity ground state of the weak link and an excited state with two quasiparticle excitations. The corresponding qubit transition frequency is then given by $f_{\text{qb}} = \Delta E/h$, with the Planck constant h . Since the next ABSs are typically found at much larger energies near Δ , the next excited state can in principle be engineered with a much greater energy difference than the qubit transition. This unique gate-tunable energy spectrum stands in strong contrast to other, more established superconducting qubits, e.g., transmon qubits [101], in which dynamical driving of the qubits is severely limited by the leakage out of the computational subspace into higher excited states [102, 103].

To implement a general quantum algorithm, it is necessary to couple two qubits coherently. While the coupling between two ABSs over short distances is being explored in various systems [96, 104–106], a long-distance coupling could not be established so far. On the other hand, the versatile long-distance coupling and quantum state readout have been established for other qubit platforms, for example superconducting [92] or semiconductor qubits [93, 107], using superconducting microwave resonators. The reproducibility and low losses of superconducting microwave resonators, and the potentially strong coupling to the APQs make these techniques ideal to transfer quantum information between APQs [108].

Despite significant progress in understanding coupled ABS-resonator systems using circuit quantum electrodynamics, only experiments with single APQs have been performed so far [24, 25, 27, 29, 29, 31, 35, 55, 56, 108–110]. Here, we first demonstrate a strong coupling of two individual APQs to the same superconducting resonator mode, with qubit decay rates lower than the coupling strengths to the resonator mode. In a second step, we simultaneously bring the APQ transition energies into resonance with a specific resonator mode that only couples weakly to the measurement circuit. A coherent, exchange-type coupling between the two APQs is then established, with the mutual coupling mediated by a microwave photon, and not disturbed by the out-coupling. The resulting excitation spectrum is fully captured by the Tavis-Cummings model, solely using independently determined single qubit parameters [94]. This allows us to identify highly entangled two-qubit states,

possibly allowing the implementation of future remote two-qubit gate operations for Andreev qubits.

The investigated quantum circuit is illustrated schematically in Fig. 7.1c-d) and consists of two InAs nanowire weak links, each with a single, highly transparent ABS forming the APQ. The nanowires have an epitaxially grown Al shell [43], etched away in a short semiconducting region to form the left APQ (L-APQ) and the right APQ (R-APQ). Local bottom gates are used to separately control the qubit frequency of each APQ. A scanning electron micrograph of the R-APQ is shown in Fig. 7.1e). This nanowire weak link is embedded in a superconducting pick-up loop forming an rf-SQUID [80], as shown in Fig. 7.1f). The threading magnetic fluxes $\Phi_{L,R} = \Phi_0 \delta_{L,R} / 2\pi$, controlled by an external current line, is used to set the corresponding phase differences $\delta_{L,R}$, with $\Phi_0 = h/2e$ the superconducting flux quantum [108]. The cavity coupler is composed of two nominally identical quarter-wavelength resonators (Fig. 7.1g). One of the key elements in our design is a coupling capacitor designed between the two resonators at the respective voltage antinodes. The coupling capacitor prohibits low frequency dissipative current flowing through the center conductor and thus ensures low internal loss of the cavity coupler. This design combines the two quarter-wavelength modes of the individual coplanar transmission line resonators into two half-wavelength modes, one mode with a symmetric voltage profile along the transmission line with a resonance frequency of $f_s = 6.461$ GHz (Fig. 7.1c) and the other mode with an anti-symmetric voltage profile with a resonance frequency of $f_a = 6.075$ GHz (Fig. 7.1d). The readout port, designed as an open-ended coplanar transmission line to the center of the cavity coupler, can be used to apply a symmetric voltage excitation to the cavity coupler and thus couples strongly to the symmetric coupler mode with a coupling strength $\kappa_s/2\pi = 1.2$ MHz. In contrast, the excitation of the anti-symmetric coupler mode through the readout port is suppressed due to the mismatch of the symmetries between the voltage excitation and coupler mode. The pick-up loops are galvanically connected to the central conductor of the respective resonator current antinodes (Fig. 7.1f).

We first demonstrate a strong coupling between each APQ and the anti-symmetric coupler mode. Owing to a weak coupling to the readout port, the anti-symmetric coupler mode has a long lifetime and can strongly hybridise with an APQ at small detunings ($f_{qb} \approx f_a$). We probe the excitation spectra of the qubit-coupler hybrid system using pulsed two-tone spectroscopy techniques. The transition from the ground state of the qubit-coupler system to an excited state can be addressed by an excitation pulse with variable microwave frequencies f_{drive} . The population of such a hybrid excited state shifts the resonance frequency of the symmetric coupler mode, measured in the reflection coefficient of a microwave probe pulse at a frequency near f_s , routed through a Josephson parametric amplifier operating close to the quan-

tum limit [111]. The APQ-coupler coupling strength for the symmetric coupler mode $g_{s,L/R}/(2\pi)$ is measured to be ~ 120 MHz (not shown). In our experiment, both the qubit excitation and resonator probe pulses are routed through the readout port to the qubit-coupler system. The resonator probe pulse is applied twice, once during the qubit excitation and the other time after the system relaxes back to the ground state (Details in the Methods). The differential quadrature ΔQ is obtained by subtracting the two reflected probe pulses to reject slow drifts.

To investigate a single APQ-coupler system, we tune the respective phase of the investigated APQ to the sweet-spot, $\delta_i = \pi$, where the qubit frequency is insensitive to small phase fluctuations. The other, idling APQ is phase biased such that its transition frequency is far above f_a . Fig. 7.2a) shows the differential quadrature ΔQ as a function of f_{drive} and V_L . We find an avoided crossing between the qubit and cavity resonances, demonstrating a coherent coupling between the L-APQ and the anti-symmetric coupler mode [49]. A fit of ΔQ with two Lorentzians and a linear background on resonance, $f_a = f_{\text{qb,L}}$, results in a qubit-coupler coupling rate of $g_{a,L}/(2\pi) = 141$ MHz, which exceeds the qubit decay rate $\gamma_L/(2\pi) = 77$ MHz. We find a similarly strong qubit-resonator coupling for the R-APQ, with $g_{a,R}/(2\pi) = 104$ MHz and $\gamma_R/(2\pi) = 82$ MHz (Fig. 7.2b).

In Fig. 7.2b), we find a weak, gate-independent resonance at a frequency $f_a = 6.075$ GHz between the APQ-coupler hybrid states. We attribute this line to the excitation of the bare anti-symmetric coupler mode without a coupled APQ. In the short junction limit, there are two degenerate current-less odd parity states, that are insensitive to the resonator current and thus do not couple to the resonator [25]. Parity switching with a rate faster than the measurement time can thus result in a reflected signal by exciting the bare anti-symmetric resonator mode.

When a bare qubit state is degenerate with the cavity excitation, they form a new set of eigenstates due to the exchange of excitations between them. This new set of qubit-coupler hybrid states is best seen as an avoided crossing in the spectrum described by the Jaynes-Cummings Hamiltonian [24, 55, 56, 69, 108]. The measured spectra are very well reproduced by the latter for one resonator mode coupled to a qubit $H_{\text{JC}} = \hbar g_{a,i}(a\sigma_{+,i} + a^\dagger\sigma_{-,i})$, with σ_+ (σ_-) and a^\dagger (a) being the qubit and resonator raising (lowering) operators. It describes the coherent exchange of one excitation between a qubit i and the cavity mode at a rate of $g_{a,i}$. In Fig. 7.2c), we plot the corresponding calculated spectrum for the R-APQ as a function of V_R using the extracted $g_{a,R}$ (See Methods for Details). The voltage axis is calibrated by equating the lowest and highest resonance frequencies with the corresponding qubit frequencies. The two resonances corresponding to the qubit-coupler hybrid states $|\pm_R\rangle$ are colored according to the qubit weight $|\langle 0, e_R | \pm_R \rangle|^2$. As the R-APQ qubit frequency is tuned across f_a by V_R , the eigenstate $|\pm_R\rangle$ evolves gradually from

a bare photonic state $|1, g_R\rangle$ to a bare qubit excited state $|0, e_R\rangle$, while $|-\rangle$ evolves from $|0, e_R\rangle$ to $|1, g_R\rangle$. At the degeneracy point at $V_R = 2.5225$ V, the coherent exchange of one excitation forms the two maximally hybridized states $|\pm\rangle = 1/\sqrt{2}(|1, g_R\rangle \pm |0, e_R\rangle)$, with a vacuum Rabi splitting of $g_{a,R}/\pi$. The odd state $|1, o_R\rangle$ does not couple to the resonator, so that the resonance is purely given by the bare anti-symmetric mode frequency f_a .

The main result of our work is shown in Fig. 7.3). We investigate the circuit with both qubit frequencies tuned into resonance with the anti-symmetric coupler mode. First, the left APQ-coupler maximally hybridized states $|\pm_L\rangle$ is generated by setting $V_L = 1.810$ V and $\delta_L = \pi$. Then, we perform again pulsed two-tone spectroscopy while sweeping V_R , such that the qubit frequency $f_{qb,R}$ of the R-APQ crosses f_a . The differential quadrature ΔQ between the two probe pulses is plotted as a function of V_R and f_{drive} in Fig. 7.3a). The measurement exhibits a spectrum showing that a resonance evolves from $|-\rangle$ for $f_{qb,R} \ll f_a$ to $|+\rangle$ for $f_{qb,R} \gg f_a$. As the single qubit frequency $f_{qb,R}$ is tuned into resonance with $|-\rangle$, the R-APQ hybridises with the left-site coupled system, forming an avoided crossing between the resonances of $|-\rangle$ and the R-APQ excited state. Likewise, a second avoided crossing emerges when $f_{qb,R}$ crosses with the transition frequency to $|+\rangle$, giving rise to the sigmoid-like dispersion [93, 107, 112]. This resonance is characteristic for the two-qubit hybrid state $|D\rangle$ with an anti-symmetric superposition of the two qubit states and demonstrates a strong coupling between the two APQs over a macroscopic distance.

To identify the eigenstates of the complete circuit, we calculate the excitation spectrum as a function of V_R using the Tavis-Cummings model $H_{TC} = \sum_i^N \hbar g_{a,i} (a\sigma_{+,i} + a^\dagger\sigma_{-,i})$ [94]. It describes the interaction between one resonator mode and $N > 1$ qubits. Inserting the qubit-coupler coupling rates extracted from single qubit measurements in Fig. 7.2), the resulting dispersion relation of the eigenstates reproduces the experimental data very well (Fig. 7.3b). The solid black line indicates the transition to the excited state $|D\rangle$. This model now allows us to identify the eigenstates, where the sigmoid-like resonance is a superposition of the two bare qubit excited states and the resonator state. When all three bare transition frequencies are resonant (black arrows), the coherent exchange between the qubits result in an eigenstate $|D_0\rangle$ devoid of the photonic excitation. This state explicitly reads

$$|D_0\rangle = \frac{1}{\sqrt{g_{c,L}^2 + g_{c,R}^2}} (g_{c,R}|0, e_L, g_R\rangle - g_{c,L}|0, g_L, e_R\rangle). \quad (7.1)$$

The dashed black lines are associated with transitions to the two two-qubit hybrid states $|\pm\rangle$ with a symmetric superposition of the two APQ excited states. The existence of these strongly correlated quantum states formed by the exchange of a cavity photon shows that both APQs, in the even parity $\mathcal{E}\mathcal{E}$,

coherently interact with an exchange-type coupling and is the main result of this work. However, the spectrum is more complex and requires an additional consideration of parity switching events.

Because parity switching events are expected to occur locally and uncorrelated on the two APQs, four parity configurations can randomly happen during the measurement, namely a single APQ in an odd parity and the other in the even parity, denoted \mathcal{OE} and \mathcal{EO} , or both APQs in the odd or even parity, denoted \mathcal{OO} and \mathcal{EE} , respectively. The eigenenergies of the coupled system in the \mathcal{OE} , \mathcal{EO} and \mathcal{OO} configurations are all shown in Fig. 7.3b). The parity configuration \mathcal{EO} gives rise to two constant resonances that are associated with the transition to the states $|\pm_L\rangle$, reproducing the measurement Fig. 7.2b, because the R-APQ in the odd parity is not coupled to the resonator. The parity configuration \mathcal{OE} adds an avoided crossing between the bare anti-symmetric mode and the R-APQ excited state, because, here, the L-APQ in the odd parity is decoupled from the resonator. These four resonances are seen in the experiment, showing that both APQs switch between parities during a measurement time of 1.5 s. More data of the L-APQ slightly detuned from f_a plotted in the Extended data Fig. E3 can be reproduced in this model with the same device parameters, showing that this quantum system is very versatile, well controlled and well-understood.

7.3. Dual-mode superconducting cavity coupler

In the remainder of this chapter, we discuss about the symmetric of the cavity coupler. We recall the energy level diagram of the capacitively coupled quarter-wavelength coplanar transmission line resonator pair in Fig. 7.4a. The formation of the anti-symmetric voltage mode $|a\rangle$ arises from the coupling capacitance C_m , which hybridizes the two quarter-wavelength modes. The resonator drive tone is capacitively coupled to the middle of the transmission line at C_m such that it couples strongly (weakly) to the symmetric (anti-symmetric) cavity mode with the resonance frequency f_s (f_a), according to the symmetry of the voltage amplitude profiles (Fig. 7.4b-c). We note that the symmetric voltage amplitude is accompanied by the anti-symmetric current amplitude and vice versa.

As explained in Ch. 3, the qubit-cavity coupling is given by the cavity induced phase fluctuation $\delta\phi$ across the NWJJs via the cavity current. This has the consequence that the symmetry of the cavity current implies a phase difference $\Delta\phi$ in the qubit-cavity coupling strength between the two qubits. In the following, we will derive $\Delta\phi$ from the symmetry of the cavity current. We consider the current amplitude at an arbitrary fixed time (Fig. 7.4b-c). In the symmetric mode $|s\rangle$, the cavity current at the short ends is drained in counter directions along the x -axis, from the ground to the cavity. In the

anti-symmetric mode $|a\rangle$, the cavity drains current from ground at one short end and forces current into the ground at the other short end. Because the inductance of the NWJJ is much greater than the shunt inductance, we can assume that the cavity current mainly flows through the shunt inductance and generates a mode dependent flux fluctuation threading the SQUIDs. In the symmetric cavity mode, the external flux fluctuation is along the z -axis and has opposite signs for the two qubit SQUIDs, whereas, in the anti-symmetric mode, it has the same sign.

We now relate the orientation of the external flux fluctuation to $\Delta\phi$ (Fig. 7.4d). First, the superconducting phase in the two grounded epitaxial Al electrodes is set to an equal value ϕ_0 for both NWJJs because of the galvanic connection. As the Lenz's law describes, a change of the magnetic flux through a loop is opposed by a magnetic field in the opposite direction, inducing a current in the loop. For a flux fluctuation in $-z$ -direction, an opposing magnetic field in the z -direction is generated, inducing an anti-clock-wise flowing current in the SQUID. Similarly, a flux fluctuation in z -direction induces a clock-wise flowing current in the SQUID. Using the superconducting phase ϕ_0 on the grounded electrodes and the current direction, we can deduce the phase of the remaining two superconducting electrodes. Fig. 7.4d shows the superconducting phase modulation $\delta\phi$ for both cavity modes. While the absolute value $\delta\phi$ is given by circuit parameters, we are interested in the signs in front of $\delta\phi$, that corresponds to the relative phase difference value. Finally, we obtain a relative phase difference $\Delta\phi = 0$ for the qubit-cavity coupling strength between the two qubits for the symmetric cavity mode $|s\rangle$ and $\Delta\phi = \pi$ for the anti-symmetric cavity mode $|a\rangle$. The phase of the qubit-cavity coupling strength is an insignificant quantity for single qubit experiments, but becomes important in a multi-qubit system.

7.4. Conclusion

In summary, we demonstrate the remote coupling of two APQs over a distance of six millimeters, mediated by a specifically designed superconducting resonator with a strongly and a weakly coupled mode for qubit readout and qubit coupling, respectively. In the resonant regime, the corresponding eigenstates of the full hybrid circuit can be identified using independently determined parameters inserted into the Tavis-Cummings Hamiltonian with two qubits and one cavity mode. At the point at which all energies are degenerate, we find a maximally entangled two-qubit state, mediated by the cavity coupler. Our experiments form a proof-of-principle for cavity-mediated interactions between APQs which might be potentially useful for complex quantum computer architectures. In the future, our results could be transferred to remote Andreev spin qubits in which the spin of an Andreev level is exploited

as a qubit.

7.5. Extended data

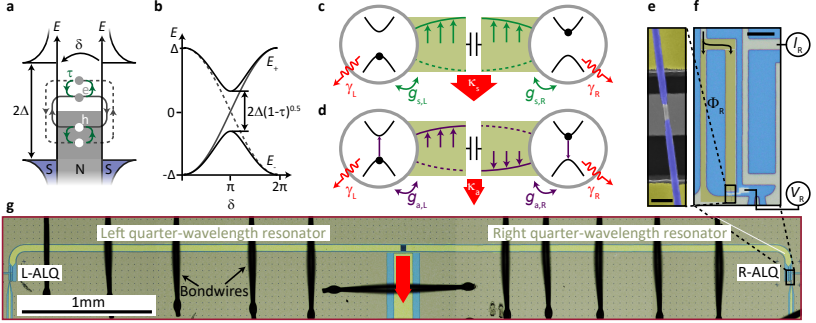


Figure 7.1. Andreev pair qubit (APQ) coupling device. **a**, Andreev bound state (ABS) formation in an S-N-S weak link. In the N region, electron (e) and hole (h) partial waves can constructively interfere to form discrete subgap levels below the gap Δ . The phases of the partial waves obtain contributions from Andreev reflections at the N-S interfaces (curved grey lines) and from the propagation in the N-region (horizontal grey lines). The two spin-degenerate and time-reversed trajectories can be coupled by single-particle scattering (green lines) with probability τ . **b**, The discrete Andreev levels $E_{\pm}(\delta)$ are plotted as a function of the phase difference δ between the two superconducting reservoirs. An energy gap of $2\Delta\sqrt{1-\tau}$ is opened by a finite τ at $\delta = \pi$. **c-d**, Schematics of the complete device containing two APQs (circles) with qubit decay rates $\gamma_{L/R}$ and APQ-coupler coupling strength $g_{s/a,L/R}$ to the two cavity coupler modes. The symmetric mode (green) is used to read out qubit states, while the anti-symmetric mode (purple) is used to coupling the two APQs, with mode dependent coupling rate $\kappa_a \ll \kappa_s$ to the readout port. **e**, A scanning electron micrograph of the right APQ (R-APQ) with epitaxially grown superconducting Al shells (purple), suspended over a metallic bottom gate (grey). The scale bar is 300 nm. **f**, An optical micrograph of the qubit control lines. The junction is galvanically connected to the center conductor in a RF-SQUID geometry (yellow), such that the qubit-coupler coupling is mediated by the currents in the common superconducting leads. The qubit frequency is controlled by a DC gate voltage V_R and the phase control δ_R is generated by a DC current I_R in a flux line. The scale bar is 10 μm . **g**, Composite optical micrographs of the full device. It consists of two capacitively coupled quarter-wavelength coplanar transmission line resonators (light green).

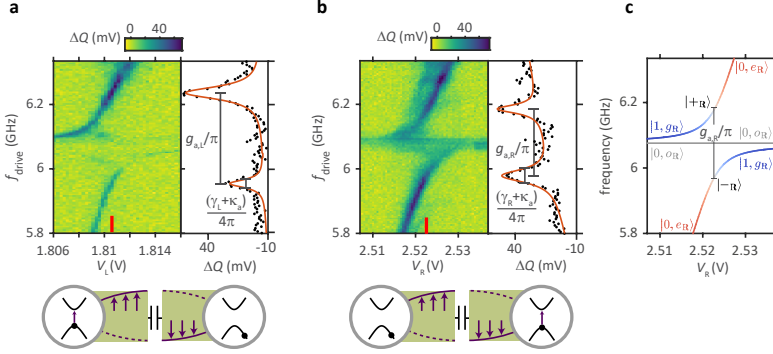


Figure 7.2. Strong coupling between individual APQs and the anti-symmetric coupler mode. **a**, The differential quadrature ΔQ between the two reflected resonator probe pulses at f_s as a function of the qubit excitation frequency f_{drive} and V_L at $\delta_L = \pi$, revealing an avoided crossing between the qubit and coupler resonances. The qubit-resonator coupling rate of $g_{c,L}/(2\pi) = 141$ MHz and the qubit decay rate of $\gamma_L/(2\pi) = 77$ MHz can be directly read out at $V_L = 1.810$ V, as illustrated in the cross-section on the right of the plot. An illustration of the interaction between the resonator and the L-APQ is shown in the bottom insert. The interaction with the R-APQ is suppressed by tuning the R-APQ frequency to a larger value with $\delta_R = 1.2\pi$, while keeping $V_R = 2.5225$ V. **b**, Similarly, an individual strong coupling between the R-APQ and the anti-symmetric coupler mode is observed at $V_R = 2.5225$ V, with $g_{c,R}/(2\pi) = 104$ MHz and $\gamma_R/(2\pi) = 82$ MHz. The horizontal resonance at $f_{\text{drive}} \approx 6.075$ MHz occurs as the occupation of the odd state due to quasiparticle poisoning. It is missing in **a** because of small excitation power seen by the circuit. **c**, Calculated excitation spectrum as a function of the V_R using the listed parameters, quantitatively reproducing the measured spectrum in **b**). The two resonances correspond to the qubit-coupler hybrid states $|\pm_R\rangle$, with the color indicating the single qubit weight $|\langle 0, e_R | \pm_R \rangle|^2$.

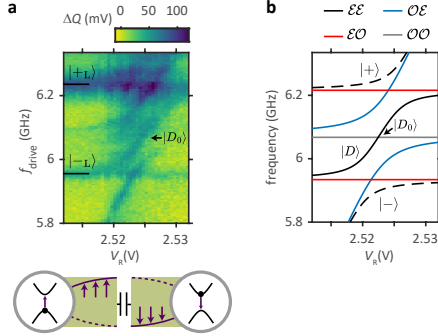


Figure 7.3. Remote coupling of two APQs. **a**, The differential quadrature ΔQ plotted as a function of V_R for the case when both APQs are tuned into resonance with the anti-symmetric resonator mode ($\delta_L = \delta_R = \pi$, $V_L = 1.810$ V). The states causing the individual resonances are identified in **b** and explained in the main text. Most relevant is the resonance $|D\rangle$, which corresponds to a two-qubit hybrid state with an anti-symmetric superposition of the two APQ excited states. The increase contrast for features at high f_{drive} is caused by the vicinity to the symmetric coupler mode frequency. **b**, Calculated excitation spectrum as a function of the V_R using the Tavis-Cummings model with two qubits, one resonator mode and the parameters found independently in Fig. 7.2. The plotted spectrum contains excitation spectra of different parity configurations distinguished by colors (\mathcal{E} = single APQ even parity, \mathcal{O} = single APQ odd parity). The dashed black lines correspond to the two hybrid states with a symmetric superposition of the two qubit states while the solid line corresponds to that with an anti-symmetric superposition of the two qubit states.

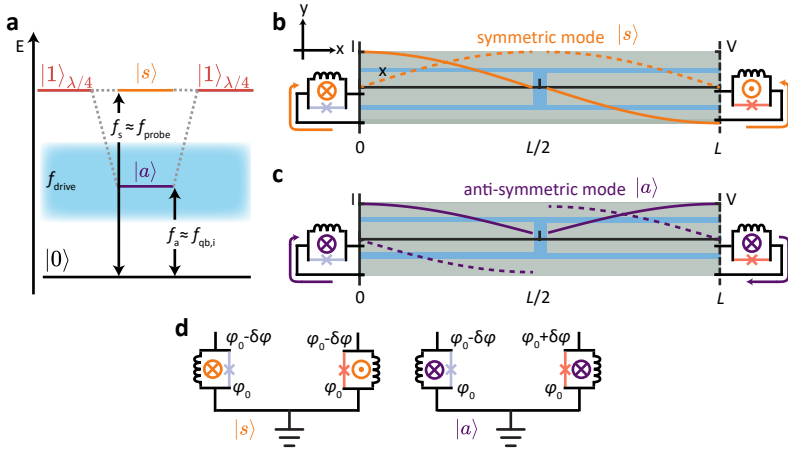


Figure 7.4. Symmetric and anti-symmetric mode of the cavity coupler. **a**, Energy level diagram of the two cavity modes ($f_s > f_a$). Cavity probe frequency f_{probe} is set to populate the symmetric mode $|s\rangle$ while the qubits are tuned close to the anti-symmetric mode $|a\rangle$. f_{drive} is varied in the blue window for the qubit spectroscopy. **b-c**, Current (solid) and voltage (dashed) amplitude of the symmetric voltage mode $|s\rangle$ and anti-symmetric voltage mode $|a\rangle$ along the cavity. The long arrows indicate the relative flow direction of the cavity current with respect to each other, while the symbols in the loops show the relative direction of the induced external flux. **d**, The superconducting phase difference across the NWJJs generated by the cavity current in both cavity modes. In the symmetric cavity mode, the induced phase difference is in-phase, whereas, in the anti-symmetric cavity mode, $\Delta\phi = \pi$.

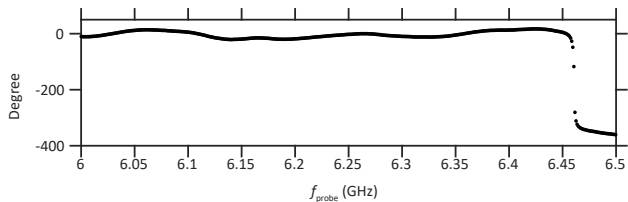


Figure E1. Coupler spectrum. The phase of a weak microwave probe pulse as a function of the probe frequency f_{probe} . No phase shift is observed at 6.075 GHz, showing that the anti-symmetric coupler mode is weakly coupled to the readout port with considerably smaller κ_a . At 6.461 GHz, a phase shift of 360° is measured, which results from the reflection of the symmetric coupler mode.

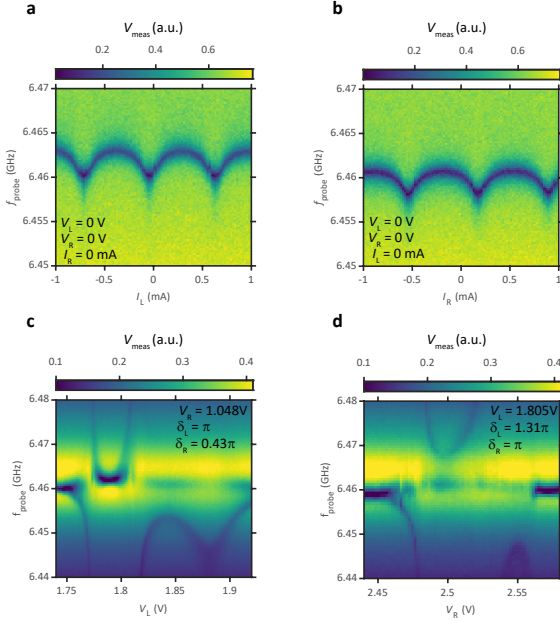


Figure E2. Reflection spectrum of the symmetric coupler mode. **a**, The voltage of a reflected weak coupler probe pulse as a function of the probe frequency f_{probe} and DC current I_L near the symmetric mode frequency f_s . The symmetric mode resonance is periodically modulated by flux biasing the left rf-SQUID. Similar behavior is observed when changing I_R , as depicted in **b**. The π -points are identified as the current values with the lowest resonance frequency. **c-d**, A transition of the L-APQ (R-APQ) is tuned across f_s at $\delta_L = \pi$ ($\delta_R = \pi$), creating a gate dependent shift of the symmetric mode resonance. The resonance at f_s in addition to the shifted resonance is characteristic for Andreev qubits and indicates finite dwell time in the odd parity. The gate voltage independent background is caused by the finite bandwidth of the JPA.

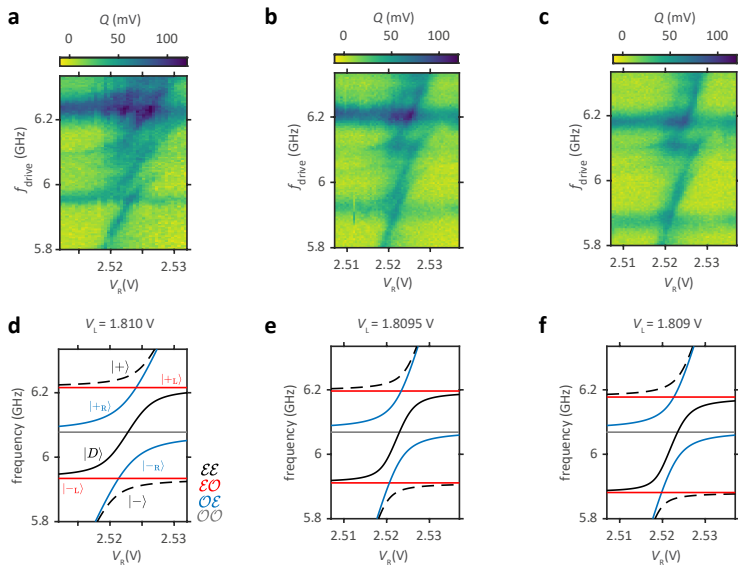


Figure E3. Extended spectroscopy measurements of the full hybrid circuit at different V_L . **a** and **d** are also shown in the Fig. 7.3 in the main text. The spectra in **b** and **c** are measured by step-wise reducing V_L . **e** and **f** are calculated spectra using the Tavis-Cummings model with $f_{\text{qb},L} = 0.993 f_a$ and $f_{\text{qb},L} = 0.985 f_a$. Crucially, as the L-APQ is detuned from the anti-symmetric mode frequency f_a , the sigmoid-shaped two-qubit entangled state $|D\rangle$ (solid black) approaches the single APQ-coupler state $|{-R}\rangle$ (blue) from the parity configuration $\mathcal{O}\mathcal{E}$, in agreement to the measured spectra in **b** and **c**.

8 Gatemon qubit using Ge/Si core/shell nanowire Josephson junctions¹

The study of InAs/Al nanowire Josephson junctions unfolds the spin degree of freedom in the Andreev spectrum in the presence of spin-orbit interaction. A qubit can be encoded in the spin space, featuring a long energy relaxation time because of the weak coupling to the small magnetic moment of a spin. Albeit having a longer T_1 than that of an Andreev pair qubit, previous experiments with Andreev spin qubits in InAs nanowires have shown short dephasing time due to spin-specific noise [27]. In fact, group III/V semiconductors have the inherent shortcoming of a nuclear spin bath which causes nuclei spin exchange flip-flops, a mechanism that generates a random fluctuating magnetic field acting on the qubit spin and hence leads to qubit decoherence [113]. For normal spin qubits, the nuclei-induced dephasing time could be improved by two orders of magnitude by just exchanging the group III/V semiconductor with group IV semiconductor as host material [114]. This exchange of material is a step that is downright transferable to Andreev based qubits. We propose using Ge/Si core/shell nanowires as the weak link, a group IV semiconductor that possesses a strong lateral confinement, direct Rashba spin-orbit interaction and highly transparent semiconductor-superconductor interface with Al.

To verify the fabrication processes and integrability of a few-modes transparent SNS Josephson junctions using Ge/Si core/shell nanowires, we took the step to first fabricate and characterize a gatemon qubit integrating the Ge/Si nanowire as Josephson element. In particular, the measurement of the qubit transition frequency will reveal the critical current of the Josephson element. The fabrication of first a gatemon device was preferred over an Andreev qubit device. Because of the numerous transitions in the Andreev spectrum, sometimes an Andreev qubit is more cumbersome to understand.

This chapter starts with a brief introduction to the Ge/Si core/shell nanowire and the superconducting gatemon qubit, involving the qubit manipulation and readout². Sec. 8.1 presents the device under test, followed by the measurement

¹This experiment was conducted in collaboration with Han Zheng, a PhD student in the Nanoelectronics lab, Nikunj Sangwan, a master's thesis student from EPFL, Switzerland, and Tom Jenniskens, a master's thesis student from University of Twente.

²The sections about qubit manipulation and readout read very similar to the ones for Andreev qubit. However, the transition and coupling for gatemon qubits are addressed

in the frequency domain in Sec. 8.2 and in the time domain in Sec. 8.3.

Ge/Si core/shell nanowires

Coherently strained Ge/Si core/shell nanowires accumulate holes as charge carriers in the Ge core due to its bandgap alignment. It was proposed as an interesting material platform primarily for quantum dot related applications, such as spin qubits, due to its large spin-orbit energy allowing electrical spin control [115, 116].

Electrical studies on the performance of the nanowire devices have been conducted to correlate the hole mobility and crystal orientation with the nanowire diameters [117]. A field-effect mobility at liquid He temperature as high as $4000 \text{ cm}^2/\text{Vs}$ was measured in the Ge/Si nanowires, with an average value of $2500 \text{ cm}^2/\text{Vs}$, for small nanowire diameters ($< 30 \text{ nm}$), growing preferably in the [110]- and [112]-direction. In comparison, the field-effect mobility in Al-etched InAs/Al nanowires from the group of Professor Peter Krogstrup at the University of Copenhagen was found to be $1000 \text{ cm}^2/\text{Vs}$ on average, about two times lower than that in the Ge/Si nanowires [118]. This finding highlights the use of Ge/Si core/shell nanowires for electronic nanodevices. Later, Florian Froning *et al.* demonstrated coherent manipulation of a hole spin qubit in these nanowires, together with an enhanced, gate-tunable g -factor that is expected from the predicted strong direct Rashba SOI [119, 120].

A crucial step towards superconductor-semiconductor hybrid devices using the Ge/Si nanowire was made by Joost Ridderbos *et al.*, when they managed to induce Josephson current through the nanowire [82, 121, 122]. For that, a non-trivial fabrication technique was developed to thermally activate an inter-diffusion process between Ge and evaporated Al that are in electrical contact, creating an Al/Ge/Al nanowire Josephson junction (NWJJ). Electrical measurements manifested high interface transparencies and a hard superconducting gap for this type of hybrid devices [121, 123].

Motivated by the promising transport measurements of the superconductivity in these hybrid devices, we would like to enable the use of these nanowires in our lab. The first step is the establishment of highly transparent JJs using these nanowires. By shunting the nanowire device with a large capacitance, we fabricated a transmon qubit, where the non-linearity originates from the Josephson coupling [101]. Following the device architecture of Ref. [45, 124], we embed our Ge/Si NWJJ in a gate tunable transmon, denoted by "gatemon", and investigate its quantum coherence properties.

via the complementary charge degree of freedom.

Gatemon qubits

As with conventional transmon qubits, semiconducting nanowire transmons operate as a non-linear quantized LC -circuit in the lowest two collective electromagnetic excitations ($|0\rangle, |1\rangle$), where the non-linearity is given by the NW Josephson inductance. The hallmark feature of a transmon is the increased shunt capacitance in comparison to a Cooper pair box[101]. It reduces the charge dispersion and hence suppresses charge noise. In our device, the qubit capacitance C_{qb} is given by a large planar superconducting island with respect to the ground yielding a charging energy of $E_C = e^2/2C_{\text{qb}}$. On the other hand, the semiconducting region of the NWJJ allows a gate tunable supercurrent $I_c(V_G)$ that gives rise to a tunable Josephson energy $E_J(V_G) = \Phi_0 I_c(V_G)/2\pi$. Due to the increased capacitance in the transmon limit $50 < E_J/E_C < 100$, the first two transition frequencies of the non-linear spectrum is very close. Their difference is given by the anharmonicity parameter $\alpha = f_{21} - f_{10} = -E_c$, the qubit frequency is given by $f_{01} \approx \sqrt{8E_C E_J(V_G)}/h$.

Gatemon manipulation

We consider a qubit with the Hamiltonian $\hat{H}_{\text{qb}} = hf_{\text{qb}}\hat{\sigma}_z/2$ and an electric dipole moment $\hat{d} = d\vec{e}_x\hat{\sigma}_x$. The qubit experiences a drive pulse that is a coherent light of the form $\vec{E}(t) = E \cos(2\pi f_d t)\vec{e}_x$. The interaction is described by the Hamiltonian $\hat{H}_{\text{int}} = -\vec{E}(t) \cdot \hat{d}$. The total Hamiltonian describing the qubit under interaction with a drive pulse then reads [125]

$$\hat{H}(t) = \frac{hf_{\text{qb}}}{2}\hat{\sigma}_z - A \cos(2\pi f_d t)\hat{\sigma}_x, \quad (8.1)$$

where $A = Ed$ is the coupling strength between the coherent drive and the qubit. To eliminate the time dependence, we transform the Hamiltonian using the unitary operator $U(t)$:

$$\hat{\mathcal{H}} = U(t)\hat{H}U^\dagger(t) - iU(t)\dot{U}^\dagger(t). \quad (8.2)$$

In particular, $U(t) = e^{-\pi f_d t \hat{\sigma}_z}$ transforms the Bloch sphere from the lab frame to a frame rotating about the z-axis at a frequency f_d . In this so-called rotating frame approximation, The Hamiltonian is time-independent:

$$\hat{\mathcal{H}} = -\frac{\Delta_d}{2}\hat{\sigma}_z - \frac{A}{2}\hat{\sigma}_x, \quad (8.3)$$

with $\Delta_d/2\pi = f_{\text{qb}} - f_d$ being the detuning. The total Hamiltonian can be exactly diagonalized, yielding the eigenvalues $E_{\pm} = \pm\sqrt{A^2 + \Delta_d^2}/2$ and eigenstates

$$|V_-\rangle = \cos(\theta)|e\rangle - \sin(\theta)|g\rangle, \quad (8.4)$$

$$|V_+\rangle = \sin(\theta)|e\rangle + \cos(\theta)|g\rangle, \quad (8.5)$$

where $\theta = \tan^{-1}\left(\frac{A}{\sqrt{A^2 + \Delta_d^2} - \Delta_d}\right)$. Then, the evolution of a state $|\Psi(t)\rangle$ under the action of $\hat{\mathcal{H}}$ has the form

$$|\Psi(t)\rangle = \sum_{j \in \{+, -\}} C_j e^{-iE_j t} |V_j\rangle, \quad (8.6)$$

where C_i is determined by the starting point. Finally, for a qubit starting in $|g\rangle$, the evolution reads [125]

$$|\Psi(t)\rangle = -i \sin(E_+ t/\hbar) \sin(2\theta) |e\rangle + \cos(E_+ t/\hbar) \sin(2\theta) |g\rangle. \quad (8.7)$$

In the presence of the drive pulse, the qubit vector rotates at a frequency of $E_+/\hbar = \sqrt{A^2 + \Delta_d^2}/2\hbar$. The oscillation is the slowest and has the highest contrast ($\sin(2\theta) = 1$) when the drive frequency matches the qubit frequency ($\Delta_d^2 = 0$). Later in the device section, we will relate the coupling strength A to circuit parameters.

Gatemon readout

Qubit state readout is performed via a microwave resonator that is dispersively coupled to the qubit. The interaction, which is identical to a Jaynes-Cummings Hamiltonian, is slightly modified due to the reduced anharmonicity. Because of the large shunt capacitance, frequencies of higher transitions become similar to the qubit transition frequency, i.e., $f_{01} \approx f_{12}$, leading to a renormalization of the characteristic energies. The effective total Hamiltonian of the dispersively coupled qubit-resonator system reads [101]

$$\hat{H}_{\text{eff}} = \frac{\hbar f'_{01}}{2} \hat{\sigma}_z + (\hbar f'_r + \frac{\hbar \chi}{2\pi} \hat{\sigma}_z) \hat{a}^\dagger \hat{a}, \quad (8.8)$$

where $f'_{01} = f_{01} + \chi_{01}/2\pi$ is the renormalized qubit frequency, $f'_r = f_r - \chi_{12}/4\pi$ the renormalized resonance frequency and $\chi = \chi_{01} - \chi_{12}/2$ the effective dispersive shift. The dispersive shift is defined as $\chi_{ij} = g_{ij}^2/2\pi(f_j - f_i - f_r)$. In case the anharmonicity is large, the coupling of the transition $|1\rangle \leftrightarrow |2\rangle$ to the resonator is negligible ($\chi_{12} \approx 0$) and we restore the Jaynes-Cumming Hamiltonian with a true two-level qubit, $f'_r \approx f_r$ and $\chi \approx \chi_{01}$. The qubit occupation is reflected in the shift of the resonance frequency, that can be probed with a resonator probe pulse at $\sim f'_r$.

8.1. Device

Fig. E1a shows a scanning electron micrograph of the Ge/Si core/shell nanowire used to form a NWJJ³. The nanowire consists of a monocrystalline Ge core

³The resonators were fabricated by L.Y. Cheung and N. Sangwan. The nanowires were deposited and contacted by H. Zheng, T. Jenniskens and N. Sangwan.

with a diameter of ~ 20 nm and a Si shell thickness of 2 nm covered by a native SiO_2 [121]. It is deposited on the resonator chip using a micromanipulator. A side gate and contacts of Al for the nanowire are evaporated (dark blue), after removing the SiO_x and Si shell in the contact area with wet etching techniques. Subsequently, the chip is placed on a hotplate at 200°C for 10 minutes to initiate Al diffusion into the Ge core, forming an Al/Ge/Al-junction with a Ge segment of ~ 30 nm long and sharp interfaces (light blue). With the contact metallization, the nanowire junction is electrically connected to the NbTiN island that generates a parallel capacitance C_{qb} to the ground (Fig E1b). We use Sonnet simulation to estimate the qubit capacitance and find $C_{\text{qb}} \approx 78$ fF, yielding a charging energy of $E_c/h \approx 250$ MHz. An equivalent circuit is illustrated in Fig E1c, featuring the readout resonator, which is a NbTiN quarter-wavelength coplanar transmission line resonator, mutually coupled with a feedline in a hanger configuration. The gatemon is capacitively coupled to the resonator (C_g). The metallic gate is connected to a voltage source V_G for tuning the semiconducting region of the nanowire junction. In the final step, Al is evaporated, electrically contacting the NbTiN ground plane. The presence of Al can drain non-equilibrium quasiparticles that reside in the NbTiN due to the smaller superconducting gap [126].

For the gatemon qubit, the coupling strength between the coherent electromagnetic drive and the qubit can be expressed in circuit parameters, $A = 2e\beta\langle 0|\hat{n}|1\rangle v$, where e is the elementary charge, β is the capacitance ratio C_g/C_{qb} , $\langle 0|\hat{n}|1\rangle$ is the matrix element that couples both states and v is the drive voltage amplitude. Both the qubit drive pulse and resonator readout pulse are routed through the feedline. The resonator readout pulse is amplified with a Josephson parametric amplifier at base temperature, a HEMT amplifier at 4 K and a room temperature amplifier before reaching the heterodyne detection setup.

Fig. E1d shows the normalized transmission line coefficient A/A_0 through the feedline as a function of the nanowire gate voltage V_G at low probe power. The resonance, stemming from the readout resonator, is observed to vary as a function of V_G . Because Ge/Si core/shell nanowires have hole-type conduction, a more negative gate voltage induces more charge carriers in the semiconducting region. The resonance frequency is shifted upwards due to dispersive coupling to the gatemon transition $|0\rangle \leftrightarrow |1\rangle$, whose frequency increases with the gate-tunable supercurrent, $\propto \sqrt{I_C(V_G)}$. As marked with arrows, the dispersive shift exhibits resonance features, indicating fluctuation in the junction transparency [122, 127]. The bare resonance frequency can be deduced at large positive V_G , where the Ge core is depleted, to be $f_r = 6.353$ GHz, where the semiconducting region is depleted.

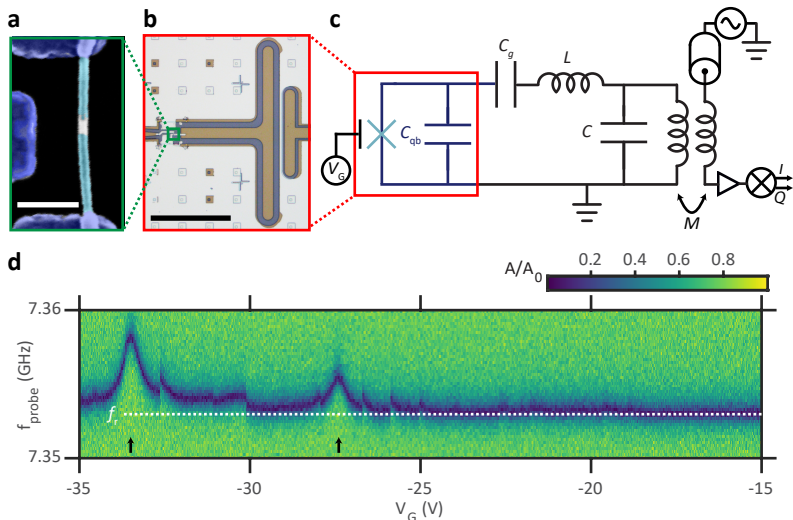


Figure E1. Ge/Si core/shell nanowire Josephson junction. **a**, False-colored scanning electron micrograph of the Ge/Si core/shell NWJJ. Al is evaporated to electrically contact the nanowire and form a side gate (dark blue). Al atoms diffuse into the Ge core (bright blue) forming a ~ 30 nm-long Al/Ge/Al-junction. The scale bar is 100 nm. **b**, Optical micrograph of the NbTiN gatemon island that is capacitively coupled to a readout resonator. The surrounding NbTiN ground plane is coated with evaporated Al for trapping quasiparticles. The scale bar is $150 \mu\text{m}$. **c**, Equivalent circuit diagram of the full device. The resonator is mutually coupled to the readout circuit in a hanger configuration. Microwave pulses are transmitted through the feedline and amplified before the heterodyne detection scheme. **d**, Normalized transmission A/A_0 through the feedline around f_r as a function of V_G . The white dashed line indicates the bare resonance frequency deduced from the depletion regime.

8.2. Gatemon spectroscopy

We now demonstrate the gatemon transition in the frequency domain. The qubit transition frequency is measured using pulsed two tone spectroscopy: a saturating drive pulse of 500 ns is sent to the feedline to address the qubit transition before a resonator probe pulse with $1 \mu\text{s}$ pulse width is sent. The difference between the quadrature values of the transmitted probe pulse and that with the qubit in its ground state integrated over $1 \mu\text{s}$ yields the quadrature value Q . It is further normalized to obtain the normalized change of the quadrature value Q/Q_0 .

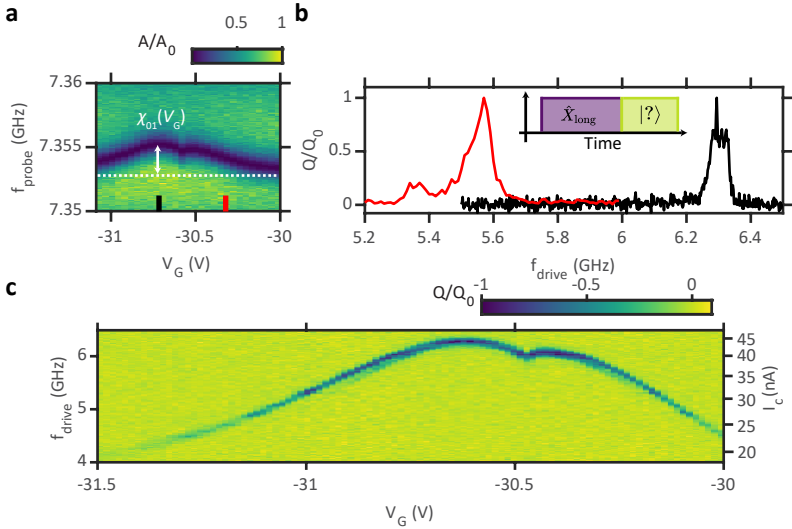


Figure E2. Gatemon spectroscopy. **a**, Normalized transmission A/A_0 through the feedline around f_r as a function of V_G . The dispersive shift $\chi_{01}(V_G)$ can be extracted as the difference to f_r . **b**, Normalized change of the quadrature value Q/Q_0 of the weak resonator probe pulse as a function of f_{drive} in pulsed two-tone spectroscopy. Color correspond to the marks in **(a)**. The inset shows the pulse scheme with a long saturating drive pulse and a cavity readout pulse. **c**, Q/Q_0 of the weak resonator probe pulse as a function of f_{drive} and V_G in pulsed two-tone spectroscopy. This spectrum is taken weeks after the measurement in **(a)** and shifted with respect to the single tone measurement due to gate drifts. The drive frequency f_{drive} is converted to a critical current I_c on the right y-axis.

First, the junction is gated to a region where a dispersive shift occurs (Fig. E2a). The dispersive shift χ_{01} can be estimated from the difference of the shifted resonance frequency and f_r [101]. We then measure Q/Q_0 as a function of the qubit drive frequency f_{drive} at the two marked gate voltage values. Fig. E2b shows the qubit spectral lines where the resonances are associated to the qubit transition $|0\rangle \leftrightarrow |1\rangle$. The qubit transition frequency f_{01} is estimated by fitting a Lorentzian lineshape to the resonance. Using $g_{01} = \sqrt{(f_{01} - f_r)\chi_{01}}$, we obtain the cavity coupling strength $g_{01}/2\pi = 47.7 \text{ MHz} \pm 1.4 \text{ MHz}$ from the transition $|0\rangle \leftrightarrow |1\rangle$ from data at these two gate voltage values.

Fig. E2c shows the qubit dispersion as a function of V_G in a large range. The gatemon transition comes from low frequencies and saturates at $V_G \approx -30.6 \text{ V}$. The abrupt change of the dispersion at around -30.45 V is caused by charge rearrangement. The signal Q/Q_0 at low f_{01} starts to fade out due to reduced qubit-cavity coupling. This two tone spectrum was measured weeks after the single tone measurement in Fig. E2a. Although it is shifted with respect to the previous measurement, most of the features are similar, highlighting the stability of our NWJJ-based gatemon. The critical current I_c in the NWJJ can be extracted by using $f_{01} \approx \sqrt{8E_C E_J(V_G)}/h$. Its value is plotted to the right y-axis of the spectrum, showing a maximum supercurrent of $\sim 40 \text{ nA}$, which is in agreement with dc transport measurements with nanowires with similar diameter and junction length in Ref. [122]. The estimated E_J/E_C ratio for the highest transition frequency at $\sim 6.3 \text{ GHz}$ is ~ 90 , well in the transmon limit featuring reduced sensitivity to charge fluctuation [101].

8.3. Quantum coherence

We now study the gatemon in the time domain. The transition frequency is set to the gate sweetspot for the study to mitigate electric noise induced by charge fluctuation. First, the gatemon is rotated around the x-axis to a superposition state with a \hat{X}_ϕ -gate of variable power and pulse width t_{rabi} at $f_{\text{drive}} = 6.345 \text{ GHz}$ before the cavity readout pulse is sent in (Fig. E3a, top). The normalized change of the quadrature value Q/Q_0 of the cavity probe pulse is plotted in Fig. E3a. The rotation of the qubit state vector around the x-axis results in so-called Rabi oscillations, indicating a coherent control about the x-axis. As the power of the \hat{X}_ϕ -gate increases, the Rabi oscillation becomes faster. We extract the oscillation frequency f_{rabi} by fitting a sinusoidal function with an exponential decay to the data and plot it as a function of the normalized drive amplitude V_d that is defined with respect to 5 dBm: $V_d = \sqrt{10^{(\text{Power}[\text{dBm}] - 5 \text{ dBm})/10}}$ (Fig. E3b). The measured oscillation frequency f_{rabi} deviates from the linear model at $f_{\text{rabi}} \gtrsim \alpha$. This is expected in the presence of a multilevel quantum system due to leakage to higher excited

states at high power, when the Rabi frequency exceeds the anharmonicity [128–130].

Fig. E3c shows Rabi oscillations as a function of drive frequency f_{drive} at a power of -10 dBm in the linear drive power range. We identify f_{01} as the drive frequency with the slowest oscillation frequency. When addressing the gatemon at exactly f_{01} , the qubit drive pulse as well populates the cavity due to finite qubit-cavity coupling, saturating the Rabi contrast in Q at high drive pulse width which complicates the qubit state discrimination. The large signal below f_{01} is identified as the frequency $f_{02}/2$ associated with a two-photon excitation for the gatemon transition $|0\rangle \leftrightarrow |2\rangle$, which also commonly appears in other transmon platforms [131, 132]. Using $\alpha = 2(f_{02}/2 - f_{01})$, we obtain an anharmonicity of ~ -116 MHz. The measured α is about two times smaller than the simulated value ($\alpha_{\text{sim}} = -E_c \approx 250$ MHz). This behaviour was observed in InAs/Al nanowire gatemons as well. In Ref. [45], the authors argue that the reduced anharmonicity in the measurement could be caused by a non-sinusoidal current phase relation. In fact, Albert Hertel showed in his dissertation that highly transparent channels, with transparencies approaching the unity, can reduce the anharmonicity by a factor of four in comparison to a tunnel junction with sinusoidal current phase relation (Sec. 2.6 from the dissertation [59]). Further study using a flux-tunable device is needed to confirm this speculation for our Ge/Si core/Shell NWJJs.

We studied the coherence of our NWJJ gatemon using Ramsey interferometry techniques. The qubit state vector is first rotated into the xy-plane with a 6 ns-long $\hat{X}_{\pi/2}$ gate, using a calibrated drive amplitude from previous measurement. At finite detuning $\Delta_f = f_{\text{drive}} - f_{01}$, the qubit precesses around the z-axis and acquires over a wait time t_{wait} a phase $\phi = 2\pi\Delta_f t_{\text{wait}}$. Depending on ϕ , a second $\hat{X}_{\pi/2}$ gate promotes the state vector towards $|1\rangle$ or $|0\rangle$. The corresponding oscillations along the z-axis is evident for a coherent control about the z-axis [132]. With the coherent control about the x- and z-axis, the whole Bloch sphere becomes accessible. Fig. E3d shows the Ramsey fringes as a function of f_{drive} and t_{wait} . Precession about the z-axis is observed up to 200 ns. At some $t_{\text{wait}} \approx 110$ ns, the fringes vanish and reenter after a short time, displaying a beating pattern. We perform a discrete Fourier transform (DFT) on the time traces to study the frequency components of these fringes, see Fig. E3e. The Ramsey oscillation frequency indeed increases linearly with the detuning Δ_f , following the linear dashed lines. A second oscillation frequency, that creates the beating pattern in the time domain, can not be resolved from this study.

Finally, we also measure the energy relaxation and dephasing time of the gatemon. We first prepare the qubit in the $|1\rangle$ with a 10 ns-long \hat{X}_{π} gate and let it decay without perturbation over a time t_{wait} , before switching on the cavity probe pulse. The quadrature value Q is converted into the occupation of the excited state $P_{|1\rangle}$ using Q/Q_{max} , with Q_{max} being the quadrature value

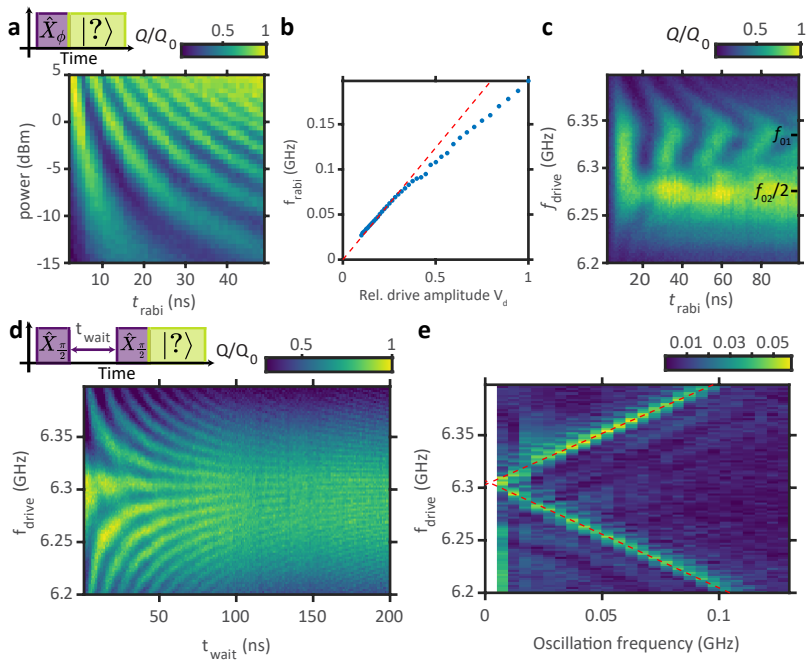


Figure E3. Coherent manipulation of the gatemon. **a**, The qubit is excited with a drive pulse before the qubit state readout. Q/Q_0 of the weak resonator probe pulse is plotted as a function of the drive pulse width t_{rabi} and drive power. f_{drive} is set to 6.345 GHz. **b**, Rabi frequency f_{rabi} as a function of the relative drive amplitude. The dashed line is a linear fit to the low power range. **c**, Q/Q_0 of the weak resonator probe pulse as a function of t_{rabi} and f_{drive} . Transition frequency f_{01} and $f_{02}/2$ are indicated. The drive power is set to -10 dBm. **d**, Ramsey experiment as a function of wait time t_{wait} and f_{drive} . The drive pulse sequence contains two 6 ns-long $\hat{X}_{\pi/2}$ pulses separated by a wait time. **e**, A discrete Fourier transform (DFT) of (d). The x-axis is DFT frequency. Dashed lines indicate the expected frequency at which the Ramsey fringes should oscillate.

immediately measured after the preparation. $P_{|1\rangle}$ is plotted against t_{wait} in Fig. E4a, following an exponential decay. An exponential fit to the probability yields an energy relaxation time of $T_1 = 1.27 \mu\text{s}$.

Ramsey fringes were measured at a detuning of $\Delta_f \approx 80 \text{ MHz}$, using two 6 ns-long $\hat{X}_{\pi/2}$ pulses and a wait pulse in between. The drive detuning is set to obtain many oscillations for an accurate fitting. Fig. E4b shows the converted $P_{|1\rangle}$ as a function of t_{wait} . The conversion to the excited state occupation uses the same Q -axis conversion as for the T_1 -measurement. The oscillations with a beating pattern is fitted using two sinusoidal functions with different exponential envelopes: $A_1 \exp(-t_{\text{wait}}/T_{2,i}^*) \sin(2\pi f_1 t_{\text{wait}} + \phi_1) + A_2 \exp(-t_{\text{wait}}/T_{2,ii}^*) \sin(2\pi f_2 t_{\text{wait}} + \phi_2) + B$. The two extracted oscillation frequencies are $f_1 \approx 86.03 \text{ MHz}$ and $f_2 \approx 80.21 \text{ MHz}$ with characteristic decay times of $T_{2,i}^* \approx 57 \text{ ns}$ and $T_{2,ii}^* \approx 144 \text{ ns}$.

In fact, the two oscillation frequencies are very close to each other, which can also be the reason why these two two-level systems are not resolved in the Rabi measurement in Fig. E3c. We speculate that the two oscillation frequencies could stem from charge parity fluctuation, caused either by charge traps in the oxide near the qubit capacitance or NW, or by quasiparticle poisoning in the junction [133, 134]. Future devices with an enhanced charge dispersion and a lower E_J/E_C ratio could act as a charge parity detector and be measured to deduce the poisoning rates [135].

8.4. Conclusion

We have fabricated a superconductor-semiconductor-based nanowire gatemon using a Ge/Si core/shell nanowire. Owing to the Al/Ge interdiffusion process, an Al/Ge/Al JJ of $\sim 30 \text{ nm}$ was formed and found to host large critical current. We have demonstrated for the first time coherent control around both the x- and z-axis and measured both the relaxation and dephasing time in a Ge/Si core/shell nanowire based gatemon, highlighting the quantum coherence of our qubit⁴. A continuation of current work could be a quantitative study of the quantum coherence as a function of gate. Because the Ge/Si core/shell nanowire with interdiffused Al is a material platform with transparent superconductor-semiconductor interfaces and limited number of modes due to its quasi-1D confinement, it will be interesting to perform microwave spectroscopy of the ABSs in such a NWJJ. Particularly, the strong direct Rashba SOI, which was predicted for this type of nanowires, could lead to

⁴During the preparation of this experiment, we became aware of a preprint of similar works from an independent group, see [136]. To our best knowledge, the authors of that work have not shown direct measurement of Ramsey fringes due to fast qubit dephasing in their gatemon qubit. In addition, the energy relaxation time of their gatemon qubit seems to be only 10% of ours. We believe that our findings are still interesting to report on, which could better represent the full potential of Ge/Si core/shell nanowire Josephson junctions.

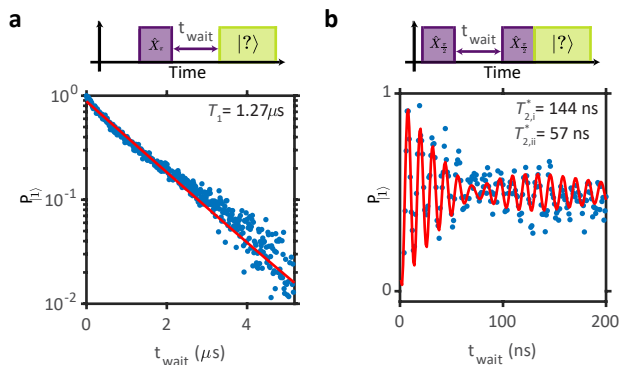


Figure E4. Quantum coherence. **a**, Energy relaxation time measurement. The qubit is prepared in the excited state $|1\rangle$ with a 10 ns-long \hat{X}_π -gate. The wait time t_{wait} between excitation and readout is varied. The quadrature value Q of the readout pulse is converted to an excited state probability $P_{|1\rangle}$. The line is an exponential fit to $P_{|1\rangle}$. **b**, Ramsey fringes measurement. The Ramsey sequence is performed at a drive detuning $\Delta f \approx 80$ MHz. The line is a fit function to $P_{|1\rangle}$ with two oscillation frequencies, each enveloped with an exponential decay.

new intriguing Andreev physics. Moreover, unlocking the spin degree of freedom of localized ABSs in group IV material could significantly improve the spin dephasing time in comparison to platforms using semiconductors of the group III/V, following the path for normal spin qubits (III/V: [3, 137–139], IV:[114, 140, 141]).

9 Experimental techniques

This chapter is dedicated to the description of the important experimental methods for this thesis. It starts with the explanation of device fabrication in the Sec. 9.1, followed by the discussion of the microwave sample holder in Sec. 9.2. After that, Sec. 9.3 and Sec. 9.4 illustrate the wiring of the cryostat and room temperature setups for the two major experiments of this thesis. Finally, Sec. 9.5 presents a protocol to characterize superconducting qubits, summarizing the technical knowledge we obtained about qubit measurement in this doctoral study.

9.1. Device fabrication

The starting point of nanowire devices is always an undoped Si wafer, sometimes with a layer of thermally grown SiO₂. The first step is the fabrication of high- Q superconducting resonators on the wafer.

NbTiN resonators

For all the presented experiments, NbTiN coplanar transmission line resonators were used as qubit state detectors. The steps for wafer cleaning and NbTiN sputtering are identical as described in Ref. [142]. Because the resonators are big structures on the scale of micrometers, they are patterned using a Heidelberg instrument μ MLA direct laser writer. The 85 nm NbTiN film is first covered with a 500 nm-thick layer of Microposit S1805 optical resist and baked at 125°C for 120 s. The regions which are exposed to the laser is then stripped in Microposit MF-319 developer with a development time of 50 s. Subsequently, the resonators are formed by dry etching the gaps in an inductively coupled reactive ion etching plasma machine (ICP) in an Ar/Cl₂ environment. Afterwards, the remaining optical resist is removed by sonication in AR 300-70 remover (NEP) for 10 mins at 100% power. The chip is then rinsed in acetone and IPA, followed by blow-drying with pressurized air. The sonication in NEP is crucial for the removal of the optical resist. We found out that sonication in acetone is not strong enough to fully remove the optical resist and suspected that the ICP cross-linked and hardened the resist. Now, the resonator chip is ready for nanowire deposition.

Nanowire deposition

Nanowires were transferred to the resonator chip from the growth chip using a micromanipulator (Fig. E1a). This instrument consists of a microscope and an arm that controls a glass needle with micrometer precision. Using the glass needle, the nanowires are mechanically picked up and then deposited on the resonator chip. Finally the chip was rinsed in IPA to increase the adhesion of the nanowires to the surface and blow-dried.

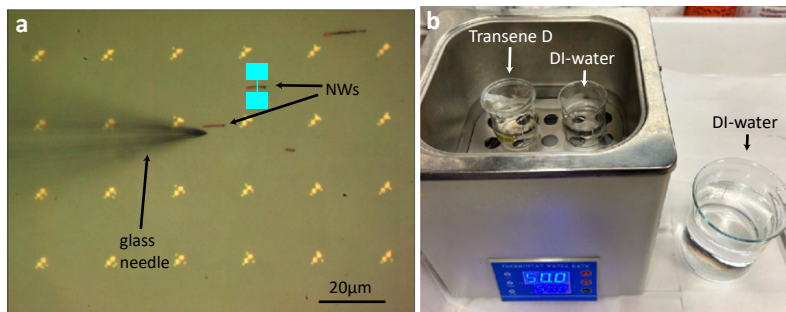


Figure E1. **a**, Optical micrograph of the chip in the micromanipulator setup. The nanowires are seen with the glass needle coming from the left. The cyan structure illustrates an Al etch window. **b**, A beaker of Transene type D and a beaker of DI-water can be seen in the 50°C water bath. An additional DI-water beaker is at room temperature.

Al etching

The next step is the etching of a short segment of the Al shell. To protect the Al-shell, the chip is masked with a 450 nm thick layer of e-beam resist EL6 and baked for 5 mins at 185°C. A small window for the etchant to get in contact with the Al is opened by e-beam lithography and subsequent development. An illustrative design of the etch window is drawn in Fig. E1a. It contains a single pixel line perpendicular to the nanowire, ending in two micrometer-scale squares. We found that the big squares help giving more reproducible etching results.

Since there can be a thin layer of e-beam resist residing on the nanowire after the development, the chip is additionally treated in O₂ plasma for 60 s at 30 W to fully uncover the nanowire. Afterwards, the chip is post-baked again for 120 s at 125°C.

The actual Al etching process contains four steps and requires a beaker of Transene D at 50°C, a beaker of DI-water at 50°C, a beaker of DI-water at room temperature and a beaker of IPA at room temperature. The beakers for Transene D and DI-water are placed in a thermal water bath (Fig. E1b). We sequentially place the chip in the Transene D (18 s), DI-water at 50°C (20 s), DI-water at room temperature (40 s) and IPA (10 s) and shake it with moderate amplitude and frequency to etch the Al-shell. Finally, the chip is placed in acetone at 50°C for 30 mins to remove the e-beam mask. Occasionally, an additional 60 s O₂ plasma treatment is needed to free the chip fully from the resist mask.

Metallization

Depending on the experiment, the chip with resonator and nanowires could need additional metallization steps, for example, for contacting the nanowires to the microwave circuit.

Again, the chip is covered in a layer of e-beam resist. The structures to be metallized are patterned and developed in the e-beam resist. Before evaporating superconducting material on the epitaxial Al, the surface AlO_x is removed by Ar-milling. Material is then evaporated onto the chip at a pressure $\sim 2 \cdot 10^{-6}$ mbar. Finally, the chip is placed in acetone at 50°C for 30 mins to lift off the metal and e-beam resist. Now, the device chip is finalized and ready for wire-bonding.

9.2. Sample holder

Fig. E2 shows a photograph of the entire microwave sample holder. It consists of a two-layer printed circuit board (PCB) (a), a bottom copper plate and a top copper plate (b). The PCB, designed during the doctoral study, features DC connections and multiple microwave connections with the option of on-PCB bias tees in a compact size. We use Rogers 4350B as the PCB dielectric and electroless nickel immersion gold as plating. DC lines are connected via an Omnetics double row nano-D connector to the PCB (green hexagon). From the 25 pins, only 18 pins are routed onto the PCB due to limited space. Two customized connectors can be placed at the position indicated with white hexagons to short all the DC lines to the ground of the PCB. This feature prevents electrostatic discharge for sensitive electric devices during the sample transfer. One common practice in our lab is to have all the DC traces grounded when the device chip is wire-bonded to the PCB. The customized connectors have to be removed after mounting the sample to the cold finger and connecting the PCB ground to the ground of the dilution refrigerator. From the nano-D connector, the DC traces continue over several stages of surface mount devices (blue hexagon) to the chip area (black hexagon). To enable a compact design,

a large portion of the traces is routed onto the bottom layer using vias through the dielectric.

This PCB design allows up to eight RF connections, using Rosenberger surface mount mini-SMP 18S102-40ML5. The position of one of the RF connectors is indicated with a red hexagon. The RF connectors are placed as close as possible to the chip area with the aim to reduce standing waves along the traces. The RF traces on the PCB are designed in coplanar transmission line geometry. Simple electric circuits such as low- or high-pass filters and bias-tees can be built using surface mount components on the PCB at mixing chamber temperature.

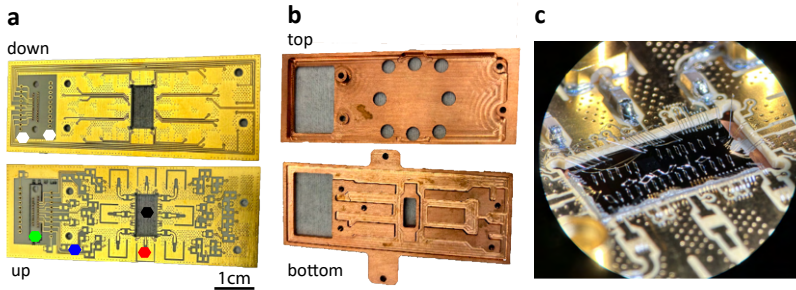


Figure E2. Sample holder for microwave measurement. **a**, A PCB as an interface between millimeter scale connectors and the device chip. **b**, Copper plates to enclose the PCB and device chip. **c**, A gatemon device chip wire-bonded to the PCB.

After tailoring the PCB with surface mount components, it can be mounted on the bottom copper plate by screws. Because a large portion of the device chip is a superconducting ground plane, slot-line modes can form with the bottom copper plate, which could create an additional loss channel. The coupling of the slot-line modes to quantum devices is reduced by removing a large portion of the copper below the chip. The chip can be glued into the chip area on the rest of the bottom copper plate, followed by wire-bonding. Fig. E2c presents an optical image of a gatemon chip bonded to the PCB. Finally, the top plate can be screwed onto the PCB such that the chip is surrounded by a normal metal shield.

9.3. Cryostat wiring

The two major experiments in this thesis were both conducted in the Bluefors cryostat. Small modifications were done between the two experiments.

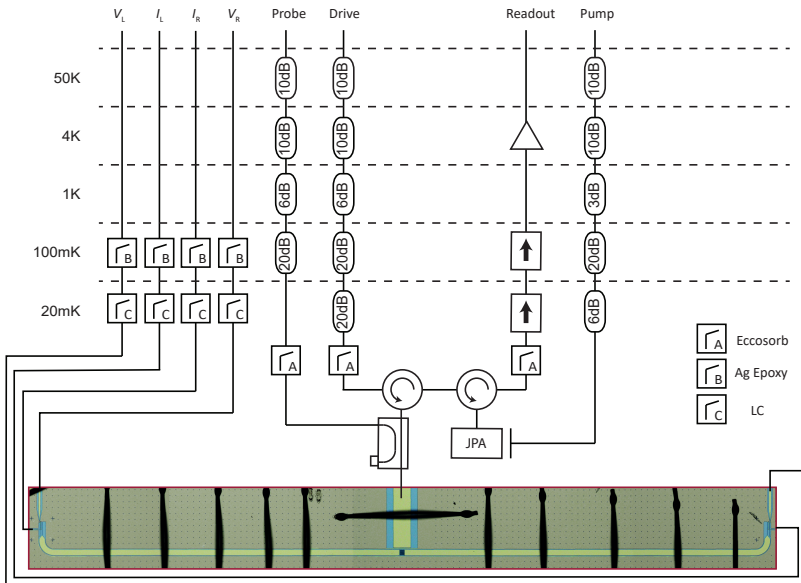


Figure E3. Wiring of the Bluefors for the Andreev qubit measurement.

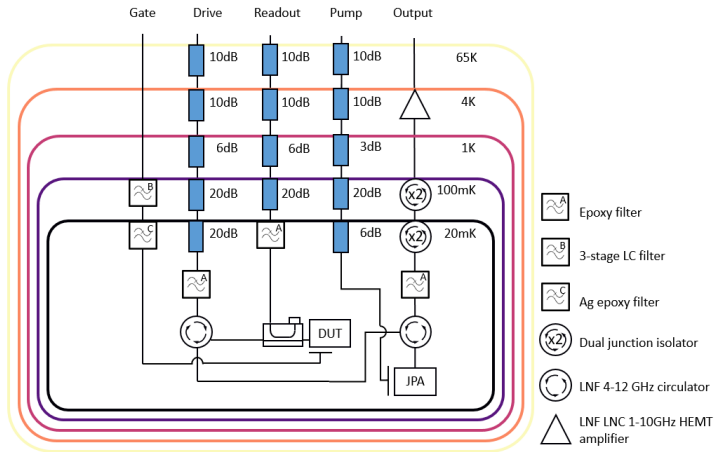


Figure E4. Wiring of the Bluefors for the gatemon qubit measurement.

Fig. E3 shows the wiring in the Bluefors for the Andreev qubit experiment. Both the qubit drive and resonator readout lines are filtered with home-made epoxy filters (3dB-cutoff frequency = 18 GHz) and heavily attenuated (~ 89 dB @ 6 GHz). The amplification chain consist of a Josephson parametric amplifier¹ (JPA), an epoxy filter and a dual junction isolator in the mixing chamber. It is followed by another dual junction isolator at the coldplate before it goes to the 4K HEMT amplifier. There are two additional RF gate lines not drawn in the schematic, each with an attenuation of 10 dB (50K) + 10 dB (4K) + 3 dB (still) + 10 dB (coldplate) + 3 dB (MC) = 36 dB.

The DC flux and gate lines are filtered with Ag epoxy filters at the coldplate and a 3-stage low-ohmic LC-filter box with cutoff frequency at 80 MHz, 225 MHz and 400 MHz at the mixing chamber. The DC and RF gate lines are combined on the PCB with an RC bias tee using 1 k Ω resistance and 2.2 nF capacitance.

The wiring is almost identical for the gatemon qubit experiment. However, the 3-stage LC filter box and the Ag epoxy filter box are exchanged, since having the Ag epoxy filter box at lower temperature can better cool down the DC lines and hence reduce the noise amplitude. The RC bias tee on the PCB now has 1 k Ω resistance and 30 nF capacitance.

To be sure that the sample holder and RF wiring in the cryostat are correct,

¹It is a dimer Josephson-junction-array amplifier developed in the group of Dr. Ioan Pop at the Karlsruhe institute of technology and fabricated by Carlo Ciaccia, a PhD student in the Nanoelectronics lab [111].

we measure the transmission of the RF lines from the top of the fridge to the sample holder at room temperature before the experiments. Fig. E5 shows the transmission spectrum of the RF gate and readout lines up to 20 GHz. Indeed, both lines are transmissive. The difference in transmission is determined by the attenuation added along the chain, with the readout line being more attenuated. For the readout line, the attenuation above 10.5 GHz is so heavy that it can not be measured. We observe dips in the transmission spectrum of the RF gate line with a spacing of 6.5 GHz, as indicated with the black arrows. We suspect that this feature arises from impedance mismatch between the capacitance of the bias tee and the RF connector or between the capacitance of the bias tee and the bondwire to the device. This feature is not observed for the readout line which also does not have a bias tee. Nevertheless, this extra attenuation at certain frequency range does not harm the measurement as it can be compensated with increased power at the signal generator.

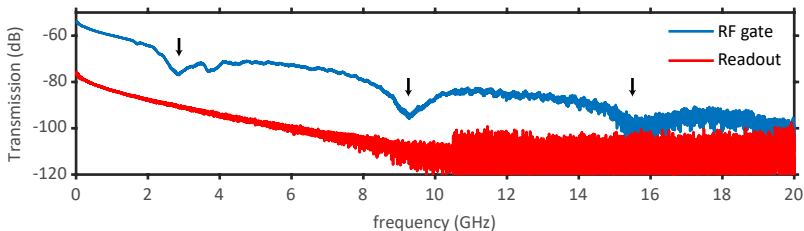


Figure E5. Room temperature transmission from the top of the cryostat to the sample holder.

9.4. Room temperature microwave setup

We have established two new room temperature microwave setups in the Nanoelectronics lab. The first setup is for standard qubit characterization with a large parameter space to program qubit drive and resonator readout pulses to fit the requirements for individual qubit experiments. A large set of parameters including pulse amplitude, phase, width, delay and shape can be modified in this setup using arbitrary waveform generation. The second setup, performing as chopped two-tone spectroscopy, is for microwave spectroscopy of excited states of a quantum device that are addressable through electromagnetic waves. Hereby, the parameters for the qubit drive pulse is only determined by a square modulation. Since the precise measurement of coherence properties is not the target in this setup, it is a fast and 'dirty' measurement that gives information about the excitation spectrum of a device up to

20 GHz. Both setups were developed with intensive scientific exchanges with Dr. Marcelo Goffman from the Quantronics group, CEA-Saclay.

Standard qubit characterization setup

Fig. E6 shows the room temperature setup for standard qubit measurement. The qubit control parameters for the presented experiments are usually gate voltage and flux current. In our lab, we use the Yokogawa 7651 as current source and the Basel SP 927 as voltage source, often with room temperature low-pass filters with a cut-off frequency of $f_{\text{cutoff}} \approx 100$ kHz. The JPA pump tone is provided by an Agilent N5183B signal generator. We use an Agilent E8257D vector signal generator in combination with an AWG 5014C arbitrary waveform generator (AWG) to execute qubit drive pulses. Moreover, we use the marker output of the AWG to trigger the Zurich instruments (ZI) SHFQA for resonator readout. Both the Agilent E8257D and ZI SHFQA are synchronised to the 10 MHz synchronisation output of the AWG.

The output of the ZI SHFQA is AC coupled to the device via a room temperature DC block. The resonator probe pulse sees, after passing through the amplification chain inside the fridge, a room temperature circulator, a high-Q tunable microwave bandpass filter and a room temperature amplifier before reaching the input of the ZI SHFQA. The JPA pump tone is a microwave signal with elevated power close to the resonance frequency ($f_{\text{pump}} - f_r \approx 150$ MHz), which also couples to the input of the SHFQA. In fact, we experienced a saturation of the analog-to-digital conversion range due to the pump tone. This can be minimized via the tunable bandpass filter that only allows transmission in a narrow band around f_r ². Reflected signals in the stopband, especially the pump tone at f_{pump} , are then terminated to the ground via the circulator.

Chopped two-tone spectroscopy

Fig. E7 shows the room temperature setup for chopped two-tone spectroscopy. Here, the drive tone is pulsed modulated with a fixed period, much longer than the characteristic time scales of the quantum device, with a 50% duty cycle. The pulse sequence is generated by the Stanford SG386 signal generator and fed in to the R&S SMB 100A signal generator, which then generates the pulse modulated drive pulse. Within one period, the quantum device is driven for 50% of the time, yielding a resonance frequency shift also for 50% of the time when an excited state transition is addressed.

A R&S vector network analyzer (VNA) generates a continuous-wave tone for the cavity readout, that splits into two paths. On one path, the signal travels to the LO port of a Marki IQ4509MXP IQ-mixer for the room temperature

²The high-Q tunable bandpass filter is a re-entrant cavity resonator designed and fabricated by the group of Dr. Ioan Pop at the Karlsruhe Institute of Technology.

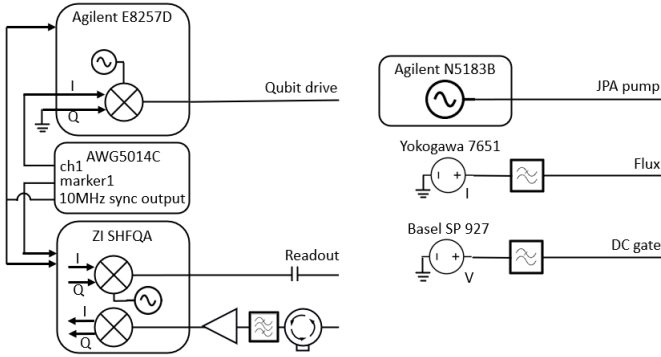


Figure E6. Room temperature microwave setup for standard qubit characterization measurement.

homodyne detection scheme. On the other path, the signal travels down to the resonator device, with a room temperature attenuator. The IQ -mixer requires a power of ~ 10 dBm on the LO port to operate, which usually means a large photon number on the resonator without additional attenuation. The reflected or transmitted readout pulse enters the RF port of the mixer and is down-converted to the base-band into the I- and Q-ports. We then use a ZI HF2LI to acquire the quadrature values of the readout pulse after several stages of low-pass filters and demodulate them at a frequency given by the inverse of the pulse modulation period, which then results in a signal when the resonance frequency is shifted. Both the ZI HF2LI and R&S SMB 100A are synchronised to the 10 MHz synchronisation output of the Stanford SG386.

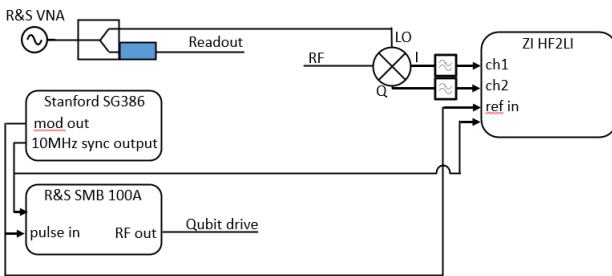


Figure E7. Room temperature microwave setup for chopped two-tone spectroscopy.

9.5. Qubit measurement protocol

A protocol with measurement scripts for characterization of superconducting qubits and Andreev qubits was developed during the doctoral study. In the following, we will explain the protocol step-by-step with exemplary measurements.

Single-tone spectroscopy

After the chip is cooled down to base temperature, almost no information is known about the device. To obtain a fast overview about the device, single tone measurement is performed either with the VNA or the SHFQA. If the resonance of the superconducting resonator is present, a narrow spectrum of typically a few tens of MHz is measured at the resonance frequency when sweeping the qubit control parameters, such as gates or magnetic field. A shift of the resonance frequency is observed when the qubit frequency approaches that of the resonator due to dispersive coupling. Hereby, the resonator excitation power has to be set at low values to remain in the few photon limit. A too high excitation power would restore the bare resonance. As an example, for an overcoupled resonator with a resonance frequency of 6.5 GHz and a total quality factor of 3000, a single photon is loaded with an excitation power of -143 dBm at the resonator. Observing avoided-crossing indicates a strongly coupled qubit-resonator system and a crossing of the qubit frequency with the resonance frequency. However, qubit characterization is usually not performed in this limit, but in the dispersive limit.

If spectroscopy measurement using the SHFQA is anticipated, simply creating an instance from the class *Continuous_spectroscopy* with corresponding input parameters prepares the SHFQA for the measurement. Explanation of the input parameters can be found in the package *qucs*.

Continuous two-tone spectroscopy

After observing a dispersive shift of the resonator, the qubit transition frequency as a function of the qubit control parameters should be measured. A continuous two-tone spectroscopy can be performed to solve this task. The qubit is driven continuously with variable drive frequencies using a signal generator while a second probe tone with fixed frequency is set close to the resonance frequency of the resonator and sent to the resonator. The second tone can be generated by a VNA. When the drive frequency matches the qubit frequency, the qubit is driven from the ground state yielding a shift of the resonator frequency. Hence, a change in the amplitude or phase of the probe tone is observed.

Here, the spectroscopy measurement can start at elevated drive power. This will broaden the linewidth of the qubit spectrum and hence make it more visible. Once the approximate qubit frequency is found, a detail measurement can be performed at lower drive power. The power for the probe tone should be kept in a few photon limit. High photon number shifts the qubit frequency yielding multiple qubit spectral lines.

Because the dispersive shift varies with the qubit-resonator frequency detuning, the optimal readout frequency changes at different operation points. Thus, the frequency of the resonator probe tone should be adjusted when sweeping the qubit control parameter. A good way to track the optimal readout frequency is to measure a single-tone spectrum after updating the qubit control parameter and to numerically find the resonance frequency. The VNA or SHFQA should then be updated with the new resonance frequency before performing the two-tone measurement. An example with probe frequency update for gate sweep can be found in the class *meta_gate*.

The goal of this step is to find a local maximum in the qubit spectrum that is $\sim 10g$ detuned from the resonance frequency, with g being the qubit-resonator coupling strength. This ensures a good suppression of spontaneous qubit decay into the resonator, which harms the qubit energy relaxation time T_1 , and simultaneously a sufficiently large dispersive shift for distinguishing the qubit excited state from the ground state.

Pulse design and upload

The next step is to design qubit drive pulse sequences for time domain measurement. In the simplest case, a drive pulse sequence is composed with one or multiple square pulses with variable pulse amplitude and width.

A time domain measurement is performed in unit of scans. Each scan is composed by a period of qubit manipulation and a period of resonator readout. If there is no scheme to actively reset the qubit to the ground state, the wait time of subsequent scans should be much longer than the energy relaxation time T_1 of the qubit such that it is relaxed to the ground state before a new qubit manipulation period starts. Although the T_1 is an unknown parameter at the beginning, realistic values can be estimated from literature.

The resonator readout is performed using the SHFQA that needs a trigger pulse for synchronisation. This trigger pulse can be provided for example by the marker 1 of the channel 1 of the AWG. A high value of 3.3 V and a duty cycle of 50% of the scan length will do the job. On the SHFQA, the threshold voltage shall be set to 1.65 V.

The python package *qkit.measure.timedomain.pulse_sequence* is used for designing individual pulses. First, pulse instances are created using the class *Pulse* with *pulse length*, *shape*, *name*, *amplitude* and *intermediate frequency* as input parameters. Second, these pulse instances are concatenated in a

pulse sequence instance that is created from the class *PulseSequence*. Third, the pulse sequence is prepared in form of an array, that it can be uploaded to the AWG. An array can be created by calling the pulses from the sequence instance using *sampling rate*, *heterodyne* and *start_phase* as input parameters. Single sideband upconversion can be performed by setting the corresponding *intermediate frequency* and *start_phase* and passing True to *heterodyne*. The so-created arrays shall then be concatenated into one pulse sequence array.

After that, a set of four ordering parameters need to be set for each pulse in the pulse sequence. They are *n_reps*, *trig_waits*, *jump_tos*, *go_to_states* determining the order which the sequence plays in. In most of the cases, *n_reps* is an array of one while *trig_waits* and *jump_tos* are both arrays of zero. *go_to_states* is an array of zero except for the last element which is one. This way, the drive sequence is played in repetition. Finally, the method *make_send_and_load_file* is applied together with the sequence arrays and ordering parameters to upload the drive sequence to the AWG.

The design of resonator readout pulse is simpler. By simply creating an instance from the class *Flat_top_gaussian_pulse_readout* from the package *qucs* with corresponding parameters, the SHFQA is prepared in a way such that a flat top Gaussian shaped readout pulse is stored in the first waveform memory in the channel 1. There are a lot of input parameters for a high design degree of freedom to fit the experimental requirements. Detail explanation of the input parameters are documented in the file *qucs.py*.

Before applying the drive pulse sequences to the VSG or device, they should be checked on an oscilloscope. The oscilloscope Keysight MSOX6004A with four input channels is fast enough to monitor the pulse sequences. Connect the outputs of the AWG to the oscilloscope. The oscilloscope input impedance should be set to $50\ \Omega$ to observe the actual voltage later seen by the inputs of the VSG or RF lines of the fridge. The oscilloscope measurement can be triggered at the rising slope of the marker pulse. Importantly, the peak-to-peak voltage of the drive sequence should not exceed 1 V as this is the maximum voltage that the wide-band IQ-inputs of the VSG can take. After confirming that the drive pulse sequences do not harm instruments or the device, the outputs of the AWG can be connected to the VSG or RF lines of the fridge.

Pulse alignment

Albeit careful design of the qubit drive and readout sequences, they are not aligned precisely due to different cable length and instrument latency times. Here, the alignment shall be performed using the oscilloscope again. Connect the outputs of the signal generators to the oscilloscope and estimate the misalignment using the marker feature of the oscilloscope. Typical misalignment can be as large as ~ 100 ns. Adjust the *probe_delay* parameter for the readout pulse to correct the misalignment.

Now, the room temperature calibration is completed and the microwave signal generators can be connected to the device.

Calibration of integration delay

The readout pulse travels within a certain time period from the output of the SHFQA to the input of it. This period of time, known as time-of-flight (TOF), is given by the ratio of the length of the transmission line and the signal propagation velocity in the transmission line. TOF can be measured using the scope feature of the SHFQA. Creating an instance from the class `Flat_top_gaussian_pulse_scope_trace` prepares the SHFQA to send out a flat top Gaussian readout pulse and to start the scope to record incident voltage as a function of time. The TOF is the time difference between the output of the readout pulse and the incident of it. It is typically ~ 330 ns in our setup.

When sending a readout pulse at the resonance frequency of a resonator, the transient behaviour of the resonator can be measured with the scope feature. The total quality factor Q of the resonator can be computed from the characteristic timescale τ of the resonator decay as $Q = \pi f_r \tau$ with f_r being the resonance frequency, after exciting the resonator with a pulse at exactly the resonance frequency.

For the rest of the characterization, a Josephson junction parametric amplifier (JPA) can be turned on to improve the signal-to-noise ratio. Usually, a signal voltage increase by a factor of ten can be achieved, see Fig. E8a. The finite rise time in the plot is an artefact created by the room temperature re-entrant cavity filter.

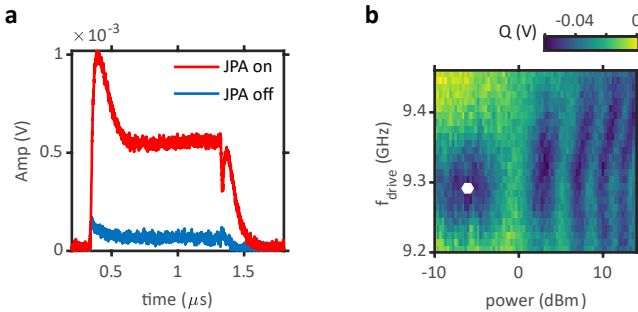


Figure E8. **a**, Transient measurement of a resonator response with and without Josephson parametric amplification. **b**, The change of the quadrature value Q of the readout pulse as a function for qubit drive power and frequency. Here the drive pulse width is 10 ns.

Calibration of the X_π -gate

Next, perform a pulsed two-tone spectroscopy by first exciting the qubit with a short drive pulse and subsequently measure the resonator response as a function of the drive frequency and drive power. Typical drive pulse length can be 10 ns long. A X_π -gate can be calibrated from this measurement. An example is plotted in Fig. E8b. In this measurement, one obtains five Rabi oscillations as a function of the drive power. The hexagon indicates the drive parameters for a X_π -gate.

The SHFQA can be set to mode *single* or *timedomain_differential*. While the former mode outputs one readout pulse that follows the qubit drive pulse immediately, the latter mode outputs a second readout pulse in addition that measures the qubit in the ground state. The mode *timedomain_differential* is useful as it directly shows the contrast between the qubit excited and ground state.

Optimization of readout power and frequency

With the knowledge of a short X_π -gate, the readout power and frequency can be optimized. Prepare the qubit in the excited state with the X_π -gate and measuring the resonator response in the *single* mode as a function of the readout power and frequency. The parameter set which gives the highest contrast can be used for the time domain measurement. The readout frequency of a readout pulse is the sum of a center frequency f_{center} and an intermediate frequency f_{IF} . The SHFQA is engineered in a way that multiple f_{IF} can be mixed to a center frequency, allowing multiplexed qubit readout. Fig. E9 shows a measurement of the quadrature values of the resonator response in the qubit excited (I_e, Q_e) and ground state (I_g, Q_g) as a function of f_{IF} . The readout power is set to -30 dBm at room temperature. From this measurement, one can derive that setting a $f_{\text{IF}} = 55.4$ MHz will enable a qubit state discrimination fully in the I -quadrature.

Rabi measurement

A proper Rabi oscillation measurement can be taken again with optimal readout parameters. Here, the oscillation shall be measured as a function of qubit drive frequency, drive power and drive pulse length.

Energy relaxation time measurement

Qubit energy relaxation can be measured by preparing the qubit in the excited state and delaying the readout pulse. The class *Probe_delay* creates a meta instrument that sweeps the starting time of the readout pulse. The characteristic relaxation time scale T_1 can be fitted from the data using an exponential

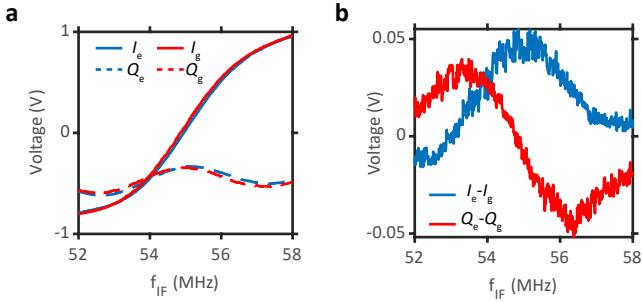


Figure E9. **a**, IQ quadrature values of the cavity readout pulse as a function of the intermediate frequency. Blue lines are measured after preparing the qubit in the excited state, red lines after relaxing to the ground state. **b**, Difference of the quadrature values.

fit. The parameter *intergration_time* for the readout pulse might need to be adjusted to be shorter than T_1 with the knowledge T_1 .

Coherence time measurement

Dephasing time of the qubit can be estimated from the decay of Ramsey fringes. Hereby, the qubit is prepared in the mixed state with a $X_{\pi/2}$ -gate. After a variable wait time τ , a second $X_{\pi/2}$ -gate is applied. As the wait time τ increases, the second $X_{\pi/2}$ -gate creates an oscillating pattern between the excited state and ground state if the drive frequency does not exactly matches the qubit frequency. The dephasing time T_2^* can be obtained from fitting the exponential decay of these oscillations. An additional refocusing X_π -gate can be applied between the two $X_{\pi/2}$ -gates to mitigate low frequency fluctuation of the qubit frequency, a technique known as Hahn-echo sequence.

10 Conclusion and outlook

The main goal of this thesis is the development of a long-range coupling scheme for two Andreev qubits. The two requirements for such an experiment are, on the one hand, reproducible highly transparent few-mode Josephson junction devices and, on the other hand, a high quality factor superconducting cavity coupler.

In Ch. 4, we have demonstrated our capability of fabricating InAs/Al nanowire Josephson junction (NWJJ) devices. An etching recipe using the Al etchant Transene D was established to form JJ on the length scale of a few hundreds of nanometers. The observation of multiple Andreev reflections (MARs) in these NW devices revealed transparent semiconductor-superconductor interfaces. Fitting the MAR pattern, we extracted the junction transparency and found highly transparent channels. This experiment showed the reproducible fabrication of highly transparent InAs/Al NWJJ which forms the base for encoding qubits in the Andreev spectrum.

For the second requirement, in Ch. 5, we proposed and studied a novel superconducting cavity coupler, which was designed to inductively couple to two quantum systems at distance. It was complementary to the well-established cavity coupler design for spin and superconducting qubits, which relied on the susceptibility of a qubit to voltage fluctuations [5, 6, 34, 93, 107, 143]. In our coupler design, the cavity induced coherent flux fluctuations at the two spatially separated qubits and established in this way a light-matter interaction on both sites. We identified that our initial coupling scheme, based on two spatially-separated current anti-nodes, resulted in an undesired ground-loop through the resonator which was detrimental to its internal quality factor due to low-frequency noise. In our experiment, we circumvented this negative effect by employing a capacitively coupled quarter-wavelength resonator pair, blocking low-frequency noise.

We verified the possibility to use the developed coupler for the readout and control of single Andreev qubits, benchmarking the performance of our InAs/Al NWJJ devices at the same time in Ch. 6. Using our cavity coupler, we could reveal Andreev transitions in both NWJJs and measure the energy relaxation and Rabi decay time for the Andreev pair transitions, reproducing consistent results with the literature [25, 56]. This set of experiments was built on the reproducible fabrication processes of the InAs/Al nanowire devices from

Ch. 4.

The main findings of this thesis were reported in Ch. 7, where the resonator pair was indeed operated as a coupler. We have demonstrated, for the first time, a coherent coupling of two spatially separated Andreev pair qubits. By aligning both qubit transition frequencies into the near-resonant or resonant regime of the two cavity modes, we have measured dispersing quantum states using microwave techniques, consistent with a three-sites Tavis-Cummings model that manifested long range hybridization of the Andreev pair qubits. All the studies in previous chapters have prepared and contributed to this keen demonstration, that now evidently extended the circuit quantum electrodynamics toolbox by a complementary cavity coupler circuit using the current, respectively the flux, degree of freedom. This encouraging discovery opens up new possibilities to investigate distant quantum entanglements of the systems that are exclusively susceptible to flux fluctuations.

Andreev qubit dephasing

Now, we would like to take a step back and discuss about the coherence of single Andreev qubits. So far, Andreev qubits have been shown on three platforms, namely the pair transitions in Al atomic point contacts ("Al weak-link"), the pair transitions in epitaxial InAs/Al NWJJs ("InAs pair") and the odd transitions in epitaxial InAs/Al NWJJs ("InAs spin"). In the latter platform, two kinds of Andreev spin qubits were demonstrated, formed either by two spin states in different Andreev manifolds, with a relaxation time $\sim 3 \mu\text{s}$, or in the same manifold. When regarding the same manifold, the relaxation time of a polarized spin could be as high as $T_s = 90 \mu\text{s}$, as measured in Ref. [38], highlighting the possibility of long coherence of an Andreev spin qubit. While semiconducting nanowires were a prosperous material platform due to their in-situ electrical tunability and physically hard confinement potentials, their performance as Andreev qubits were still limited by spin flips of nuclei in the semiconductor.

Fig. E1 summarizes the coherence time data from different Andreev qubit experiments. Fig. E1a presents the energy relaxation time T_1 , with the data point associated with a $T_s = 90 \mu\text{s}$ being omitted, Fig. E1b the dephasing time T_2^* , measured using Ramsey interferometry techniques, and Fig. E1c the Hahn-echo decay time T_{2E} across all three Andreev qubit platforms. The large discrepancy between the T_2^* , respectively T_{2E} , and T_1 for the column "InAs spin" signifies the hidden potential of an Andreev spin qubit. With the summary of coherence data from available Andreev qubit experiments, we hope to encourage new efforts to explore "clean" Andreev spin qubits, whose dephasing time is enhanced to the limit by the energy relaxation, $T_1 \approx 2T_2$ [89].

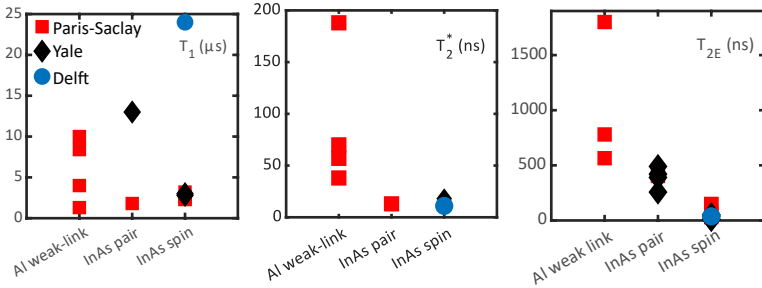


Figure E1. Quantum coherence data. **a**, Energy relaxation time T_1 plotted against the Andreev qubit platforms (The definition of platforms can be found in the main text). **b**, Dephasing time T_2^* . **c**, Hahn-echo decay time T_{2E} . Data for the "Al weak-link" column are extracted from Ref. [24], for the "InAs pair" column from Ref. [25, 36, 144], for the "InAs spin" column from Ref. [35, 36, 144]. From our experiment, a T_1 of $0.28 \mu\text{s}$ and $1.07 \mu\text{s}$ were measured for the column "InAs pair".

In the remaining scope of this thesis, we accomplished a first step towards a cleaner Andreev spin qubit by exploring Ge/Si core/shell nanowires as a Josephson weak link candidate. Because Ge/Si core/shell nanowires consist of type IV materials, they have a lower abundance of nuclei spin promising longer qubit dephasing. We have measured the energy relaxation and, for the first time, dephasing time of a superconducting gatemon qubit using a Ge/Si core/shell NWJJ. This experiment required substantial supercurrent in the Josephson element with increased mode numbers, which puts the operation of the NWJJ, with increased electrochemical potential, in the opposite regime of an Andreev qubit. Hence, a continuation of works could be integrating the Ge/Si core/shell nanowire devices as Andreev spin qubits and studying their quantum coherence. If an improvement of dephasing time is evident in these nanowires, one may proceed to a spin-spin entanglement experiment, using the here demonstrated superconducting cavity coupler scheme.

So far, the vertically grown nanowires, be it InAs/Al or Ge/Si core/shell nanowires, have to be transferred from the nanowire growth chip to the microwave device chip, which is obviously not a scalable procedure. Alternative group IV semiconductor platforms that allow a top-down fabrication could further be investigated, such as selective area grown Ge nanowires [145] or gate-defined weak links in strained Ge/GeSi quantum wells [146].

Despite the interesting findings of this thesis, Andreev qubits still remain a vastly unexplored terrain. To promote Andreev qubits as a serious competitor,

a demonstration of a large Rabi oscillation quality factor, that is defined as $Q = f_{\text{rabi}} T_2^*$, with f_{rabi} being the Rabi frequency and T_2^* the dephasing time, is persuasive.

Bibliography

- [1] M. A. Nielsen and I. L. Chuang, *Quantum Computation and Quantum Information: 10th Anniversary Edition* (Cambridge University Press, Cambridge, 2010).
- [2] D. P. DiVincenzo, *Fortschritte der Physik* **48**, 771 (2000).
- [3] J. R. Petta, A. C. Johnson, J. M. Taylor, E. A. Laird, A. Yacoby, M. D. Lukin, C. M. Marcus, M. P. Hanson, and A. C. Gossard, *Science* **309**, 2180 (2005).
- [4] Y. Nakamura, Y. A. Pashkin, and J. S. Tsai, *Nature* **398**, 786 (1999).
- [5] P. Harvey-Collard, J. Dijkema, G. Zheng, A. Sammak, G. Scappucci, and L. M. K. Vandersypen, *Phys. Rev. X* **12**, 021026 (2022).
- [6] J. Majer, J. M. Chow, J. M. Gambetta, J. Koch, B. R. Johnson, J. A. Schreier, L. Frunzio, D. I. Schuster, A. A. Houck, A. Wallraff, A. Blais, M. H. Devoret, S. M. Girvin, and R. J. Schoelkopf, *Nature* **449**, 443 (2007).
- [7] T. F. Watson, S. G. J. Philips, E. Kawakami, D. R. Ward, P. Scarlino, M. Veldhorst, D. E. Savage, M. G. Lagally, M. Friesen, S. N. Coppersmith, M. A. Eriksson, and L. M. K. Vandersypen, *Nature* **555**, 633 (2018).
- [8] L. DiCarlo, J. M. Chow, J. M. Gambetta, L. S. Bishop, B. R. Johnson, D. I. Schuster, J. Majer, A. Blais, L. Frunzio, S. M. Girvin, and R. J. Schoelkopf, *Nature* **460**, 240 (2009).
- [9] P. Stano and D. Loss, *Nature Reviews Physics* **4**, 672 (2022).
- [10] A. Chatterjee, P. Stevenson, S. De Franceschi, A. Morello, N. P. de Leon, and F. Kuemmeth, *Nature Reviews Physics* **3**, 157 (2021).
- [11] M. F. Gonzalez-Zalba, S. de Franceschi, E. Charbon, T. Meunier, M. Vinet, and A. S. Dzurak, *Nature Electronics* **4**, 872 (2021).
- [12] G. Scappucci, C. Kloeffel, F. A. Zwanenburg, D. Loss, M. Myronov, J.-J. Zhang, S. De Franceschi, G. Katsaros, and M. Veldhorst, *Nature Reviews Materials* **6**, 926 (2021).
- [13] L. M. K. Vandersypen and M. A. Eriksson, *Physics Today* **72**, 38 (2019).
- [14] I. Siddiqi, *Nature Reviews Materials* **6**, 875 (2021).
- [15] M. Kjaergaard, M. E. Schwartz, J. Braumüller, P. Krantz, J. I.-J. Wang, S. Gustavsson, and W. D. Oliver, *Annual Review of Condensed Matter Physics* **11**, 369 (2020).

- [16] J. Clarke and F. K. Wilhelm, *Nature* **453**, 1031 (2008).
- [17] P. Krantz, M. Kjaergaard, F. Yan, T. P. Orlando, S. Gustavsson, and W. D. Oliver, *Applied Physics Reviews* **6**, 021318 (2019).
- [18] J. Yoneda, K. Takeda, T. Otsuka, T. Nakajima, M. R. Delbecq, G. Allison, T. Honda, T. Kodera, S. Oda, Y. Hoshi, N. Usami, K. M. Itoh, and S. Tarucha, *Nature Nanotechnology* **13**, 102 (2018).
- [19] R. Zhao, T. Tantt, K. Y. Tan, B. Hensen, K. W. Chan, J. C. C. Hwang, R. C. C. Leon, C. H. Yang, W. Gilbert, F. E. Hudson, K. M. Itoh, A. A. Kiselev, T. D. Ladd, A. Morello, A. Laucht, and A. S. Dzurak, *Nature Communications* **10**, 5500 (2019).
- [20] A. P. M. Place, L. V. H. Rodgers, P. Mundada, B. M. Smitham, M. Fitzpatrick, Z. Leng, A. Premkumar, J. Bryon, A. Vrajitoarea, S. Sussman, G. Cheng, T. Madhavan, H. K. Babla, X. H. Le, Y. Gang, B. Jäck, A. Gyenis, N. Yao, R. J. Cava, N. P. de Leon, and A. A. Houck, *Nature Communications* **12**, 1779 (2021).
- [21] C. Wang, X. Li, H. Xu, Z. Li, J. Wang, Z. Yang, Z. Mi, X. Liang, T. Su, C. Yang, G. Wang, W. Wang, Y. Li, M. Chen, C. Li, K. Linghu, J. Han, Y. Zhang, Y. Feng, Y. Song, T. Ma, J. Zhang, R. Wang, P. Zhao, W. Liu, G. Xue, Y. Jin, and H. Yu, *npj Quantum Information* **8**, 3 (2022).
- [22] A. F. Andreev, *Zh. Eksperim. i Teor. Fiz.* **46** (1964).
- [23] A. F. Andreev, *Zhurnal Eksperimental'noi i Teoreticheskoi Fiziki (U.S.S.R.)* For English translation see *Sov. Phys. - JETP (Engl. Transl.)* **49** (1965).
- [24] C. Janvier, L. Tosi, L. Bretheau, Ç. Ö. Girit, M. Stern, P. Bertet, P. Joyez, D. Vion, D. Esteve, M. F. Goffman, H. Pothier, and C. Urbina, *Science* **349**, 1199 (2015), <https://www.science.org/doi/pdf/10.1126/science.aab2179> .
- [25] M. Hays, G. de Lange, K. Serniak, D. J. van Woerkom, D. Bouman, P. Krogstrup, J. Nygård, A. Geresdi, and M. H. Devoret, *Phys. Rev. Lett.* **121**, 047001 (2018).
- [26] P. Zellekens, R. S. Deacon, P. Perla, D. Grützmacher, M. I. Lepsa, T. Schäpers, and K. Ishibashi, *Communications Physics* **5**, 267 (2022).
- [27] M. Hays, V. Fatemi, D. Bouman, J. Cerrillo, S. Diamond, K. Serniak, T. Connolly, P. Krogstrup, J. Nygård, A. L. Yeyati, A. Geresdi, and M. H. Devoret, *Science* **373**, 430 (2021).
- [28] A. Zazunov, V. S. Shumeiko, E. N. Bratus', J. Lantz, and G. Wendin, *Phys. Rev. Lett.* **90**, 087003 (2003).
- [29] S. Park and A. L. Yeyati, *Phys. Rev. B* **96**, 125416 (2017).
- [30] Q. Zhi-Jie, H. Dong-Sheng, and X. Shi-Jie, *Chinese Physics Letters* **21**, 934 (2004).

-
- [31] J. Cerrillo, M. Hays, V. Fatemi, and A. L. Yeyati, *Phys. Rev. Res.* **3**, L022012 (2021).
- [32] J. Michelsen, V. S. Shumeiko, and G. Wendin, *Phys. Rev. B* **77**, 184506 (2008).
- [33] R. Aguado, *Applied Physics Letters* **117**, 240501 (2020).
- [34] M. A. Sillanpää, J. I. Park, and R. W. Simmonds, *Nature* **449**, 438 (2007).
- [35] M. Pita-Vidal, A. Bargerbos, R. Žitko, L. J. Splitthoff, L. Grünhaupt, J. J. Wesdorp, Y. Liu, L. P. Kouwenhoven, R. Aguado, B. van Heck, A. Kou, and C. K. Andersen, “Direct manipulation of a superconducting spin qubit strongly coupled to a transmon qubit,” (2022).
- [36] C. Metzger, *Effets de spin et de charge dans les états liés d’Andreev*, Theses, Université Paris-Saclay (2022).
- [37] B. Pannetier and H. Courtois, *Journal of Low Temperature Physics* **118**, 599 (2000).
- [38] M. Hays, V. Fatemi, K. Serniak, D. Bouman, S. Diamond, G. de Lange, P. Krogstrup, J. Nygård, A. Geresdi, and M. H. Devoret, *Nature Physics* **16**, 1103 (2020).
- [39] C. W. J. Beenakker and H. van Houten, *Phys. Rev. Lett.* **66**, 3056 (1991).
- [40] P. F. Bagwell, *Phys. Rev. B* **46**, 12573 (1992).
- [41] G. Dresselhaus, *Phys. Rev.* **100**, 580 (1955).
- [42] G. Bihlmayer, O. Rader, and R. Winkler, *New Journal of Physics* **17**, 050202 (2015).
- [43] P. Krogstrup, N. L. B. Ziino, W. Chang, S. M. Albrecht, M. H. Madsen, E. Johnson, J. Nygård, C. M. Marcus, and T. S. Jespersen, *Nature Materials* **14**, 400 (2015).
- [44] W. Chang, S. M. Albrecht, T. S. Jespersen, F. Kuemmeth, P. Krogstrup, J. Nygård, and C. M. Marcus, *Nature Nanotechnology* **10**, 232 (2015).
- [45] T. W. Larsen, K. D. Petersson, F. Kuemmeth, T. S. Jespersen, P. Krogstrup, J. Nygård, and C. M. Marcus, *Phys. Rev. Lett.* **115**, 127001 (2015).
- [46] M. T. Deng, S. Vaitiekėnas, E. B. Hansen, J. Danon, M. Leijnse, K. Flensberg, J. Nygård, P. Krogstrup, and C. M. Marcus, *Science* **354**, 1557 (2016).
- [47] S. M. Albrecht, A. P. Higginbotham, M. Madsen, F. Kuemmeth, T. S. Jespersen, J. Nygård, P. Krogstrup, and C. M. Marcus, *Nature* **531**, 206 (2016).
- [48] E. M. Spanton, M. Deng, S. Vaitiekėnas, P. Krogstrup, J. Nygård, C. M. Marcus, and K. A. Moler, *Nature Physics* **13**, 1177 (2017).
- [49] A. Blais, A. L. Grimsmo, S. M. Girvin, and A. Wallraff, *Rev. Mod. Phys.* **93**, 025005 (2021).

- [50] M. H. Devoret and R. J. Schoelkopf, *Science* **339**, 1169 (2013), <https://www.science.org/doi/pdf/10.1126/science.1231930> .
- [51] P. Krantz, M. Kjaergaard, F. Yan, T. P. Orlando, S. Gustavsson, and W. D. Oliver, *Applied Physics Reviews* **6**, 021318 (2019), <https://doi.org/10.1063/1.5089550> .
- [52] M. Kjaergaard, M. E. Schwartz, J. Braumüller, P. Krantz, J. I.-J. Wang, S. Gustavsson, and W. D. Oliver, *Annual Review of Condensed Matter Physics* **11**, 369 (2020), <https://doi.org/10.1146/annurev-conmatphys-031119050605> .
- [53] A. A. Clerk, K. W. Lehnert, P. Bertet, J. R. Petta, and Y. Nakamura, *Nature Physics* **16**, 257 (2020).
- [54] Z.-L. Xiang, S. Ashhab, J. Q. You, and F. Nori, *Rev. Mod. Phys.* **85**, 623 (2013).
- [55] F. J. Matute-Cañadas, C. Metzger, S. Park, L. Tosi, P. Krogstrup, J. Nygård, M. F. Goffman, C. Urbina, H. Pothier, and A. L. Yeyati, *Phys. Rev. Lett.* **128**, 197702 (2022).
- [56] L. Tosi, C. Metzger, M. F. Goffman, C. Urbina, H. Pothier, S. Park, A. L. Yeyati, J. Nygård, and P. Krogstrup, *Phys. Rev. X* **9**, 011010 (2019).
- [57] J. J. Wesdorp, F. J. Matute-Cañadas, A. Vaartjes, L. Grünhaupt, T. Laeven, S. Roelofs, L. J. Splitthoff, M. Pita-Vidal, A. Bargerboos, D. J. van Woerkom, P. Krogstrup, L. P. Kouwenhoven, C. K. Andersen, A. L. Yeyati, B. van Heck, and G. de Lange, “Microwave spectroscopy of interacting andreev spins,” (2022).
- [58] U. Vool and M. Devoret, *International Journal of Circuit Theory and Applications* **45**, 897 (2017), <https://onlinelibrary.wiley.com/doi/pdf/10.1002/cta.2359> .
- [59] A. Hertel, *Development of superconducting gatemon qubits based on selective-area-grown semiconductors*, Ph.D. thesis, University of Copenhagen (2021).
- [60] S. Probst, F. B. Song, P. A. Bushev, A. V. Ustinov, and M. Weides, *Review of Scientific Instruments* **86**, 024706 (2015), <https://doi.org/10.1063/1.4907935> .
- [61] J. Burnett, A. Bengtsson, D. Niepce, and J. Bylander, *Journal of Physics: Conference Series* **969**, 012131 (2018).
- [62] B. S. Deaver and W. M. Fairbank, *Phys. Rev. Lett.* **7**, 43 (1961).
- [63] R. Doll and M. Näbauer, *Phys. Rev. Lett.* **7**, 51 (1961).
- [64] R. Haller, *Probing the microwave response of novel Josephson elements*, Ph.D. thesis, University of Basel (2021).
- [65] D. J. van Woerkom, A. Proutski, B. van Heck, D. Bouman, J. I. Väyrynen, L. I. Glazman, P. Krogstrup, J. Nygård, L. P. Kouwenhoven, and A. Geresdi, *Nature Physics* **13**, 876 (2017).

- [66] A. I. Braginski and J. Clarke, “Introduction,” in *The SQUID Handbook* (John Wiley & Sons, Ltd, 2004) Chap. 1, pp. 1–28, <https://onlinelibrary.wiley.com/doi/pdf/10.1002/3527603646.ch1> .
- [67] S. Park, C. Metzger, L. Tosi, M. F. Goffman, C. Urbina, H. Pothier, and A. L. Yeyati, *Phys. Rev. Lett.* **125**, 077701 (2020).
- [68] A. Wallraff, D. I. Schuster, A. Blais, L. Frunzio, R.-. S. Huang, J. Majer, S. Kumar, S. M. Girvin, and R. J. Schoelkopf, *Nature* **431**, 162 (2004).
- [69] E. Jaynes and F. Cummings, *Proceedings of the IEEE* **51**, 89 (1963).
- [70] S. Stenholm, *Journal of Physics B: Atomic, Molecular and Optical Physics* **46**, 224013 (2013).
- [71] M. F. Goffman, C. Urbina, H. Pothier, J. Nygård, C. M. Marcus, and P. Krogstrup, *New Journal of Physics* **19**, 092002 (2017).
- [72] G. Fabian, *Engineered Magnetoconductance in InAs Nanowire Quantum Dots*, Ph.D. thesis, University of Basel (2015).
- [73] J. Gramich, *Andreev and Spin Transport in Carbon Nanotube Quantum Dot Hybrid Devices*, Ph.D. thesis, University of Basel (2016).
- [74] G. Abulizi, *Quantum transport in hexagonal boron nitride carbon nanotube heterostructures*, Ph.D. thesis, University of Basel (2017).
- [75] C. H. Jünger, *Transport Spectroscopy of Semiconductor Superconductor Nanowire Hybrid Devices*, Ph.D. thesis, University of Basel (2019).
- [76] F. S. Thomas, *Deterministic Tunnel Barriers in One-Dimensional Quantum Electronic Systems*, Ph.D. thesis, University of Basel (2020).
- [77] A. Bordoloi, *Spin Projection and Correlation Experiments in Nanoelectronic Devices*, Ph.D. thesis, University of Basel (2020).
- [78] B. Josephson, *Advances in Physics* **14**, 419 (1965), <https://doi.org/10.1080/00018736500101091> .
- [79] V. Ambegaokar and B. I. Halperin, *Phys. Rev. Lett.* **22**, 1364 (1969).
- [80] M. Tinkham, *Introduction to Superconductivity*, 2nd ed. (Dover Publications, 2004).
- [81] N. A. Court, A. J. Ferguson, and R. G. Clark, *Superconductor Science and Technology* **21**, 015013 (2007).
- [82] J. Ridderbos, M. Brauns, A. Li, E. P. A. M. Bakkers, A. Brinkman, W. G. van der Wiel, and F. A. Zwanenburg, *Phys. Rev. Materials* **3**, 084803 (2019).
- [83] H. A. Nilsson, P. Samuelsson, P. Caroff, and H. Q. Xu, *Nano Letters* **12**, 228 (2012).
- [84] D. Averin and A. Bardas, *Phys. Rev. Lett.* **75**, 1831 (1995).

- [85] J. C. Cuevas, A. Martín-Rodero, and A. L. Yeyati, *Phys. Rev. B* **54**, 7366 (1996).
- [86] V. S. Shumeiko, E. N. Bratus, and G. Wendin, *Low Temperature Physics* **23**, 181 (1997).
- [87] G. Rubio-Bollinger, “Aevshow v0.2,” .
- [88] A. Anthore, H. Pothier, and D. Esteve, *Phys. Rev. Lett.* **90**, 127001 (2003).
- [89] G. Ithier, E. Collin, P. Joyez, P. J. Meeson, D. Vion, D. Esteve, F. Chiarello, A. Shnirman, Y. Makhlin, J. Schrieffer, and G. Schön, *Phys. Rev. B* **72**, 134519 (2005).
- [90] A. A. Houck, J. A. Schreier, B. R. Johnson, J. M. Chow, J. Koch, J. M. Gambetta, D. I. Schuster, L. Frunzio, M. H. Devoret, S. M. Girvin, and R. J. Schoelkopf, *Phys. Rev. Lett.* **101**, 080502 (2008).
- [91] J. M. Gambetta, A. A. Houck, and A. Blais, *Phys. Rev. Lett.* **106**, 030502 (2011).
- [92] J. Majer, J. Chow, J. M. Gambetta, J. Koch, B. R. Johnson, J. A. Schreier, L. Frunzio, D. I. Schuster, A. A. Houck, A. Wallraff, A. Blais, M. H. Devoret, S. M. Girvin, and R. J. Schoelkopf, *Nature* **449**, 443 (2007), <https://www.nature.com/articles/nature06184.pdf> .
- [93] F. Borjans, X. G. Croot, X. Mi, M. J. Gullans, and J. R. Petta, *Nature* **577**, 195 (2020).
- [94] M. Tavis and F. W. Cummings, *Phys. Rev.* **170**, 379 (1968).
- [95] I. Kulik, *Sov. Phys. JETP* **30**, 944 (1970).
- [96] C. Jünger, S. Lehmann, K. A. Dick, C. Thelander, C. Schönenberger, and A. Baumgartner, “Intermediate states in andreev bound state fusion,” (2021), [arXiv:2111.00651 \[cond-mat.mes-hall\]](https://arxiv.org/abs/2111.00651) .
- [97] C. Jünger, A. Baumgartner, R. Delagrèe, D. Chevallier, S. Lehmann, M. Nilsson, K. A. Dick, C. Thelander, and C. Schönenberger, *Communications Physics* **2**, 76 (2019).
- [98] I. Kulik, *Soviet Journal of Experimental and Theoretical Physics* **30**, 944 (1969).
- [99] A. Furusaki and M. Tsukada, *Phys. Rev. B* **43**, 10164 (1991).
- [100] A. Furusaki, *Superlattices and Microstructures* **25**, 809 (1999).
- [101] J. Koch, T. M. Yu, J. Gambetta, A. A. Houck, D. I. Schuster, J. Majer, A. Blais, M. H. Devoret, S. M. Girvin, and R. J. Schoelkopf, *Phys. Rev. A* **76**, 042319 (2007).

- [102] M. McEwen, D. Kafri, Z. Chen, J. Atalaya, K. J. Satzinger, C. Quintana, P. V. Klimov, D. Sank, C. Gidney, A. G. Fowler, F. Arute, K. Arya, B. Buckley, B. Burkett, N. Bushnell, B. Chiaro, R. Collins, S. Demura, A. Dunsworth, C. Erickson, B. Foxen, M. Giustina, T. Huang, S. Hong, E. Jeffrey, S. Kim, K. Kechedzhi, F. Kostritsa, P. Laptev, A. Megrant, X. Mi, J. Mutus, O. Naaman, M. Neeley, C. Neill, M. Niu, A. Paler, N. Redd, P. Roushan, T. C. White, J. Yao, P. Yeh, A. Zalcman, Y. Chen, V. N. Smelyanskiy, J. M. Martinis, H. Neven, J. Kelly, A. N. Korotkov, A. G. Petukhov, and R. Barends, *Nature Communications* **12**, 1761 (2021).
- [103] M. Werninghaus, D. J. Egger, F. Roy, S. Machnes, F. K. Wilhelm, and S. Filipp, *npj Quantum Information* **7**, 14 (2021).
- [104] Z. Su, A. B. Tacla, M. Hocevar, D. Car, S. R. Plissard, E. P. A. M. Bakkers, A. J. Daley, D. Pekker, and S. M. Frolov, *Nature Communications* **8**, 585 (2017).
- [105] O. Kürtössy, Z. Scherübl, G. Fülöp, I. E. Lukács, T. Kanne, J. Nygård, P. Makk, and S. Csonka, *Nano Letters* **21**, 7929 (2021).
- [106] M. Pita-Vidal, J. J. Wesdorp, L. J. Splitthoff, A. Bargerbos, Y. Liu, L. P. Kouwenhoven, and C. K. Andersen, “Strong tunable coupling between two distant superconducting spin qubits,” (2023), [arXiv:2307.15654 \[quant-ph\]](https://arxiv.org/abs/2307.15654).
- [107] D. J. van Woerkom, P. Scarlino, J. H. Ungerer, C. Müller, J. V. Koski, A. J. Landig, C. Reichl, W. Wegscheider, T. Ihn, K. Ensslin, and A. Wallraff, *Phys. Rev. X* **8**, 041018 (2018).
- [108] C. Metzger, S. Park, L. Tosi, C. Janvier, A. A. Reynoso, M. F. Goffman, C. Urbina, A. Levy Yeyati, and H. Pothier, *Phys. Rev. Res.* **3**, 013036 (2021).
- [109] M. Hays, V. Fatemi, K. Serniak, D. Bouman, S. Diamond, G. de Lange, P. Krogstrup, J. Nygård, A. Geresdi, and M. H. Devoret, *Nature Physics* **16**, 1103 (2020), <https://www.nature.com/articles/s41567-020-0952-3.pdf>.
- [110] P. D. Kurilovich, V. D. Kurilovich, V. Fatemi, M. H. Devoret, and L. I. Glazman, *Phys. Rev. B* **104**, 174517 (2021).
- [111] P. Winkel, I. Takmakov, D. Rieger, L. Planat, W. Hasch-Guichard, L. Grünhaupt, N. Maleeva, F. Foroughi, F. Henriques, K. Borisov, J. Ferrero, A. V. Ustinov, W. Wernsdorfer, N. Roch, and I. M. Pop, *Phys. Rev. Appl.* **13**, 024015 (2020).
- [112] J. M. Fink, R. Bianchetti, M. Baur, M. Göppl, L. Steffen, S. Filipp, P. J. Leek, A. Blais, and A. Wallraff, *Phys. Rev. Lett.* **103**, 083601 (2009).
- [113] F. H. L. Koppens, K. C. Nowack, and L. M. K. Vandersypen, *Phys. Rev. Lett.* **100**, 236802 (2008).
- [114] B. M. Maune, M. G. Borselli, B. Huang, T. D. Ladd, P. W. Deelman, K. S. Holabird, A. A. Kiselev, I. Alvarado-Rodriguez, R. S. Ross, A. E. Schmitz, M. Sokolich, C. A. Watson, M. F. Gyure, and A. T. Hunter, *Nature* **481**, 344 (2012).

- [115] C. Kloeffel, M. Trif, and D. Loss, *Phys. Rev. B* **84**, 195314 (2011).
- [116] C. Kloeffel, M. J. Rančić, and D. Loss, *Phys. Rev. B* **97**, 235422 (2018).
- [117] S. Conesa-Boj, A. Li, S. Koelling, M. Brauns, J. Ridderbos, T. T. Nguyen, M. A. Verheijen, P. M. Koenraad, F. A. Zwanenburg, and E. P. A. M. Bakkers, *Nano Letters* **17**, 2259 (2017).
- [118] A. Vesti, *Fabrication and Electrical Characterization of Semiconductor Nanowire Devices*, Ph.D. thesis, University of Copenhagen (2016).
- [119] F. N. M. Froning, L. C. Camenzind, O. A. H. van der Molen, A. Li, E. P. A. M. Bakkers, D. M. Zumbühl, and F. R. Braakman, *Nature Nanotechnology* **16**, 308 (2021).
- [120] F. N. M. Froning, M. J. Rančić, B. Hetényi, S. Bosco, M. K. Rehmann, A. Li, E. P. A. M. Bakkers, F. A. Zwanenburg, D. Loss, D. M. Zumbühl, and F. R. Braakman, *Phys. Rev. Res.* **3**, 013081 (2021).
- [121] J. Ridderbos, M. Brauns, F. K. de Vries, J. Shen, A. Li, S. Kölling, M. A. Verheijen, A. Brinkman, W. G. van der Wiel, E. P. A. M. Bakkers, and F. A. Zwanenburg, *Nano Letters* **20**, 122 (2020).
- [122] J. Ridderbos, M. Brauns, J. Shen, F. K. de Vries, A. Li, E. P. A. M. Bakkers, A. Brinkman, and F. A. Zwanenburg, *Advanced Materials* **30**, 1802257 (2018), <https://onlinelibrary.wiley.com/doi/pdf/10.1002/adma.201802257>.
- [123] M. Sistani, J. Delaforce, R. B. G. Kramer, N. Roch, M. A. Luong, M. I. den Hertog, E. Robin, J. Smoliner, J. Yao, C. M. Lieber, C. Naud, A. Lugstein, and O. Buisson, *ACS Nano* **13**, 14145 (2019).
- [124] G. de Lange, B. van Heck, A. Bruno, D. J. van Woerkom, A. Geresdi, S. R. Plissard, E. P. A. M. Bakkers, A. R. Akhmerov, and L. DiCarlo, *Phys. Rev. Lett.* **115**, 127002 (2015).
- [125] M. Naghiloo, “Introduction to experimental quantum measurement with superconducting qubits,” (2019).
- [126] J. M. Martinis, *npj Quantum Information* **7**, 90 (2021).
- [127] S. De Franceschi, L. Kouwenhoven, C. Schönenberger, and W. Wernsdorfer, *Nature Nanotechnology* **5**, 703 (2010).
- [128] J. Claudon, F. Balestro, F. W. J. Hekking, and O. Buisson, *Phys. Rev. Lett.* **93**, 187003 (2004).
- [129] S. K. Dutta, F. W. Strauch, R. M. Lewis, K. Mitra, H. Paik, T. A. Palomaki, E. Tiesinga, J. R. Anderson, A. J. Dragt, C. J. Lobb, and F. C. Wellstood, *Phys. Rev. B* **78**, 104510 (2008).
- [130] Y. Schön, J. N. Voss, M. Wildermuth, A. Schneider, S. T. Skacel, M. P. Weides, J. H. Cole, H. Rotzinger, and A. V. Ustinov, *npj Quantum Materials* **5**, 18 (2020).

- [131] A. Antony, M. V. Gustafsson, G. J. Ribeill, M. Ware, A. Rajendran, L. C. G. Govia, T. A. Ohki, T. Taniguchi, K. Watanabe, J. Hone, and K. C. Fong, *Nano Letters* **21**, 10122 (2021).
- [132] J. I.-J. Wang, D. Rodan-Legrain, L. Bretheau, D. L. Campbell, B. Kannan, D. Kim, M. Kjaergaard, P. Krantz, G. O. Samach, F. Yan, J. L. Yoder, K. Watanabe, T. Taniguchi, T. P. Orlando, S. Gustavsson, P. Jarillo-Herrero, and W. D. Oliver, *Nature Nanotechnology* **14**, 120 (2019).
- [133] D. Sabonis, O. Erlandsson, A. Kringhøj, B. van Heck, T. W. Larsen, I. Petkovic, P. Krogstrup, K. D. Petersson, and C. M. Marcus, *Phys. Rev. Lett.* **125**, 156804 (2020).
- [134] O. Erlandsson, D. Sabonis, A. Kringhøj, T. W. Larsen, P. Krogstrup, K. D. Petersson, and C. M. Marcus, “Parity switching in a full-shell superconductor-semiconductor nanowire qubit,” (2022).
- [135] D. Ristè, C. C. Bultink, M. J. Tiggelman, R. N. Schouten, K. W. Lehnert, and L. DiCarlo, *Nature Communications* **4**, 1913 (2013).
- [136] Z. Lyu, E. Zhuo, X. Sun, A. Li, B. Li, Z. Ji, J. Fan, E. Bakkers, X. Han, X. Song, F. Qu, G. Liu, J. Shen, and L. Lu, “Hole-type superconducting gatemon qubit based on ge/si core/shell nanowires,” (2022).
- [137] F. H. L. Koppens, C. Buizert, K. J. Tielrooij, I. T. Vink, K. C. Nowack, T. Meunier, L. P. Kouwenhoven, and L. M. K. Vandersypen, *Nature* **442**, 766 (2006).
- [138] S. Nadj-Perge, S. M. Frolov, E. P. A. M. Bakkers, and L. P. Kouwenhoven, *Nature* **468**, 1084 (2010).
- [139] J. W. G. van den Berg, S. Nadj-Perge, V. S. Pribiag, S. R. Plissard, E. P. A. M. Bakkers, S. M. Frolov, and L. P. Kouwenhoven, *Phys. Rev. Lett.* **110**, 066806 (2013).
- [140] X. Wu, D. R. Ward, J. R. Prance, D. Kim, J. K. Gamble, R. T. Mohr, Z. Shi, D. E. Savage, M. G. Lagally, M. Friesen, S. N. Coppersmith, and M. A. Eriksson, *Proceedings of the National Academy of Sciences* **111**, 11938 (2014), <https://www.pnas.org/doi/pdf/10.1073/pnas.1412230111> .
- [141] E. Kawakami, P. Scarlino, D. R. Ward, F. R. Braakman, D. E. Savage, M. G. Lagally, M. Friesen, S. N. Coppersmith, M. A. Eriksson, and L. M. K. Vandersypen, *Nature Nanotechnology* **9**, 666 (2014).
- [142] J. H. Ungerer, D. Sarmah, A. Kononov, J. Ridderbos, R. Haller, L. Y. Cheung, and C. Schönberger, “Performance of high impedance resonators in dirty dielectric environments,” (2023).
- [143] A. J. Landig, J. V. Koski, P. Scarlino, C. Müller, J. C. Abadillo-Uriel, B. Kratochwil, C. Reichl, W. Wegscheider, S. N. Coppersmith, M. Friesen, A. Wallraff, T. Ihn, and K. Ensslin, *Nature Communications* **10**, 5037 (2019).
- [144] H. Max, *Realizing an Andreev Spin Qubit*, *Theses*, Yale University (2022).

- [145] S. P. Ramanandan, P. Tomić, N. P. Morgan, A. Giunto, A. Rudra, K. Ensslin, T. Ihn, and A. Fontcuberta i Morral, *Nano Letters* **22**, 4269 (2022).
- [146] D. Jirovec, A. Hofmann, A. Ballabio, P. M. Mutter, G. Tavani, M. Botifoll, A. Crippa, J. Kukucka, O. Sagi, F. Martins, J. Saez-Mollejo, I. Prieto, M. Borovkov, J. Arbiol, D. Chrastina, G. Isella, and G. Katsaros, *Nature Materials* **20**, 1106 (2021).
- [147] C. Jünger, S. Lehmann, K. A. Dick, C. Thelander, C. Schönenberger, and A. Baumgartner, “Intermediate states in andreev bound state fusion,” (2021).
- [148] S. De Franceschi, J. A. van Dam, E. P. A. M. Bakkers, L. F. Feiner, L. Gurevich, and L. P. Kouwenhoven, *Applied Physics Letters* **83**, 344 (2003), <https://doi.org/10.1063/1.1590426> .
- [149] T. S. Jespersen, M. Aagesen, C. Sørensen, P. E. Lindelof, and J. Nygård, *Phys. Rev. B* **74**, 233304 (2006).
- [150] S. Csonka, L. Hofstetter, F. Freitag, S. Oberholzer, C. Schönenberger, T. S. Jespersen, M. Aagesen, and J. Nygård, *Nano Letters* **8**, 3932 (2008).
- [151] E. J. H. Lee, X. Jiang, M. Houzet, R. Aguado, C. M. Lieber, and S. De Franceschi, *Nature Nanotechnology* **9**, 79 (2014).
- [152] J. Gramich, A. Baumgartner, and C. Schönenberger, *Phys. Rev. B* **96**, 195418 (2017).
- [153] S. De Franceschi, S. Sasaki, J. M. Elzerman, W. G. van der Wiel, S. Tarucha, and L. P. Kouwenhoven, *Phys. Rev. Lett.* **86**, 878 (2001).
- [154] V. Fatemi, P. D. Kurilovich, M. Hays, D. Bouman, T. Connolly, S. Diamond, N. E. Frattini, V. D. Kurilovich, P. Krogstrup, J. Nygård, A. Geresdi, L. I. Glazman, and M. H. Devoret, *Phys. Rev. Lett.* **129**, 227701 (2022).

A Cavity readout

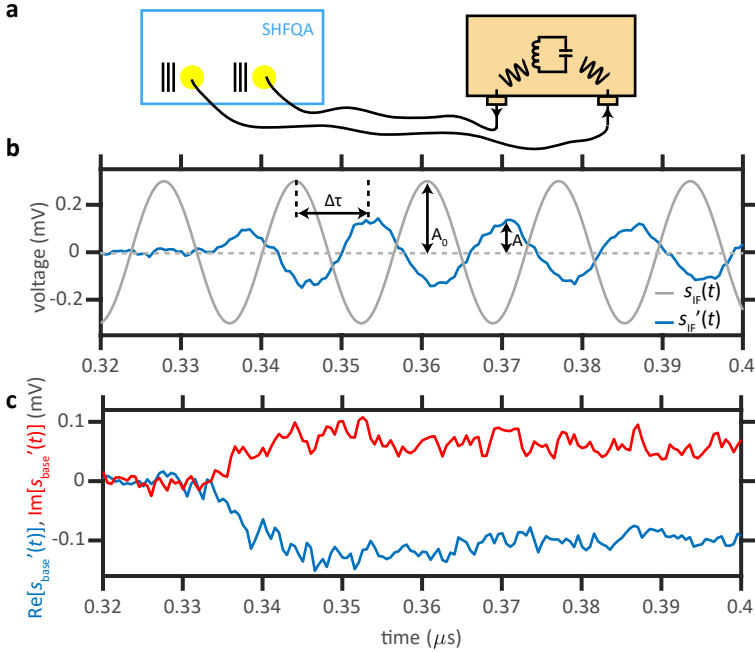


Figure E1. Cavity readout in time domain.

For time domain measurement, qubit drive pulse and cavity readout pulse have to be aligned. Reflected (or transmitted, depending whether the measurement is in reflection or transmission) waves have to be recorded with a sampling rate of a few GSa per second. In our lab, we use the SHFQA from Zurich instrument to readout cavity photons. It has a local oscillator frequency synthesis from 0.5 to 8.5 GHz and a bandwidth for intermediate frequencies of 1 GHz. Since the modulation does not use mixers, the instrument can be used

without mixer calibration.

In practise, we choose a local oscillator frequency f_{LO} and design a cavity readout pulse with an intermediate frequency f_{IF} and pulse shape $A(t)$ ¹:

$$s_{\text{IF}}(t) = A(t)e^{i2\pi f_{\text{IF}}t}. \quad (\text{A.1})$$

The frequencies are chosen such that the resonator can be excited, $f_{\text{res}} \approx f_{\text{LO}} + f_{\text{IF}}$. To demonstrate the readout pulse, its in-phase component is plotted in Figure A.1.b in grey. Then, the readout pulse is mixed with the local oscillator to $e^{i2\pi f_{\text{LO}}t} \cdot A(t)e^{i2\pi f_{\text{IF}}t}$. We set the phase offset of the readout pulse to be zero for convenience. The wave travels towards the sample in the cryostat. After exciting the resonator, the wave coming back from the cryostat now carries information about the resonator. The first demodulation step of the instrument is done internally at f_{LO} . After that, the wave $s'_{\text{IF}}(t)$ can be acquired and stored in time steps with a step size of 0.5 ns. An example measurement is shown in blue in Figure A.1.b. Again, this is the in-phase component of the measurement. One observes that its oscillation starts at a later point at around $0.33 \mu\text{s}$ which is due to the travelling time of the wave. The reflected wave $s'_{\text{IF}}(t)$ is further demodulated to the baseband:

$$s_{\text{base}}(t) = s'_{\text{IF}}(t) \cdot e^{-i2\pi f_{\text{IF}}t}. \quad (\text{A.2})$$

Figure A.1.c shows the in-phase and quadrature components of $s_{\text{base}}(t)$. Different qubit occupation shifts the resonator frequency. When measuring a microwave pulse with a fixed frequency close to the resonator frequency, different qubit occupation reflects itself as different traces of in-phase and quadrature components of the microwave pulse.

¹We usually use a Gaussian flat top pulse with a rise time of 10 ns.

B Derivation of the capacitively coupled quarter-wavelength transmission line resonator

We assume that the voltage and current of a resonance is a superposition of a forward- and backward-propagating wave with the wavevector β_1 :

$$\begin{aligned} V_1 &= V_1^+ e^{-i\beta_1 x} + V_1^- e^{i\beta_1 x}, & V_2 &= V_2^+ e^{-i\beta_1(x-L/2)} + V_2^- e^{i\beta_1(x-L/2)} \\ I_1 &= \frac{V_1^+}{Z_0} e^{-i\beta_1 x} - \frac{V_1^-}{Z_0} e^{i\beta_1 x}, & I_2 &= \frac{V_2^+}{Z_0} e^{-i\beta_1(x-L/2)} - \frac{V_2^-}{Z_0} e^{i\beta_1(x-L/2)}, \end{aligned} \quad (\text{B.1})$$

where V_1 and I_1 are voltage and current profile on the left transmission line and V_2 and I_2 that on the right transmission line. The first mode with a wavelength of $2L$ is a resonance which also exists when there is no coupling capacitance, i.e., $\beta_1 = 2\pi/\lambda = \pi/L$. According to the design, it possesses a voltage node at $x = 0$ and $x = L$ such that

$$\begin{aligned} V_1(0) \stackrel{!}{=} 0 &\Rightarrow V_1^+ = -V_1^- \\ V_2(L) \stackrel{!}{=} 0 &\Rightarrow V_2^+ = V_2^-. \end{aligned} \quad (\text{B.2})$$

A second condition arises as the voltage at $x = L/2$ is continuous:

$$V_1\left(\frac{L}{2}\right) \stackrel{!}{=} V_2\left(\frac{L}{2}\right) \Rightarrow V_1^+ = iV_2^+. \quad (\text{B.3})$$

Now, we have all the information for the first resonating mode. For deriving the second mode, the first condition Eq. (C.2) still holds but give different results:

$$\begin{aligned} V_1(0) \stackrel{!}{=} 0 &\Rightarrow V_1^+ = -V_1^- \\ V_2(L) \stackrel{!}{=} 0 &\Rightarrow V_2^+ = -V_2^- e^{i\beta_2 L}, \end{aligned} \quad (\text{B.4})$$

where β_2 is the wavevector of the second mode. Moreover, the current at the capacitance has to be continuous which leads to a further condition:

$$I_1\left(\frac{L}{2}\right) \stackrel{!}{=} I_2\left(\frac{L}{2}\right) \Rightarrow V_1^+ = V_2^+ \frac{1 + e^{i\beta_2 L}}{e^{-i\beta_2 L/2} + e^{i\beta_2 L/2}} \quad (\text{B.5})$$

By introducing the coupling capacitance, an alternating current can exist at the capacitance. Its amplitude is related to the voltage across via the impedance $1/i\omega_2 C$.

$$V_1\left(\frac{L}{2}\right) - V_2\left(\frac{L}{2}\right) \stackrel{!}{=} \frac{1}{i\omega_2 C} I_1\left(\frac{L}{2}\right). \quad (\text{B.6})$$

Inserting eq. (1.11) and (1.12) into (1.13) gives a condition which determines the resonance frequency ω_2 :

$$\Rightarrow \omega_2 = \frac{1}{2CZ_0} \tan^{-1}\left(\frac{\beta_2 L}{2}\right). \quad (\text{B.7})$$

Since β_2 is a deviation from β_1 , we can Taylor expand the tangent at $\frac{\beta_2 L}{2} = \pi/2$: $\tan^{-1}\left(\frac{\beta_2 L}{2}\right) \approx -\left(\frac{\beta_2 L}{2} - \frac{\pi}{2}\right)$. Inserting the Taylor expansion into eq. (1.14) leads to

$$\omega_2 = -\frac{1}{2CZ_0} \left(\frac{\beta_2 L}{2} - \frac{\pi}{2}\right). \quad (\text{B.8})$$

Then the relation for constant speed of light in the transmission line is used, $\beta_2 = (\beta_1/\omega_1)\omega_2 = (\pi/L\omega_1)\omega_2$. That yields

$$\frac{\omega_1 \omega_2}{\omega_2 - \omega_1} = -\frac{\pi}{4CZ_0} \quad (\text{B.9})$$

Finally, an expression for the frequency difference is obtained when identifying $\omega_2 \omega_1 \approx \omega_1^2$:

$$\Delta\omega = \omega_2 - \omega_1 = -\frac{4CZ_0}{\pi} \omega_1^2. \quad (\text{B.10})$$

The wave-vector β_2 can be computed as

$$\beta_2 = \frac{\pi}{L} \left(1 - \frac{4CZ_0}{\pi L} \omega_1\right). \quad (\text{B.11})$$

One can see that $1 - 4CZ_0\omega_1/\pi L$ is the correction factor to obtain β_2 from β_1 . Furthermore, this formula is valid when the characteristic impedance of the transmission line is much smaller than the impedance of the coupling capacitance, $C\omega_1 Z_0 \ll 1$.

C Additional DC transport measurement of full-shell epitaxial InAs/Al nanowire Josephson junctions

Now, we will investigate the transport behaviour of our nanowire (NW) at low gate voltages. The differential conductance G was measured as function of voltage bias V at low V_G , close to the depletion of the semiconductor. Fig. E1 shows the differential conductance as a function of V_G and voltage bias V at negative V_G . At low gate voltage, one can recognize an opening of a gap with multiple resonances in the gap (Fig. E1a). Some of the resonances are gate independent at a value of $|eV| = 2\Delta'$, while some clearly show gate dependence. As the gate voltage increases, more "in-gap" resonances appear, giving rise to very complicated resonance spectra (Fig. E1c). These "in-gap" resonances appear to be pushed to low bias when resonance features occur outside the gap.

In previous experiments [147], similar characteristics were found for well-defined in-situ grown tunnel barriers dividing the NW up into three segments. Here, we can imagine a similar scenario with unintentional quantum dots (QDs) forming at potential minima, when the NW is near pinch-off. Unlike the crystal-phase defined QDs in nanowires, the barriers of these unintentional QDs are not controlled in our experiment. They could arise from potential fluctuation in the semiconductor or mismatch in the Fermi velocity at the superconductor-semiconductor interfaces [148–150]. Andreev bound states (ABSs) can form in the semiconducting lead segments that are coupled to the superconducting contact (S-contact) [147, 151, 152].

Fig. E1b shows an energy level diagram of the nanowire device close to the depletion. The resonances outside the gap can be understood as Coulomb blockade (CB) resonances, where a QD state is aligned to a superconducting coherence peak in the superconducting electrodes S_1 or S_2 , shifted in bias voltage $e\Delta V = \pm 2\Delta'$ by the superconducting gap. The additional resonances in the bias window $e|\Delta V| < 2\Delta'$ suggest the presence of ABSs in the lead segments.

In the following, we will focus on the description of the 'in-gap' resonances, denoted with Roman numerals i-iv and i'-iv', in the Coulomb blockade at around $V_G = -2V$. In this regime, transport of electrons through the QD

involves simultaneous tunneling of two or more electrons, a process known as cotunneling [153]. We find a pair of strong resonances $i(i')$ at constant $eV = \pm 2\Delta'$ and a pair of weak resonances $iii(iii')$ at constant $eV = \pm\Delta'$, consistent with an increased quasiparticle density of states (DoS) at an energy $\Delta' = 190 \mu\text{eV}$ in the LS_1 , mapped by an increased single particle DoS in the LS_2 at $eV = \pm\Delta'$ or by the superconducting coherence peak in S_2 . Because the resonances $i(i')$ are at constant $eV = \pm 2\Delta'$, we attribute them to a short-junction ABS residing in LS_1 , with the resonance energy pinned at the gap values. The replicas $iii(iii')$ can be understood as quasiparticle tunneling from the short-junction ABS in LS_1 to residual quasiparticle DoS in LS_2 .

At multiple CB resonances, for example $V_G = -2.022 \text{ V}$, we find that the horizontal resonances i and i' are bent to lower bias voltage values and continue as resonances with positive and negative slopes, as pointed out by green arrows. We attribute the resonances with positive and negative slopes to QD resonances, where the QD level is aligned to one of the ABSs. The avoided crossing between the horizontal resonances and QD resonances can be understood as hybridization between the ABSs on the LSs with an QD level, which occurs at enhanced tunnel coupling between the LSs and the QD [148]. In particular, the avoided crossing with a QD resonance of negative slope (positive slope) indicates hybridization of an ABS on the LS_1 (LS_2) with the QD level, mapped by a short-junction ABS in LS_2 (LS_1) or by the superconducting coherence peak in S_2 (S_1). We note that the observation of symmetric avoided-crossings with QD resonances of both slopes suggests the presence of short-junction ABSs on both LSs.

At lower bias voltage $e|V| < 2\Delta'$, we find again a pair of strong resonances $ii(ii')$ and a pair of corresponding replicas $iv(iv')$. Following a similar argument as above, we attribute the resonances $ii(ii')$ to a second ABS in LS_1 , that is not pinned to Δ' and is accompanied with finite quasiparticle dwell time in the non-superconducting part in the long-junction limit [154].

To conclude, we have performed tunneling spectroscopy measurement in a epitaxial InAs/Al NWJJ using an unintentionally formed QD in the semiconductor. We have observed resonances that are consistent with ABSs residing in the semiconducting lead segments between the epitaxially grown S-contacts and the QD. In the investigated gate range, the coupling strength between the ABSs and the QD is sufficiently strong to form an hybridized system.

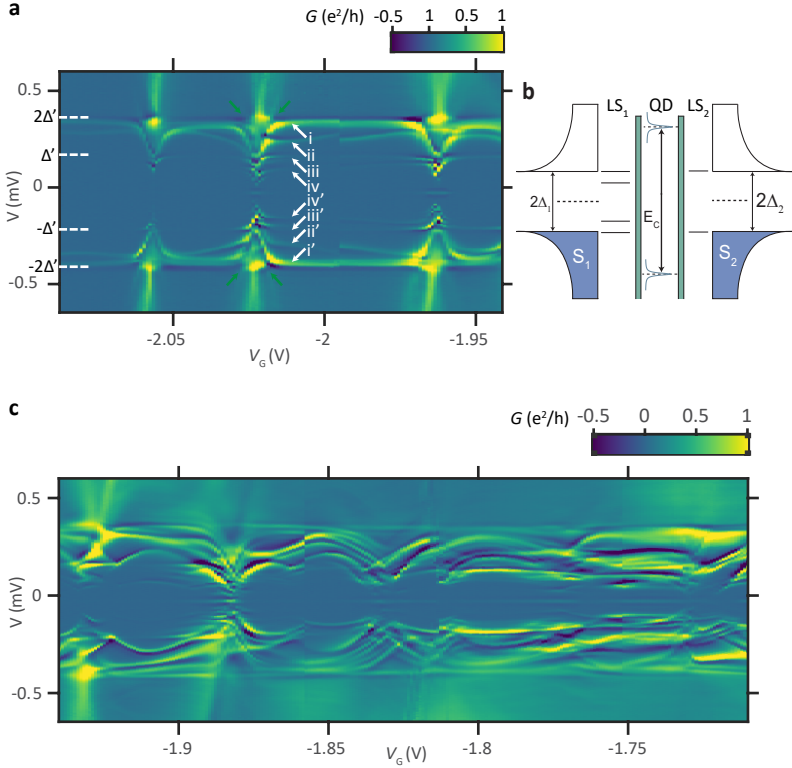


Figure E1. Voltage bias measurement near depletion. **a,c**, Differential conductance G as a function of bias voltage V and gate V_G . **b**, An energy level diagram with the S-contacts (S_1 , S_2), proximitized lead segments (LS_1 , LS_2) and QD levels. Finite residual DoS is omitted in this figure. Figure adapted from [75].

D Additional microwave spectroscopy measurement of full-shell epitaxial InAs/Al nanowire Josephson junctions

This appendix presents a systematic study of single quasiparticle transitions (SQPTs) as a function of the gate voltage V_R and superconducting phase difference ϕ_R , measured in the right InAs/Al nanowire Josephson junction (NWJJ). The SQPTs are revealed using pulsed two-tone spectroscopy techniques.

Fig. E1a shows a two-tone spectrum as a function of V_R at $\phi_R = 0$. We find five gate dependent resonances, two are weak and the other three are strong. In the following, we will focus on the three strong resonances, denoted with the Roman numerals i)-iii) and measure the superconducting phase dependent two-tone spectra at four selected gate voltage values, indicated with alphabets b-e.

At $V_R = -0.189$ V, we find the two weak resonances decreasing in frequency towards $\phi_R = \pm\pi$. Thus, we attribute them to pair or mixed pair transitions. At slightly higher gate voltage value (Fig. E1c), we find that the resonances i)-iii) all split into four resonances for $\phi_R \neq 0$ or $\phi_R \neq \pm\pi$, indicating that each of them is indeed associated with SQPTs between two Andreev manifolds. The observation of three groups of SQPTs can be understood as the presence of four Andreev manifolds, caused by a small transverse subband spacing or increased electrochemical potential in the semiconducting nanowire, with the resonance group i) corresponding to the transitions between the first and second manifold, the resonance group ii) to that between the first and third manifold, and the resonance group iii) to that between the first and fourth manifold. We find that all the SQPTs possess a higher transition frequency at $\phi_R = \pm\pi$ than at $\phi_R = 0$. Additional resonances featuring minima at $\phi_R = \pm\pi$ arise from pair transitions and indicate the large number of channels in the junction.

At $V_R = -0.175$ V, we find that the dispersion of the SQPTs is reversed (Fig. E1d). Now, the transition frequencies at $\phi_R = 0$ become higher than that at $\phi_R = \pm\pi$. Overall, the transition frequencies of the group i) and iii) are pushed to higher values, while that of the group ii) remain nearly constant. Finally, at $V_R = -0.175$ V, the resonance group iii) is pushed above 18 GHz for an extended range in ϕ_R (Fig. E1e). All SQPT groups appear to remain at higher frequencies at $\phi_R = 0$ than at $\phi_R = \pm\pi$. Looking at the SQPT

group ii), we observe two interesting features (Fig. E1f). First, the frequency splitting of the SQPTs is rather small, not exceeding a few hundreds of MHz. Second, the SQPT remain flat over an extended range of ϕ_R around $\phi_R = 0$, before abruptly drop to lower values, when approaching $\phi_R = \pm\pi$. The first observation indicates a small difference in the spin-dependent Fermi velocity of the quasiparticles. This can arise by tuning the electrochemical potential away from the point where two subbands of opposite spins hybridize, or by a gate tunable spin-orbit coupling strength. The reason for the second observation is unclear yet.

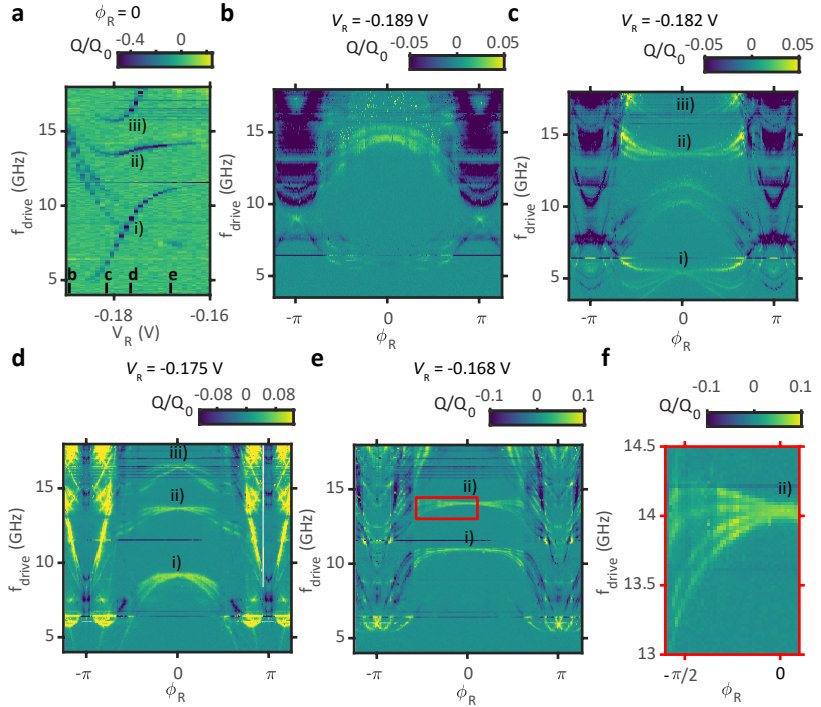


Figure E1. Local gate dependence of SPQTs. **a**, Two-tone spectrum as a function of drive frequency f_{drive} and gate voltage V_R at $\phi_R = 0$. **b-e**, Sequential two-tone spectra as a function of f_{drive} and ϕ_R at the gate voltage values marked in **a**. **f**, A zoom-in to the box in **e** to emphasise the small transition frequency splitting between the SQPTs and their abrupt drop when approaching $\phi_R = -\pi$.

Publications

- “Coherent control of a few-channel hole type gatemon qubit”
H. Zheng, **L. Y. Cheung**, N. Sangwan, A. Kononov, R. Haller, J. Ridderbos, C. Ciaccia, J. H. Ungerer, A. Li, E.P.A.M. Bakkers, A. Baumgartner and C. Schönenberger
Nano. Lett. **24**, 7173-7179 (2024)
- “Photon-mediated long-range coupling of two Andreev pair qubits”
L. Y. Cheung, R. Haller, A. Kononov, C. Ciaccia, J. H. Ungerer, T. Kanne, J. Nygård, P. Winkel, T. Reisinger, I. M. Pop, A. Baumgartner and C. Schönenberger
Nat. Phys., accepted (2024)
- “Performance of high impedance resonators in dirty dielectric environments”
J. H. Ungerer, D. Sarmah, A. Kononov, J. Ridderbos, R. Haller, **L. Y. Cheung** and Christian Schönenberger
EPJ Quantum Technology **10**, 41 (2023)
- “Phase-dependent microwave response of a graphene Josephson junction”
R. Haller, G. Fülöp, D. Indolese, J. Ridderbos, R. Kraft, **L. Y. Cheung**, J. H. Ungerer, K. Watanabe, T. Taniguchi, D. Beckmann, R. Danneau, P. Virtanen, and C. Schönenberger
Phys. Rev. Research **4**, 13198 (2022)

Talks

- *Long distance coupling of Andreev qubits*
Swiss Quantum Days, Villars-sur-Ollon (Switzerland), February 2023
- *Superconducting resonator for microwave measurement of Andreev spin qubits*
QSIT Junior Meeting, Flumserberg (Switzerland), June 2019

Poster Contributions

- “*Transport spectroscopy in semiconducting nanowire electronic devices*”
NCCR QSIT, Arosa (Switzerland), February 2020

Acknowledgements

I am deeply grateful to the people who have made this PhD thesis possible, and I would like to take this opportunity to thank them for their support and encouragement.

To start with, I would like to direct my greatest gratitude to my thesis advisor Prof. Dr. Christian Schöenberger for giving me the opportunity to conduct my doctoral research in his group. I had quite a unique opportunity to work in both DC and microwave measurements of quantum devices. In both fields, I have benefited a lot from his extensive knowledge about nanoelectronic devices, that guided me throughout the whole doctoral study. Christian was (almost) always supportive, which leads to fancy RF instruments and, particularly, an opportunity for me to visit the Quantronics group, an activity that immensely boosted my research. Physics was never the only thing I could learn from Christian, it was also his enchanting way to interact with people, and his unceasing passion to discover and understand new topics. Perhaps, there are two characters from Christian which have left deepest impressions in me: First, his management and negotiation skills to support a group of 20+ researchers with resources and time. Second, his ability to keep the work-life balance, being a professor while having a sporty life-style. I think these have widened my horizon quite a lot. For all these, I want to thank you, Christian.

Second, I would like to thank Dr. Marcelo Goffman and Prof. Dr. Attila Geresdi for making the effort to read my thesis. It is my honor to have two such excellent physicists in my PhD committee.

This PhD work would have *literally* been not possible without the help from a lot of great scientists. Here, I would like to thank the people I met at the Université Paris-Saclay: Dr. Marcelo Goffman, Prof. Dr. Hugues Pothier, Cyril Metzger, Manas Ranjan Sahu. I would like to explicitly thank Dr. Marcelo Goffman for his openness in sharing the knowledge about microwave engineering. Setting up the time domain measurement would have taken a while longer without the scientific exchange with him. I was lucky to work on the launch of a JPA from the group of Dr. Ioan Pop, Karlsruhe institute of technology, which sped up the measurement by a factor of five. For that, I am grateful to him and his group members. My gratitude also goes to the nanowire providers, Prof. Dr. Peter Krogstrup, Prof. Dr. Jesper Nygård and their group members at the University of Copenhagen.

I specially thank both Dr. Roy Haller and Dr. Artem Kononov for tirelessly accompanying me through the whole writing phase of this thesis. I would also like to thank Dr. Andreas Baumgartner, Dr. Prasanta Kumbhakar, Dr. Jann Hinnerk Ungerer, Dr. Alessia Pally, Han Zheng, Nikunj Sangwan and Giorgio Fabris for proofreading parts of the thesis.

I am immensely grateful to the colleagues whom I collaborated very closely: Dr. Roy Haller, with whom we advanced the microwave setup a lot. His thorough, perhaps perfectionist work ethics make him a person you can rely on. Dr. Artem Kononov, for his always critical scientific inputs that solidifies the scientific foundations. Dr. Alessia Pally, with whom I evaporated Pb runs by runs. In the dark era of the world pandemic, we stood in front of the Balzers and filled liquid N_2 . Dr. Jann Hinnerk Ungerer, for his knowledge about cQED. Han Zheng, Nikunj Sangwan and Tom Jenniskens, for the work with Ge/Si gatemons. Alexei Orekhov, for the Al shell etching recipe. Carlo Ciaccia, for the JPA and 2DEG devices. Dr. Christian Jünger, from whom I learnt (almost) all the nanofabrication techniques and the operation of a dilution refrigerator. I would also like to acknowledge the supports from my other post-docs: Malin Nilsson and Joost Ridderbos. I am grateful to Francisco Jesus Matute Fernandez-cañadas from the group of Prof. Dr. Alfredo Levy Yeyati, Universidad Autónoma de Madrid, for the numerous insightful discussions about Andreev spectra.

I feel deeply thankful for having the opportunity to work in the Nanoelectronics group with such enthusiasts from all over the world, not only about science but also about life: Dr. Martin Endres, Dr. Paritosh Karnatak, Ian Correa Sampaio, Rounak Jha, Zarina Mingazheva, Deepankar Sarmah, Blesson-sam Varghese, Dr. Arunav Bordoloi, Dr. Olivier Faist, Dr. David Indolese, Dr. Mehdi Ramenzani, Dr. Frederick Thomas, Dr. Lujun Wang, Dr. Libin Wang, Matthijs Hermans, and all the former colleagues. All the group activities with the big group, from skiing in the Alps to swimming in the Rhine, from biking in Tuscany to via Ferrata in Graubünden, and much more to mention and to come, helped to remind me that there is more in life than difficult moments in the research. Not to forget the activities in smaller groups, the barbeque at the Rhine, movie nights, or just one or two beers on the rooftop, all these have made the PhD study a vibrant period of time for me, filled with memories.

Special thanks also go to many people at the Physics Department. I want to thank Barbara Kammermann and Astrid Kalt for the administrative works and motivating chats in the corridors. My thanks are also directed to the electronics workshop and the mechanical workshop: Sascha Martin and his team, thank you for the copper plates for the sample holder and the Al shields. Andreas Tonin, Roberto Maffiolini, thank you for the discussion about the PCB. Sascha Linder, thank you for making the PCB. I would also like to thank Dominik Sifrig for the supply of helium, Daniel Sacker and Laurent Marot for the help with the cleanroom.

Finally, I would like to thank my family and friends, especially the ones who are not in Switzerland such that we could not meet more often, for supporting me throughout the years and creating all the lovely moments. If any of you was not there, I would not be where I am today.